EXPERIMENTAL EVALUATION OF SAND, RESIN-COATED SAND, AND CERAMIC PROPPANTS FOR THE HYDRAULIC FRACTURING OF EAGLE FORD SHALE RESERVOIRS

A Dissertation

by

AHMED MOHAMED MAHMOUD ELSARAWY

Submitted to the Office of Graduate and Professional Studies of
Texas A&M University
in partial fulfillment of the requirements for the degree of

DOCTOR OF PHILOSOPHY

Chair of Committee,	Hisham A. Nasr-El-Din
Committee Members,	Stephen Holditch
	Jerome Schubert
	Mahmoud El-Halwagi
Head of Department,	Jeff Spath

May 2019

Major Subject: Petroleum Engineering

ABSTRACT

The coupling of the technologies of the horizontal drilling and hydraulic fracturing operations has enabled the economic development of the shale oil and gas reservoirs and led to the recent significant increase in the U.S. hydrocarbon production and reserve. The literature review revealed the importance of the fracture conductivity which is usually sacrificed in the hydraulic fracturing operation. The objective of this study is to experimentally evaluate the damaging mechanisms to fracture conductivity associated with the use of ceramic, sand, and resin-coated sand proppants in the hydraulic fracturing of Eagle Ford shale formations.

The combined effect of proppant crushing, compaction, and embedment mechanisms is assessed by the measurements of the fracture width and proppant porosity at stress conditions using a new procedure that allows the direct measurement of the propped fracture width at simulated downhole conditions. Furthermore, the proppant diagenesis mechanism is assessed by studying the chemical interactions between the proppant, the fluid, and the formation, using, high-pressure/high-temperature (HP/HT) aging cells, and, the post-aging analyses of the solids and fluids using scanning electron microscopy (SEM) with an energy dispersive X-ray spectroscopy (EDS) and Inductively Coupled Plasma Optical Emission Spectroscopy (ICP-OES).

The study presents tables of the values of the fracture width and the proppant porosity for different proppant types and concentrations. The 20/40-mesh resin-coated sand at concentration 0.2 lb/ft^2 showed the highest reduction in fracture width and

proppant porosity of 25.88 and 44.16%, respectively, while the 40/70-mesh ceramic proppant at 0.6 lb/ft^2 showed the minimum reduction of 5.68 and 7.88%, respectively, at 8000 psia closure stress. Furthermore, the diagenesis process was found more profoundly in the case of ceramic proppant; and the chemical interactions between the proppant, the formation, and the fluid led to the precipitation of $CaSO_4$ and the overgrowth of different zeolite minerals on the proppant surface.

The study contributes to the understanding of the proppant-related fracture conductivity damaging mechanisms. The results can be used in the hydraulic fracturing design, the production forecasting models, and the proppant selection process for an improved fracture conductivity, and hence, an improved hydrocarbon production from the Eagle Ford shale formations.

DEDICATION

I dedicate this dissertation to my blessed family, including my parents, grandparents, brother, sisters, uncles, and aunts without their love, support, and encouragement, the completion of this work would have not been possible.

ACKNOWLEDGEMENTS

I would like to thank my committee chair, Dr. Hisham Nasr-El-Din, for his continuous guidance, help, and support throughout the course of this research. I would also like to thank my committee members, Dr. Holditch, Dr. Schubert, and Dr. El-Halwagi, for their guidance and support throughout the course of my research.

Thanks also go to my friends and colleagues and the department faculty and staff for making my time at Texas A&M University a great experience.

Finally, special thanks go to my family for their motivation and love.

CONTRIBUTORS AND FUNDING SOURCES

Contributors

This work was supervised by a dissertation committee consisting of Professor Hisham A. Nasr-El-Din [advisor] and Stephen A. Holditch and Jerome J. Schubert of the Department of [Home Department] and Professor Mahmoud M. El-Halwagi of the Department of [Outside Department].

The analysis of the results of the Scanning Electron Microscope and the Energy Dispersive Spectroscopy was done with the help of Dr. Michael Pendleton and Dr. Stanislav Vitha from the microscopy imaging center at Texas A&M University.

Funding Sources

The graduate study was supported by a research assistantship from Texas A&M University. Also, this work was made possible in part by the Crisman Institute for Petroleum Research at the Harold Vance Department of Petroleum Engineering at Texas A&M University.

NOMENCLATURE

U.S. EIA	United States Energy Information Administration
md	Millidarcy
ft	feet
MMscf	Million standard cubic feet
bopd	Barrel oil per day
3D	Three dimensional
NPV	Net present value
Bscf	Billion standard cubic feet
ANN	Artificial neural network
bbls	Barrels
LWC	Light weight ceramic
USD	Unites states dollars
Mcf	Thousand cubic feet
Bcf	Billion cubic feet
Tcf	Trillion cubic feet
BOE	Barrel oil equivalent
STB	Stock tank barrel
RCS	Resin-coated sand
API	American Petroleum Institute
RP	Recommended practice

ISO	International Organization for Standardization
lb	Pound force
cp	Centipoise
SEM	Scanning electron microscope
Si/Al	Silicon to aluminum ratio
EDS	Energy Dispersive X-ray Spectroscopy
Psia	Absolute pressure in pound per square inch
LVDT	Linear Variable Displacement Transducer
XRD	X-ray diffraction
wt%	weight percent
g/cc	grams per cubic centimeter
mm	millimeter
XRF	X-ray fluorescence
in.	Inch
ϕ_{pi}	Initial proppant porosity in the experimental fracture model
W_{fi}	Initial fracture width in the experimental fracture model
ϕ_p	Proppant porosity
V_P	Proppant pore volume
V_b	Proppant bulk volume
V_P	Solid volume of the proppant
V_s	Solid volume of the proppant
M_P	Proppant mass

ρ_p	Proppant density
V_f	Bulk volume of the propped fracture
W_f	Measured fracture width
A_f	Surface area of the propped fracture
HP/HT	High-pressure/high-temperature
gm	gram
ICP-OES	Inductively Coupled Plasma Optical Emission Spectroscopy
UFD	Unified fracture design
kx	thousand times
ppm	Part per million

TABLE OF CONTENTS

Page

LIST OF FIGURES

Page

LIST OF TABLES

Page

1. INTRODUCTION AND LITERATURE REVIEW*

The oil and gas production from shale formations has significantly contributed to the U.S. economy since the production boom started in 2008. As shown in the resource pyramid presented by Holditch (2006), unconventional resources, including shale oil and gas reservoirs, are found in large volumes and require improved technologies to be developed. **Figure 1.1** shows the most recent U.S. total natural gas proved reserves and the share of natural gas from shale gas reservoirs. As of 2016, the proved reserves of U.S. natural gas from shale is 209.8 Tcf, which is equivalent to 62% of the total U.S. natural gas reserves (U.S. Energy Information Administration, EIA, 2018).

* Reprinted with permission from "Propped Fracture Conductivity in Shale Reservoirs: A Review of Its Importance and Roles in Fracturing Fluid Engineering" by A. Elsarawy and H. Nasr-El-Din, 2018. SPE-192451-MS, Copyright 2018 by Society of Petroleum Engineers. And permission from "An Experimental Investigation of Proppant Diagenesis and Proppant-Formation-Fluid Interactions in Hydraulic Fracturing of Eagle Ford Shale" by A. Elsarawy and H. Nasr-El-Din, 2018. SPE-191225-MS, Copyright 2018 by Society of Petroleum Engineers. And permission from "Experimental Evaluation of Sand Porosity in Eagle Ford Shale Fractures" by A. Elsarawy and H. Nasr-El-Din, 2018. SPE-191240-MS, Copyright 2018 by Society of Petroleum Engineers.

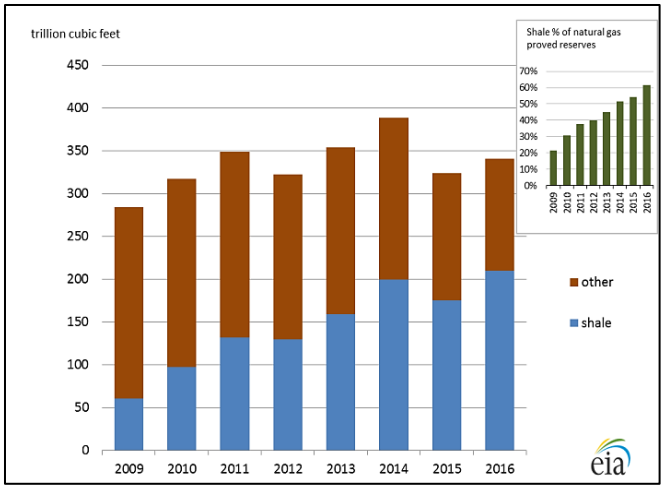

Figure 1.1 U.S. total natural gas proved reserves including shale and other sources (U.S. EIA 2018).

There are more than 20 significant shale gas plays in the U.S. which are widely distributed; the most active plays are the Barnett, Woodford, Haynesville, Marcellus, and Fayetteville shales. Other active shale oil plays are the Bakken, Niobrara, Utica, and most recently, the Eagle Ford shales. These shale reservoirs have an ultra-low permeability value (less than 0.01 md). The hydraulic fracturing and horizontal drilling technologies are the major technologies that enable the economic development of such tight reservoirs. The hydraulic fracturing improves the well productivity by inducing fractures inside the formation to increase the formation permeability through injecting a fluid with a pressure higher than the formation fracture pressure. The injection of proppant, a fracture propping agent, is necessary to prevent the fracture closure after the removal of the surface pressure. The proppant is transported into the fractures by the aid of a viscosifying-agent and a friction reducing-agent to reduce the required pump surface pressure.

1.1. Importance of Propped Fracture Conductivity in Shale Hydraulic Fracturing

The productivity improvement from hydraulic fracturing of vertical wells depends on the relative fracture conductivity, the ratio of the fracture conductivity to the formation conductivity (McGuire and Sikora 1960). As the conductivity ratio increases, the well productivity increases up to a certain value, after which, any further increase does not contribute to a significant increase in production. Unconventional reservoirs, by definition, have 0.01 md permeability or less (Holditch 2006), while the fracture permeability could reach 1000s md, as it is packed with a well-sorted and large-grain proppant. In hydraulic fracturing of shale reservoirs, it would be suggested that the fracture conductivity is always infinite compared to the ultra-low permeability of the matrix, and that any damage or improvement in the fracture conductivity will have no impact on the well production performance. In other words, the proppant conductivity could be sacrificed in the completion optimization process of shale reservoirs. However, the following reviewed studies show that the fracture conductivity does matter, and, in some cases, it can significantly affect the well production performance in shale reservoirs, in both the short and long terms. Although Vincent (2009) presented more than 200 field studies in which the production was successfully improved by modifying the fracture operation design, including several cases from tight-gas reservoirs and coal-bed methane with ultra-low permeability, this following section focuses on studies done specifically on shale formations.

For example, Mayerhofer et al. (2006) presented a numerical production simulator which discretely models the fracture network structure in the Barnett shale.

The model was integrated with the results from microseismic fracture mapping, and a parametric study was presented to show how the fracture conductivity affects the well productivity. The simulation results showed a significant pressure drop in the fracture network in the case of using fracture conductivity of 0.5 md-ft, in contrast to the use of 5 or 20 md-ft conductivity. The subsequent effect on production showed that higher fracture conductivity would result in higher production. After 1800 days, the increase in the fracture conductivity from 0.5 md-ft to 20 md-ft increased the cumulative gas production from 700 to 3400 MMscf. The effect of near-well fracture conductivity (300 ft from the well) was studied separately. The cumulative gas production increased from 1550 to 1700 MMscf when near-well fracture conductivity increased from 5 to 20 md-ft. Rankin et al. (2010) were able to increase the well production of new wells in the Bakken and Three Forks shale oil plays by optimizing the well completion operation. The authors were able to develop a successful completion strategy through the careful investigation of the data and the key learnings from offset wells. The length of the horizontal lateral and number of fracturing stages, along with the proppant type and concentration were the key variables that improved the well production performance with an economic profitability. In the middle Bakken, the use of ceramic proppant and increasing the number of stages provided a higher initial production rate and higher production sustainability in the first 30 days. After producing 50,000 barrels of cumulative oil production, the wells completed with the ceramic proppants were producing at 580 to 940 bopd, while the wells completed with the sand proppants were producing at 105 to 250 bopd. While in the Three Forks shale, the wells treated with 18

plug and perf stages and ceramic proppant showed a 37% higher initial production rate compared to adjacent wells treated with 24 frac sleeve stages with sand proppant. In addition, the increase in production rate after 30 days of production and after reaching cumulative production of 48,000 barrels were 56% and 70%, respectively.

Mendoza et al. (2011) presented a case study to show the design of an optimum completion strategy of a horizontal well in the Eagle Ford reservoir. Post-fracture data from two nearby wells was used to calibrate 3D fracture growth and conductivity models to optimize the number of fracturing stages, and the number of clusters per fracture to maximize the Net Present Value (NPV). Sensitivity analysis on the fracture conductivity was run to study its effect on well productivity and NPV. The production forecast showed that increasing the fracture conductivity 0.5 md-ft to 300 md-ft could increase the gas reserve from 5.6 Bscf to 9 Bscf (60% increase in gas reserve).

Vincent (2011) analyzed the field results in the Niobrara, Bakken, Viking, Haynesville, Eagle Ford and other shale reservoirs completed with transverse fractures to develop the best practices for shale completion techniques and investigated the effect of fracture conductivity on the oil and gas well production rates. In Eagle Ford, analysis of the production data over 12 months of 750 horizontal well showed that the cumulative production of the wells completed using high-quality ceramic proppant was 33% more than the wells completed with lower-quality proppants (sand or resin-coated sand). The analysis of the results suggested that the wells completed with high conductivity fractures, which was achieved by higher-quality proppant, provided a superior production performance through the available production period of liquid rich shale

formations. The author finally concluded that the conductivity loss over the time was significant and should be included in the different fracture simulation studies, and also proposed a re-fracturing treatment as a remedial response to the cases with severe conductivity loss. The re-fracturing technique was explained in detail in another paper for the same author (Vincent 2010).

Penny et al. (2012) showed the dependency of the horizontal well productivity and its economics on the efficient communication between the wellbore and transverse fractures. The communication is strongly controlled by the fracture conductivity, which highlights the importance of fracture conductivity over the life cycle of the well. By the use of the laboratory experiments and field validation studies, the authors investigated the effect of changing fracture conductivity on the final well productivity, as well as the changes that could happen over the different time scales. The authors related the fracture conductivity to the gas relative permeability inside the fracture, and, eventually, studied its impact on the gas production rate. The laboratory results showed that, based on the value of fracture conductivity, relative permeability of gas can vary between 0.05 and 0.8. The analysis of the field results showed that the cumulative gas production in 30 days increased seven-fold as a result of the improved gas relative permeability when 20/40 proppant was used instead of the 100 mesh proppant.

A case study from the Bakken shale was analyzed using an artificial neural network (ANN) model developed by Shelly et al. (2012) to identify the important parameters to identify the completion variables that have the most influence on the production performance. The model was validated, trained, and a sensitivity analysis

was done to select the optimum completion parameters. Among the parameters that showed a significant influence on the production were the number of fracture treatments, the proppant type, the perforation, and the staging lengths. The model results recommended reducing the treatment volume and the number of stages so that a higher fracture conductivity could be achieved. The recommendations were then applied to the actual completion design and resulted in a superior well performance of 36,000 bbls cumulative oil in one month. The ANN model was also used in another case where the effect of using Light Weight Ceramic (LWC) proppant over the sand proppant was investigated. The results showed an additional 50,000 bbls were produced using the LWC proppant.

The cost of fracturing represents 60-70% of the total well cost (Pope et al. 2012, Ran and Kelkar 2015). Therefore, the completion method needs to be carefully selected, including the selection of the casing and wellhead equipment to meet the fracturing needs. The main parameters that impact the fracturing operation are injection rate, treating pressure, the stimulation volume, number of stages, and type of perforation, fluid and proppant. The field results from 1800 wells that have been completed and stimulated in the Eagle Ford shale of North America were reviewed by Pope et al. (2012). The successful and unsuccessful treatments were analyzed, and a method to determine the best completion practices was discussed. Using history-matched data from an Eagle Ford well, the preliminary modeling studies done by Bazan et al. (2010) suggested that increasing the conductivity of fracture will generally increase the production from the Eagle Ford shale; upgrading from sand proppant to resin-coated

sand increased the cumulative gas production after three years by 100%, while upgrading to ceramic proppant increased the cumulative production by 150%. The actual field results were studied by Pope et al. (2012); 254 wells with 12 months production data were identified and divided into wells with ceramic proppants and wells completed with other types of proppants. The wells with ceramic proppant showed an incremental increase in cumulative production of 35%. It was estimated that ceramic wells have generated $1.5 million USD additional value per well in the first year (assuming $4 USD/mscf and $80 USD/bbl). The additional cost of using ceramic proppant over sand or resin-coated sand was recovered in less than one year. Analysis of 400 newer wells has shown greater conductivity impact. After six months, the wells with ceramic proppant showed an incremental increase in cumulative production of 65% and $1.7 million USD additional value per well was generated.

In another study by a different operator done on the same area, it was reported that a 30-50% increase in production was achieved after six months in a well completed with 40/80 Light Weight Ceramic (LWC) compared with three offset wells completed with sand proppant. The equivalent benefit is estimated to be $1.4 million USD more than the cost of higher cost ceramic proppant (Saldungaray and Palisch 2012). Most of the completion and production data from Eagle Ford supported the technical and economic benefits from improving the fracture conductivity by using higher-quality proppant (Pope et al. 2012).

Palisch et al. (2012) presented results from laboratory experiments which explain the effect of downhole conditions on the proppant performance, including the effect of

embedment, fines migration, and elevated temperature. Fracture modeling studies and analysis of actual field data from three shale plays were used to optimize the completion process. Case histories showed the successful implementation of the proposed optimization method in the Haynesville, Eagle Ford, and Bakken shale plays. Using the most up to date prices, the upgrade from resin-coated sand proppant to ceramic proppant for the "tail-in" stage, which was 40% of the treatment volume, has increased the fracturing treatment cost in the Haynesville shale gas by $250,000 USD per well. However, the incremental production increase has paid out the additional cost in less than three months, even though the gas price was relatively low at that time. After 32 months, an incremental increase in cumulative gas was 0.5 Bcf per well which is equivalent to $1.8 million USD base on the gas price at that time ($3.5 USD/Mcf). After 20 years, the hyperbolic decline model indicated an increase in cumulative gas by 35%. The cost of upgrading to ceramic proppant ($250,000 USD) eventually resulted in a 10-fold return on investment (Palisch et al. 2012).

In Eagle Ford shale, the modeling studies suggest that production and economic gains would be achieved using improved fracture conductivity (Bazan et al. 2010). The modeling results were verified through field implementation by Palisch et al. (2012). The production benefits from using higher-quality proppant was not significant in the first six months, as early production data was dominantly controlled by reservoir contact and high reservoir flowing pressure. However, after 12 months, the production from wells with LWC showed a significant difference than well with sand proppant. The effect of proppant type on well production is magnified with time, due to the decrease in

fluid flowing pressure and increase in the stress on the proppant with time (Bazan et al. 2012). After 12 months, wells with LWC have produced 15 MMscf incremental gas per fracturing stage than wells completed with sand proppant. Assuming gas price of $3.7 USD/Mscf and $75 USD/barrel oil, the production increment is equivalent to $1.5 million USD per well after 12 months and paid out the increased proppant investment in 9 months (Palisch et al. 2012).

The benefits of improved fracture conductivity on well production performance are not limited to the gas and liquid-rich gas shale reservoirs. Field analysis has also shown its profitability in the shale oil reservoirs. In the study of Palisch et al. (2012), the analysis of the completion and production data of 22 wells from the Bakken shale oil showed that the use of LWC proppant has increased the cumulative oil production after 22 months by 34%. Palisch et al. (2012) showed that all three shale plays (Haynesville, Eagle Ford, and Bakken) have experienced production benefits from the improved fracture conductivity achieved through using a higher-quality proppant. The analysis of the cost of achieving higher conductivity versus its benefits has shown its economic profitability. It was shown that the additional cost is recoverable with in the first year of production. Therefore, increasing fracture conductivity generously increases the investment.

Chapman and Palisch (2014) reviewed the field results from the Eagle Ford and the Bakken shale; and verified that increasing fracture conductivity increases production. In the Eagle Ford shale, the authors compared the production performance from the wells completed with high fracture conductivity, using lightweight ceramic (LWC)

proppant, to the wells of low fracture conductivity, completed using sand proppant. The comparison was done in two aspects: a broad area, where all wells were completed by a single operator in one county, and an offset pair, where two offset wells were completed at the same time with similar completion techniques, except for one variable, which was the proppant type. The predictive models suggested that the wells were conductivity-limited and the production would increase if the fracture conductivity was enhanced. The actual field results confirmed the results of the predictive models; wells completed with LWC experienced an increase in the cumulative gas production of 50,000 barrel oil equivalent (BOE) in the first six months, compared to the wells completed with the sand proppant. Although the operator company has saved $1 million USD by replacing the LWC with the sand proppant, wells with the LWC generated, on average, an incremental $1.8 million USD per well from the incremental increase in the production after only six months. In the offset pair study, two wells offset to each other in the same county and were drilled, completed, and produced with the same manner. The high conductivity well was completed with the sand proppant with a tail-in of LWC, while the low conductivity well was completed with the sand proppant with a tail-in of resin-coated sand proppant. The saving from changing the proppant type was estimated to be $500,000 USD. After 100 days of production, the high conductivity well produced 15% more oil and 11% more gas, resulting in an overall increase in BOE of 14%. The revenue increase was estimated to be $700,000 USD. The use of LWC would have generated $200,000 USD more revenue in just 100 days.

The cumulative oil production from a shale reservoir in CAPA field of North Dakota, of 0.0014 md permeability, has also shown an increase by one third from 120 to 180 million STB in the study of Sun and Schechter (2015) after 800 days of production. The increase in production resulted from the improvement of the fracture conductivity from 2 to 712 md-ft. The authors used a new integrated workflow for characterization and simulation of unconventional reservoirs. Sensitivity analysis was carried out to determine the role of fracture conductivity and the natural fractures. The study showed the importance of fracture conductivity in the long-term production performance of the unconventional reservoirs.

Tables 1.1 provides a summary of the reviewed studies that show the production and economic benefits from improving the fracture conductivity in shale reservoirs.

Table 1.1 Summary of the reviewed studies showing the production and economic benefits from improving the fracture conductivity in shale reservoirs. Reprinted from SPE-192451-MS.

Reference	Shale Formation	Reservoir type	Study Type			Approach	Impact
			Analysis of Field Results	Simulation Study	Laboratory Study		
Mayerhofer et al. 2006	Barnett	Gas		√		Increasing fracture conductivity from 0.5 md-ft to 20 md-ft	After 1800 days, the cumulative gas production increased from 700 to 3400 MMscf
						Increasing the near-well fracture conductivity from 5 to 20 md-ft	After 1800 days, The cumulative gas production increased from 1550 to 1700 MMscf
Rankin et al. 2010	Bakken	Oil	√			Increasing the number of fracturing stages and replacing the sand proppant with the ceramic proppant	After producing 50,000 barrels of the cumulative oil production, production rates increased from 105-250 bbl/day to 580-940 bbl/day
	Three Forks					The use of plug and perf stages and replacing sand proppant with ceramic proppant	The initial production rate, the production rate after 30 days of production, and the production rate after reaching a cumulative production of 48,000 bbls increased by 37%, 56%, and 70%, respectively
Bazan et al. 2010	Eagle Ford	Gas		√		Upgrading from the sand proppant to the resin-coated sand proppant	Increasing the cumulative gas production after 3 years by 100%
						Upgrading from the sand proppant to the ceramic proppant	Increasing the cumulative gas production after 3 years by 150%,
Mendoza et al. 2011	Eagle Ford	Gas		√		Increasing the fracture conductivity from 0.5 md-ft to 300 md-ft	An increase in the gas reserve from 5.6 Bscf to 9 Bscf (60% increase)
Vincent 2011	Eagle Ford	Oil	√			The use of the ceramic proppant instead of the sand or resin-coated sand proppants	The cummulative oil production in 12 months increased from 120,000 BOE to 167,000 BOE (39% increase)
Penny et al. 2012	shale gas	Gas	√		√	Improving the gas relative permeability inside the fracture by using 20/40-mesh size proppant	The cumulative gas production in 30 days increased seven-fold
Shelly et al. 2012	Bakken	Oil		√		The use of LWC proppant and increasing the number of fracturing stages	Additional 50,000 bbls were produced in one month

Table 1.1 Continued

Reference	Shale Formation	Reservoir type	Study Type			Approach	Impact
			Analysis of Field Results	Simulation Study	Laboratory Study		
Pope at al. 2012	Eagle Ford	Liquid Rich Gas	√			The use of ceramic proppant	An incremental increase in the cumulative production of 35% which generated $1.5 million USD additional value per well in the first year (assuming $4 USD/mcf and $80 USD/bbl). The additional cost of using the ceramic proppant has been recovered in less than one year
							After 6 months, an incremental increase in cumulative production of 65% which generated $1.7 million USD additional value per well (assuming $4 USD/mcf and $80 USD/bbl)
Saldungaray and Palisch 2012	Eagle Ford	Liquid Rich Gas	√			The use of 40/80 Light Weight Ceramic (LWC)	30-50% increase in the production after 6 months
Palisch et al. 2012	Haynesville	Gas	√	√	√	The use of ceramic proppant in the tail-in fracturing stage instead of the resin-coated sand	After 32 months, an incremental increase in the cummulative gas production of 0.5 Bcf per well ($1.8 million USD) has been achieved. Hyperbolic decline indicated a 35% increase in the cumulative gas after 20 years. Eventually, the cost of proppant upgrading has been returned 10-fold
	Eagle Ford	Liquid Rich Gas				The use of LWC instead of the sand proppant	After 12 months, the wells with LWC proppant have produced a 15 MMscf incremental gas per fracturing stage than the wells completed with the sand proppant. Assuming a gas price of $3.7 USD/Mscf and $75 USD/bbl, the production increment is equivalent to $1.5 million USD per well after 12 months and paid out the increased proppant investment in 9 months
	Bakken	Oil				The use of LWC proppant instead of the sand proppant	The increase in the cumulative oil production after 22 months by 34%
Chapman and Palisch 2014	Eagle Ford	Gas	√	√		The use of Lightweight ceramic (LWC) proppant instead of the sand proppant	An increase in the cumulative gas production of 50,000 BOE in the first 6 months. The use of LWC generated $200,000 USD more revenue in just 100 days
	Bakken	Oil					An increase of 36,000 bbls in the cumulative oil production after one month
Sun and Schechter 2015	CAPA Field	Oil		√		The improvement of the fracture conductivity from 2 to 712 md-ft	The cumulative oil production increased by one third from 120 to 180 million STB

The reliance of well production performance on the fracture conductivity, in spite of the ultra-low matrix permeability of shale formations, could be explained by two main reasons.

Firstly, the fracture conductivity is not as high as it is usually assumed, considering the multiple damaging mechanisms to the fracture conductivity at downhole conditions of shale formations. **Figure 1.2** shows a comparison between the laboratory measured baseline conductivity and the downhole conductivity at the Eagle Ford shale downhole conditions for 40/80 LWC, 40/70 RCS, and 40/70 white sand proppants (Bazan et al. 2012). All proppants tested experienced a significant conductivity loss at the downhole conditions (93, 94, and 97%). The limited fracture conductivity at the downhole conditions was not only shown by laboratory experiments but it was also confirmed by the modeling studies and the field observations by Bazan et al. (2010).

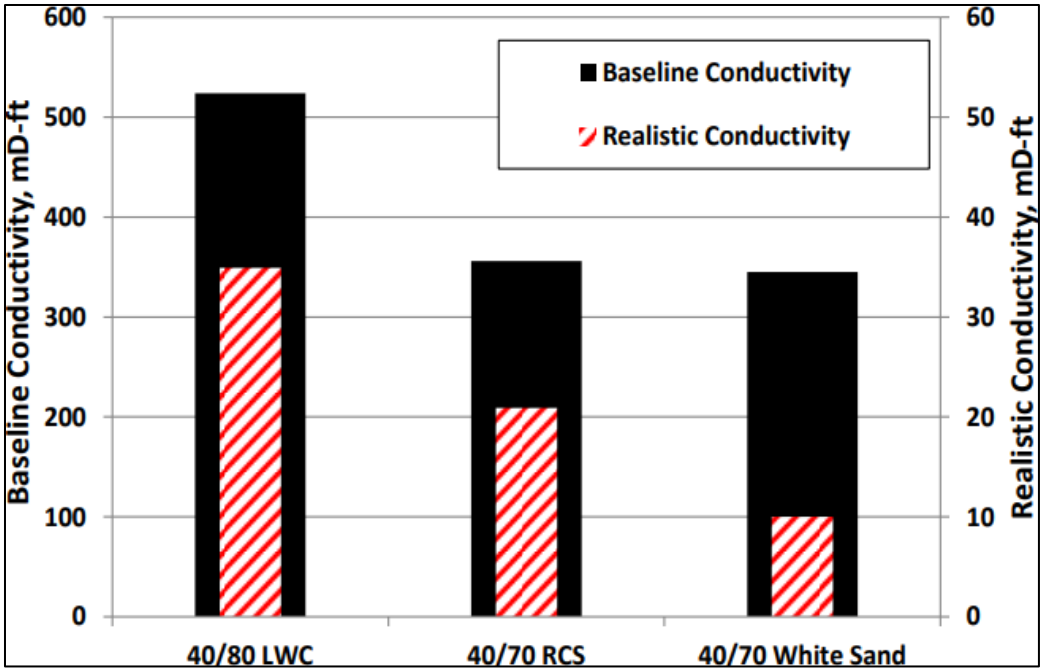

Figure 1.2 Comparison between the baseline conductivity and the downhole conductivity for 40/80 LWC, 40/70 RCS, and 40/70 white sand proppants at the Eagle Ford shale reservoir conditions (Bazan et al. 2012).

Secondly, the effective formation permeability is not as low as the matrix formation permeability, considering the secondary microfracture networks that branch from the main propped fracture and enhance the flow of hydrocarbon to the main fracture, and, thus, improve the formation effective permeability.

Figure 1.3 illustrates the drainage pattern of the hydraulic fractures and the concept of the effective formation permeability presented by Song et al. (2011). The complex fracture network created by hydraulically fracturing the shale formations can be represented by multiple main propped fractures, in which each main fracture drains a separate isolated region with no-flow boundaries separating the regions drained by each fracture. The minor fractures that branch from the main fracture can be taken in account

by calculating an effective formation permeability that includes the improvement in matrix permeability due to the presence of the microfracture network. **Figure 1.4** illustrates the created complex fracture network due to the horizontal multiple fracturing of shale formations and the concept of the effective formation permeability. Accordingly, if one considers these factors in the calculation of fracture and effective formation permeability, the fracture-to-formation conductivity ratio would significantly be reduced to the range that makes the well production performance sensitive to the conductivity of the main propped fracture.

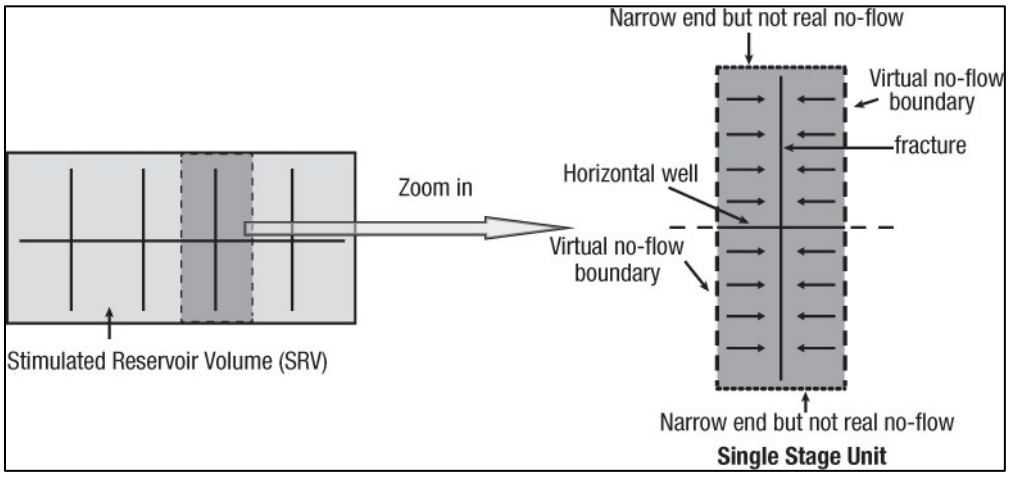

Figure 1.3 The drainage of multiple transverse fractures in horizontal wells (Economides et al. 2012, modified after Song et al. 2011).

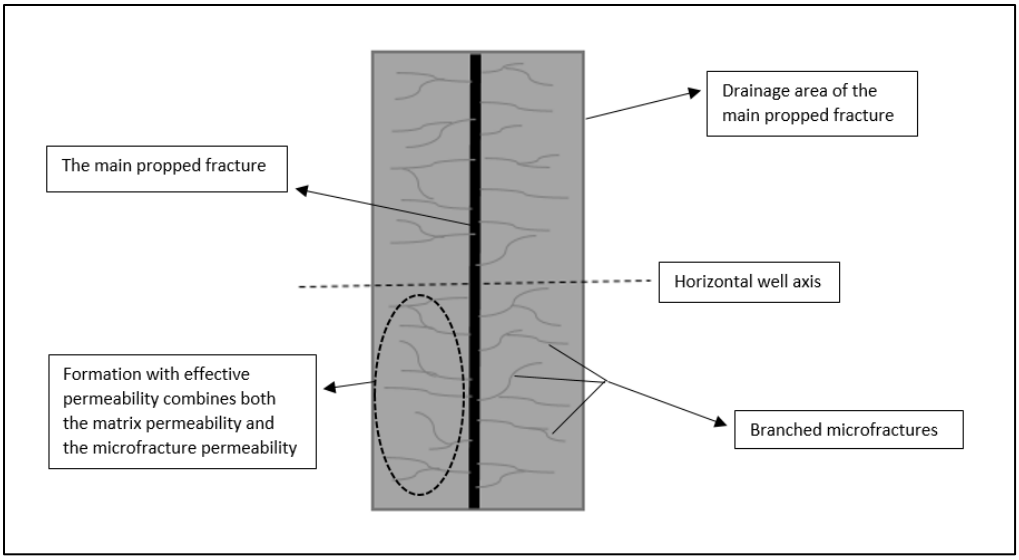

Figure 1.4 The created fracture network in shale formations and the concept of effective formation permeability. Reprinted from SPE-192451-MS.

1.2. Laboratory Measurement of Fracture Conductivity

Fracture conductivity is measured experimentally for different proppant types and concentrations, and at different closure stress values. The API recommended practices (RP) are available for the test procedures and conditions. The need for the laboratory testing of the proppant has started with the early use of the hydraulic fracturing as a well stimulation method. The operator companies have designed several laboratory tests to evaluate the proppant performance at the downhole conditions to relate the proppant properties to the well production performance (Gidley et. al. 1989). The proppant testing was also necessary for the design of the fracturing treatments, by the service companies, and for the quality control and the marketing of the proppants, by the different supplier companies (Duenckel et al. 2016). There are sets of API/ISO standards to evaluate and report the fracture conductivity on the short and long term time

scale (API 61, modified-API 61, and API 19D). The first API standard (API 61) was issued in 1989 and it is known commercially as the short-term conductivity. While the most recent one is the API 19D, published in 2008, and it is known as the long-term conductivity. The API standard conductivity cell is used in the test to allow the flow of the fracturing fluid through the proppant pack and measure the pressure drop across the fracture and the leak off rate to the rock sample. The proppant is packed between two Barea sandstone platens, and the in-situ stress is applied mechanically by the use of a load frame. The width of the fracture is measured by a displacement sensor mounted to the hydraulic press piston. The fracture conductivity, the fracture permeability times its width, can subsequently be calculated. The API standards require the use of a proppant concentration of 2 lb/ft^2 and the use of 2 wt% KCl water as the flowing fracturing fluid. The API standard tests provide a simple procedures with repeatable results to be used for the comparison of different types of proppant.

As mentioned in the API 61 document, the API standards were not designed to reproduce the exact in-situ conditions. Therefore, correction factors should be used to estimate the more realistic fracture conductivity that takes into account more representable downhole conditions, such as, the loadings other than 2 lb/ft^2, the different formation type, the multiphase and non-Darcy flow, and the damage from the fracturing fluid residues.

The value of the fracture conductivity is crucial to the fracture design and reservoir simulation processes, therefore, special laboratory testing at representable downhole conditions is necessary for the accurate evaluation of the proppant

performance inside the formation fractures. The first initiative to address this challenge was done in 1987, by a consortium of 20 companies (operators, service companies, and proppant suppliers) to provide a systematic approach for the fracture conductivity corrections. Several laboratory and field studies were conducted to address each fracture conductivity-damaging mechanism and the required correction technique for each one (Barree et al. 2003; Chapman and Palisch 2014; Duenckel et al. 2016). The total reduction percentage in the fracture conductivity after considering all the contributing factors can be as high as 97% (Chapman and Palisch 2014). Therefore, the laboratory measured API conductivity should be corrected to take into account the main conductivity-damaging mechanisms, which are summarized in the following section.

1.3. Damaging Mechanisms to Fracture Conductivity

We classified the damaging mechanisms of propped fracture conductivity at downhole conditions into fluid/flow-related and proppant-related, based on the source of damage. The following section discusses the sources of each damaging mechanism.

1.3.1. Fluid/Flow-Related Mechanisms

1.3.1.1. Fracturing Fluid Damage

The effect of the fracturing fluid residue after breaking on the fracture conductivity was fully studied for the development of tight-gas reservoirs by the early 1970's. For the development of the ductile shale oil formations, injecting a high-viscosity fracturing fluid with a high proppant concentration was found to be the optimum completion strategy for several fields. This strategy is in contrast to injecting high volumes of low viscosity fracturing fluids to create a complex fracture network,

which is usually used for brittle shale formations. To achieve a high-viscosity fracturing fluid, a gelling agent, including polymers or surfactants, should be added to the fracturing fluid Formula. The polymers increases the viscosity of water to 10's cp range; however, the addition of crosslinkers to the fluid system can increase the viscosity to 100's or even 1000's cp range. For the fracturing fluid flowback purposes, delayed breakers are usually added to the fluid system to break the polymer bonds and reduce the fluid viscosity to improve the fracturing fluid flowback efficiency. The breaking mechanism of the polymers precipitates polymer residues inside the fracture, which could plug the pore throats of the proppant pack, and hence, reduce the fracture permeability.

With the aid of SEM (Scanning Electron Microscope), Cooke (1975) demonstrated the precipitation of guar polymer residues on the surface of sand proppant grains. The author presented a new model to calculate the change in porosity due to fluid residues and the resulted reduction in pore volume. The Kozeny Model was then modified to account for the change in the porosity and relate it to the change in the packing permeability. The permeability reduction was also confirmed by conducting fracture flow experiments and monitoring the pressure drop across the fracture. The reduction in permeability was shown in some cases to be as large as 50%. As presented in the results of that study, the subsequent reduction in the fracture conductivity could reach 90%. There have been extensive studies in the literature to develop new fluid systems with a minimum residue after breaking, including the use of synthetic polymers,

guar derivatives, and viscoelastic surfactants (Nasr-El-Din and Samuel 2007, Hua et al. 2016, Elsarawy et al. 2016, Ibrahim at al. 2016, Ozden et al. 2017).

1.3.1.2. Multiphase Flow

The baseline conductivity is measured using a single-phase flow regime (2 wt% KCl); however, it is expected that multi-phase flow of oil, gas, and water occurs inside the fracture at downhole conditions. The relative permeability of each phase as a function of the fluid saturation need to be experimentally determined by simultaneously flowing oil, gas, and water through the proppant pack. Each fluid experiences a higher pressure drop in the case of multiphase flow, which also can be more influential if coupled with the pressure drop of the non-Darcy flow.

1.3.1.3. Non-Darcy Flow

The API standard tests measures the fracture conductivity at a flow rate of 2 ml/min, which corresponds to the Darcy's flow condition. This flow rate is equivalent to an oil production at a rate of 6 barrels per day, in a fully perforated vertical well with a bi-wing fracture of 50 ft length and using 2 lb/ft^2 proppant concentration. In dry gas wells, it is equivalent to 15 Mscf/day. An additional pressure drop is expected if the fluid flow velocity exceeded the critical velocity and the flow converted to the non-Darcy flow status. Forchheimer (1901) provided the modified Darcy flow equation to account for the high velocity flow conditions, the presented equation showed that the total pressure drop is controlled by the Darcy pressure drop as a function of the fluid viscosity and velocity, in addition to an additional pressure drop term as a function of the square of the velocity term.

Penny and Jin (1995) and Olson et al. (2004) expanded the Forchheimer equation to apply it to the different oil and gas field practices. Generally, the higher the flow rate, the more pronounced the effect becomes. The non-Darcy flow can cause 25%-60% additional pressure drop than those calculated using Darcy's law (Smith and Montgomery 2015). The multiphase flow and non-Darcy flow can be minimized by optimizing operational techniques through a) the use of spherical proppants instead of angular ones, b) the use of the large mesh size ceramic proppants, or c) maximizing fracture width through a high proppant concentration.

1.3.1.4. Asphaltene Precipitation

As a result of the pressure and temperature changes inside the fracture, asphaltene could precipitate from the crude oil which leads to the reduction of the fracture permeability. Asphaltene precipitation refers to the settling of solid particles from the crude oil onto the rock surface. Such precipitation will induce alteration in the rock wettability, in addition to, plugging the pore spaces available for the flow of hydrocarbons. Hence, a reduction in the fracture conductivity is expected if the asphaltene precipitation was not mitigated.

1.3.2. Proppant-Related Mechanisms

The following are the damaging mechanisms that are sourced from, and associated with, the use of proppant in the hydraulic fracturing process.

1.3.2.1. Proppant Crushing and Compaction

The stress applied to the proppant at in-situ conditions reduces the proppant strength and cause its crushing and failure (Stephens et al. 2007). The proppant crushing process leads to the compaction of the proppant pack and the reduction of the fracture width and the proppant porosity. The proppant crushing also generates fines which are mobile and plug the pore throats of the proppant pack. Subsequently, a fracture permeability loss is expected.

The evaluation of fracture width and proppant porosity reductions due to the crushing and compaction process can be done using the proppant laboratory testing data of the API RP19C and API RP19D reports as explained in the following two paragraphs.

The proppant physical properties, including the proppant bulk density, is usually reported in the proppant data sheet provided by the proppant supplier company (World Oil 2015). The reported value of the proppant bulk density is measured according to the API RP19C standard. The procedures is done by allowing the proppant to fall freely from a funnel, under the effect of the gravitational force, to fill a certain volume of a cylinder. The proppant mass required to fill the cylinder is then used to calculate the proppant bulk density. The calculated value can then be used to calculate the proppant pack porosity a no-stress condition. The proppant porosity calculated using the API RP19C data does not represent the actual value at the downhole conditions. The earth in-situ stresses causes a significant proppant compaction, crushing, and embedment inside the formation fractures (Chapman and Palisch 2014), subsequently, the proppant porosity could be significantly reduced. The use of an enlarged value of the proppant

porosity in the fracture design and the well production modelling has been reported by some studies which could be misleading (Marongiu-Porcu et al. 2008, Zhang et al. 2010, Jangda et al. 2014, Economides et al. 2002, Bhattacharya and Nikolaou 2016). The proppant porosity needs to be estimated at more representable conditions.

The data from the proppant conductivity test (API RP19D) is commonly used to estimate the proppant porosity under stress conditions. The test results include the change of the proppant pack permeability and width at different stresses. The measured fracture width can be used with the proppant mass and density to calculate the proppant porosity inside the fracture. The fracture width, in the API RP19D test, is measured using a Linear Variable Displacement Transedcucer (LVDT) which is mounted to the hydraulic press piston.

1.3.2.2. Proppant Embedment

Proppant embedment is the reduction of the fracture width around the proppants by the action of the closure stress. The problem is described by the schematic shown in **Figure 1.5**. Proppant embedment is more significant in the ductile shale formations than in brittle formations.

Wen et al. (2007) studied experimentally the effect of the different types of proppants on the degree of embedment in different cores and its negative impact on the fracture conductivity. The API conductivity cell was used to run the conductivity measurement experiments. Actual field core slices (8 samples covering different range of elasticity) were used in the test to simulate the fracture surface and evaluate the degree of proppant embedment. The results were compared to the no-embedment case,

where the fracture conductivity was measured at identical conditions but with the use of steel plates. Two proppants of different diameters were tested, 20/40 and 30/60 mesh sizes. The fracture conductivity was evaluated at different closure stresses, and each test lasted for 50 hr. The results showed the presence of a critical closure stress after which the proppant embedment starts to significantly reduce the fracture conductivity. Below the critical stress value, the fracture conductivity of both cases was identical and the proppant embedment showed no effect. The degree of the conductivity reduction varies with the proppant type and formation characteristics; the maximum reported conductivity reduction is 87.5% which corresponds to the results of the most ductile formation and the smaller proppant size.

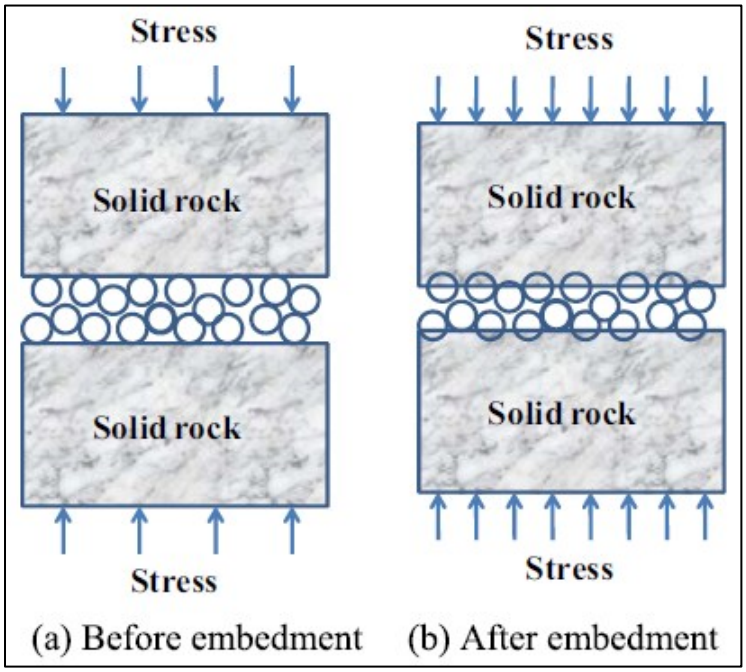

Figure 1.5 Schematic of proppant embedment process (Chen et al. 2016).

Alramahi and Sundberg (2012) presented an analytical model to predict the degree of the proppant embedment and the stress-dependent fracture conductivity by the aid of a designed proppant embedment laboratory test. The embedment was quantified at different stresses for different mineralogy and mechanical properties of shale samples. The author concluded the variation of the degree of embedment based on the degree of the stiffness of the shale sample. The stiff samples showed a reduction in the fracture conductivity of one order of magnitude, while the ductile samples showed a reduction of six orders of magnitudes. The study highlights the importance of measuring a representable shale mechanical properties (Young's modulus and Poisson's ratio) at downhole conditions, which enables a better prediction of the effect of the proppant embedment process.

1.3.2.3. Proppant Diagenesis

Proppant dissolution was observed in the 1980's from the analysis of the effluent fluid from proppant conductivity flow test (Becq et al. 1984; McDaniel 1986; Penny 1987). The presence of the silicon ion was the key indicator of the proppant dissolution. The term, proppant diagenesis, however, was first used by Weaver et al. (2005). The proppant diagenesis refers to the formation of overgrowth minerals due to the interactions between the fluid, the proppant, and the formation. The overgrowth was observed as a porosity filling material in the proppant pack after a long-term conductivity testing of ceramic proppant between two Ohio sandstone wafers. The Si/Al ratio was used to differentiate between the proppant, the formation, and the new formed overgrowth material, which was identified as a zeolite mineral.

The pressure-solution and compaction mechanisms were considered as the main mechanism of proppant diagenesis reactions (Weaver et al. 2006). The earth diagenesis occurs over the geological time when the permeable unconsolidated sand particles are buried under high overburden stress and temperature. A subsequent cement material is formed between the sand particles at the grain to grain contacts. Through the geochemical reactions, the high permeable sand beds convert to a lower permeability beds due to the formation of the porosity filling materials. As an analogue to the geological diagenesis, the modeling studies show that the diagenesis of proppant in the formation fractures occurs in a period of time that could be a fraction of a year (Yasuhara et al. 2003; Weaver et al. 2007). The proppant diagenesis can be reasonably observed in the lab by accelerating the involved reactions through the use of temperature-promoted tests, which enable the diagenesis to take place over several weeks (Weaver et al. 2008).

The proppant diagenesis process depends on the mineral composition of the proppant and the formation (Nguyen et al. 2008). The dissolution and the overgrowth rates are controlled by the temperature and stress conditions. Higher rates are expected at higher temperature and stress. The aluminum-based and zirconium-based proppants are the main types that undergo a significant diagenesis (Weaver et al. 2009). Various aluminosilicate (zeolite) minerals were observed in previous studies as a result of the proppant diagenesis process. The type of the overgrowth mineral depends on the type of proppant, the chemical composition of water, and the mineralogy of the formation in contact with the proppant. Weaver et al. (2009) reported the formation of needle, bi-

pyramidal, and tabular-shaped crystals when four different types of ceramic proppants were mixed with silica-rich shale formation in deionized water at 500°F for one to two months. A variety of zeolite and clay minerals were identified with the aid of Energy Dispersive X-ray Spectroscopy (EDS) analysis. The proppant coating with hydrophobic film, hardening or non-hardening resins, was found to reduce the effect of proppant diagenesis and provide an improved fracture conductivity with long-term impact (Weaver et al. 2010). The proppant diagenesis was also observed in the lab at realistic reservoir conditions by Raysoni et al. (2013). The heating of a static-cell containing a mixture of a high strength bauxite proppant with a low-permeability sandstone formation at 300-450°F resulted in the formation of zeolites after a period of time varied from 15 to 180 days. The volume of the mineral overgrowth was found to increase with time. The tested proppant-pack cells showed a significant reduction in its permeability after the aging. The single-grain crush tests also indicated the reduction of the proppant strength after diagenesis.

An experimental procedure using pressure bombs was developed by LaFallotte and Carman (2010) to investigate the proppant diagenesis in the presence of the formation water and the fracturing fluid solutions. The diagenesis of high-strength, intermediate-strength, and low weight ceramic proppants were tested in the presence of Haynesville shale. The procedure requires the use of two formation samples cut in the shape of a coin (1 in. diameter and 0.3 in. thickness). The proppant is sandwiched between the two samples and the assembly is placed in a pressure bomb (23 ml volume) and filled with the fluid solution at 70 psia. The bomb is then aged at 300°F for 30, 60,

120, and 240 days. Testing several types of ceramic proppants confirmed the diagenetic activity of the proppants at various periods of time. The composition of the fluid was tested and indicated a variation in the ions' concentrations at different times. The increase in Ca, Si, Cl, and HCO_3^- ion concentrations followed by a subsequent reduction indicated the occurrence of the precipitation after dissolution reaction. Crystals of $CaCO_3$, $CaSO_4$, $BaSO_4$, and NaCl were observed on the majority of the proppants. Minor deposits of Ca and Mg silicates were observed underneath the proppant only after 240 days. There was a wide range of the impact of the diagenetic reactions on the different proppants after being exposed to the formation water and fracturing fluid solutions of different compositions and pH values. The sand proppant showed a minimal or no effective reactions, while intermediate strength proppant showed the greatest degree of reaction (LaFallotte and Carman 2011).

The effect of diagenesis on the proppant conductivity inside the formation fractures was questioned by Lee et al. (2009; 2010). Experimental and analytical models were used to calculate the reduction of the porosity and permeability of the proppant pack. After 1000 days, the reduction in porosity was found to be 25%. The subsequent reduction in permeability was estimated to be in the range of 25-75%, depending on the formation temperature. Hence, the proppant diagenesis mechanism could explain the long-term deterioration of fracture conductivity that is observed in both the lab and the field tests (Weaver et al. 2009).

The source of the precipitated materials was further investigated by Dunckel et al. (2011; 2012) after raising the doubt that the observed overgrowth minerals could be

explicitly sourced from the formation. The authors tested high-strength ceramic, light-weight ceramic, sand, and resin-coated sand proppants with four types of formations: Pinedale shale, steamboat, and two Haynesville/Bossier cores. The proppant and formation mixtures were mixed and aged in a deionized water at 400°F for 7 to 154 days. Several diagenesis precipitates were observed on both the proppant and the formation surfaces. The precipitates were identified as zeolites and were found associated with most of the proppant types in the presence of the formation material. After testing an inert steel proppant, the results suggested that the formation is the only source of the precipitants and the proppant has no contribution to the interactions. Furthermore, there was no evidence that chemical treatment or coating the proppant surface is effective to mitigate the observed zeolite precipitation. However, Raysoni et al. (2012; 2013) and Aven et al. (2013), reported afterwards the observation of the zeolite and the diagenetic overgrowth materials even in the absence of the formation materials, which indicated the contribution of the proppant in the interaction process.

1.4. Completion Design for Hydraulic Fracturing Shale Reservoirs

The success of Mitchel Energy Corporation to economically develop the Barnett shale reservoir was the start of the development campaign of multiple shale oil and gas formations in the U.S. The success key was the use of large volumes of slick water fracturing fluid along with applying advanced horizontal drilling techniques and massive hydraulic fracturing operations. The economic development of shale gas and oil reservoirs depends mainly on the success of the well completion strategy through both horizontal drilling and hydraulic fracturing operations.

The well completion strategies set by the operators started by following the same strategies used to develop the Barnett shale; however, production of some wells was not as successful as the Barnett (Ramurthy et al. 2011). It raised the doubt that the strategy of pumping large volumes of slick water fracturing fluid with low concentration of proppant might not be the optimum choice. The two main techniques for hydraulic fracturing are fracture packing and complex fracture network techniques. The fracture packing technique results in short and high conductive fractures and can be achieved by using a high proppant concentration carried by a highly viscous fracturing fluid. The fracture packing technique is favorable in the liquid-rich shale reservoirs, where fracture conductivity is critical to well productivity. On the other hand, shale gas reservoirs are completed by pumping large quantities of water carrying a low concentration of proppant. The increase in the reservoir access by creating a complex fracture network is the main objective in completing the shale gas reservoirs. For the advantageous of both techniques, a combination of the two completion strategies can also be used.

Accordingly, it is now well established that not every shale is similar to the Barnett, and completion optimization should be done based on formation properties, including mechanical properties, in-situ stresses, rock mineralogy, reservoir fluid properties, natural fractures network, and formation petrophysical and geological properties. For example, Barnett is considered as a brittle formation with a high Young's modulus, which makes the use of high volumes of water to create a complex fracture network a successful strategy. On the other hand, Eagle Ford is considered as a ductile formation with a moderate Young's modulus, which makes it prone to fracture closure

and loss of fracture conductivity due to proppant embedment. The proppant packing method of injecting high-viscosity fracturing fluid with high proppant concentration, provides a better completion strategy for ductile shale formations.

1.5. Problem and Study Objectives

The proppant used in hydraulic fracturing is currently selected in most shale plays based on the depth of the formation, commonly 5,000 ft is used as the critical depth, after which, the switch from using sand proppant to ceramic proppant occurs. It is also very common that the operator company selects the proppant type based on either the cost or the availability. While the proppant size has no clear selection criteria among the operator companies, the most commonly used size is the 100-mesh with the maximum possible amount of water.

We concluded from the presented review on the importance of fracture conductivity (section 1.1) and its significant damaging mechanisms at downhole conditions (section 1.3) that maximizing the fracture conductivity should be a priority in the fracturing design process. We suggest in this study that the proppant selection process be done based on the evaluation of the fracture conductivity damage associated with each proppant type and size. In order to do that, the proppant-related fracture conductivity damaging mechanisms need to be well understood, mathematically modeled, and related to the fracture conductivity calculations. Therefore, we address in the remaining sections of this dissertation, two main problems related to the evaluation of proppants and its associated damage to fracture conductivity.

1.5.1. Problem 1: Evaluation of Fracture Width and Proppant Porosity at In-Situ Conditions

As shown previously, to evaluate the proppant crushing and compaction mechanisms, the data from the API RP19C and API RP19D tests can be utilized to estimate the subsequent reduction in the fracture width and proppant porosity. However, the use of the API RP19C data does not simulate the actual downhole stress conditions. While the measurement of fracture width using the API RP19D data does not account for the displacement that occurs due to the compressibility of the rock under the applied stress. In addition, the API RP19D test is done using the Ohio sandstone sample at 2 lb/ft^2 proppant concentration which could behave differently than the actual formation rock and proppant concentration.

Therefore, the first objective of this study is to evaluate the propped fracture width and the proppant porosity of ceramic, sand, and resin-coated sand proppants inside the fractures of one of the shale formations that has the highest activities in the U.S., the Eagle Ford shale, using a new procedure that allows the direct measurement of the propped fracture width at simulated downhole conditions.

1.5.2. Problem 2: Evaluation of the Proppant Diagenesis Process

The reviewed literature about the proppant diagenesis mechanism shows that, at some conditions, it could induce a significant damage to the fracture conductivity. However, the source of the observed overgrowth and/or precipitated minerals is not fully understood in the literature, the involvement of the proppant in the chemical interactions is still a point of disagreement.

Therefore, the second objective of this study is to experimentally investigate the proppant diagenesis process in the hydraulic fracturing of Eagle Ford shale. The occurrence, type, and source of the overgrowth and/or precipitated minerals, associated with the most commonly used proppant types, including, ceramic, sand, and resin-coated sand proppants, are to be determined.

1.5.3. Study Objectives

The following list summarizes the main objectives of this study:

1. The measurement of the fracture width results from the use of the different sizes of the ceramic, sand, and resin-coated sand proppants at different concentrations and stress conditions inside the Eagle Ford shale fractures.
2. The evaluation of the proppant porosity for each type and concentration at different stress conditions up to 8,000 psia.
3. The evaluation of the proppant crushing mechanism associated with the use of each proppant type and concentration.
4. The identification of the precipitate and the overgrowth minerals that could be formed due to the proppant diagenesis process and the formation/fluid chemical interactions.
5. The determination of the degree of involvement of ceramic, sand, and resin-coated sand proppants in the proppant diagenesis process and the effect of their presence on the formation/fluid chemical interactions.

2. EXPERIMENTAL STUDIES*

2.1. Materials

The experiments were done using Eagle Ford shale outcrop samples, obtained from a local service company. The mineralogy of the core samples is shown in **Table 2.1**, as analyzed using the X-ray-diffraction (XRD) technique (BRUKER D8 ADVANCE, **Figure 2.1**).

Table 2.1 Mineral composition of the Eagle Ford shale samples.

Mineral	Concentration, wt%
Calcite	82.06
Quartz	10.87
Feldspar	4.78
Kaolinite	1.95
Pyrite	0.34

* Reprinted with permission from "Experimental Evaluation of Sand Porosity in Eagle Ford Shale Fractures" by A. Elsarawy and H. Nasr-El-Din, 2018. SPE-191240-MS, Copyright 2018 by Society of Petroleum Engineers. And permission from "An Experimental Investigation of Proppant Diagenesis and Proppant-Formation-Fluid Interactions in Hydraulic Fracturing of Eagle Ford Shale" by A. Elsarawy and H. Nasr-El-Din, 2018. SPE-191225-MS, Copyright 2018 by Society of Petroleum Engineers.

Figure 2.1 X-ray-diffraction equipment, BRUKER D8 ADVANCE.

The proppants used in this study were provided by a local proppant supplier company. Three proppant types and sizes were used, including sand, resin-coated sand, and ceramic at the size of 20/40, 40/70, and 100-mesh. **Table 2.2** summarizes the physical properties of the tested proppants, as provided by the supplier company.

Table 2.2 Physical properties of the tested proppants.

Proppant	Sand			Resin-Coated Sand		Ceramic	
Mesh-Size	20/40	40/70	100	20/40	40/70	20/40	40/70
Mean Diameter (mm)	0.54	0.30	0.18	0.54	0.33	0.73	0.35
Apparent Density (g/cc)	2.65	2.65	2.65	2.61	2.5	3.62	3.63
API-Bulk Density (g/cc)	1.54	1.54	1.54	1.47	1.41	2.1	2.06
Krumbein Sphericity	0.6-0.7	0.6-0.8	0.6-0.8	0.6-0.7	0.6-0.8	0.9	0.9
Krumbein Roundness	0.6-0.7	0.6-0.8	0.6-0.8	0.6-0.7	0.6-0.8	0.9	0.9

The ceramic proppant was analyzed using XRD and X-ray-fluorescence (XRF), BRUKER S2 RANGER, shown in **Figure 2.2**, to determine its mineralogy and elemental compositions, the results are presented in **Tables 2.3 and 2.4**. The sand proppant consists of >99 wt% quartz, as shown from the XRD analysis. The resin-coated

sand is coated with 5 wt% of the phenol formaldehyde resin, as provided from the supplier company.

Figure 2.2 X-ray-fluorescence equipment, BRUKER S2 RANGER.

Table 2.3 Mineral composition of the ceramic proppant.

Mineral	Concentration, wt%
Corundum (Aluminum Oxide)	49.74
Mullite (Aluminum Silicate)	37.69
Hematite (Iron Oxide)	5.75
Melanterite (Hydrous Iron Sulfate)	4.31
Ilmenite (Iron Titanium Oxide)	2.51

Table 2.4 Elemental composition of the ceramic proppant.

Element	Concentration, wt%
Al	41.7
Fe	34.8
Si	8.1
Ti	7.81
Zr	2.59
Mg	1.11
Mn	1.08
Ca	0.81

A de-ionized water with resistivity of 18.2 MΩ.cm at room temperature was synthesized using a water purification system (Thermo Barnstead RoDi, shown in **Figure 2.3**) and used in all experiments.

Figure 2.3 Water purification unit, Thermo Barnstead RoDi.

2.2. Preparation of an Experimental Propped Fracture Model

The Eagle Ford shale samples were examined visually for intact and samples with fractures or discontinuity were disregarded. The shale samples were drilled and cut into cylindrical cores 1.5 in. diameter and 0.5 in. length. Each core was longitudinally cut into two halves to produce two symmetrical rock surfaces, each surface has an area of 1.5 in. * 0.5 in. A high precision cutter (IsoMet BUEHLER, shown in **Figure 2.4**) is used to dry-cut the samples to produce two smooth and parallel surfaces. **Figure 2.5** shows an image of the two core halves after cutting which were used to prepare the propped fracture model.

Figure 2.4 IsoMet BUEHLER high precision cutter used to cut the core samples.

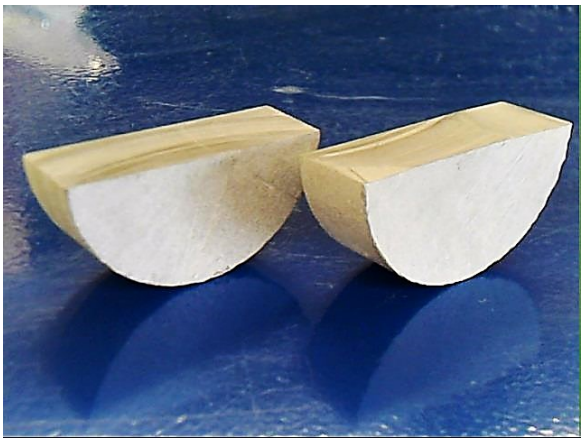

Figure 2.5 An image of the Eagle Ford core after cutting. Reprinted from SPE-191240-MS.

The two core halves were stacked together using an adhesive transparent tape. Ultra-thin glass slices, the thickness of each is 0.01 mm, were placed in-between the two cores halves before stacking to act as a spacer, and thus, allow a specified distance between the two core halves. A specified number of slices were used to produce an exact distance between the two core halves. For each proppant, the fracture model was

prepared with an initial porosity equals to the porosity calculated using the API-bulk density reported in the specification sheet (**Table 2.2**). Thus, the distance between the two core halves was chosen so that it produces the required initial porosity of the proppant. After solidating the model, the glass slices were removed and replaced with a weighted amount of proppant. The proppant was packed by filling the space between the two core halves with all the proppant amount.

Using this method, the initial fracture width at zero stress and the corresponding initial proppant porosity were controlled. **Table 2.5** summarizes the initial fracture width and proppant porosity of the 21 fracture models prepared using different proppants and concentrations. **Figure 2.6** shows an image of a propped fracture model after proppant packing. Finally, the fracture model was saturated with 2 wt% KCl water by imbibition for 24 hour to take in consideration the effect of water on the mechanical properties of the proppant and the shale formation.

Table 2.5 The initial fracture width and proppant porosity of the prepared fracture models of different proppants.

Proppant		ϕ_{pi} (%) *	W_{fi} (mm) Proppant Concentration, lb/ft^2		
			0.2	0.4	0.6
Sand	20/40	41.8	0.64	1.29	1.93
	40/70	41.8	0.64	1.29	1.93
	100	41.8	0.64	1.29	1.93
Resin-Coated Sand	20/40	43.6	0.68	1.35	2.03
	40/70	43.6	0.71	1.41	2.12
Ceramic	20/40	41.9	0.73	0.94	1.42
	40/70	43.2	0.48	0.96	1.45

* ϕ_{pi} = 1 - (API-Bulk Density / Apparent Density)

Figure 2.6 An image of the experimental propped fracture model. Reprinted from SPE-191240-MS.

The proppant concentration in slick-water and hybrid fracturing is estimated to be less than 1 lb/ft^2 (Palisch et al. 2012). In Eagle Ford shale, the hydraulic fracture modeling indicated that the proppant concentration inside the fractures is mostly in the range of 0-0.6 lb/ft^2 (Cook et al. 2014). Accordingly, the fracture models were prepared at three different proppant concentrations of 0.2, 0.4, and 0.6 lb/ft^2.

2.3. Measurements of the Propped Fracture Width under Stress

The closure stress is supplied by using a high-pressure cylindrical core holder with a Hassler rubber sleeve (**Figure 2.7**). The core holder is connected to a high pressure hydraulic pump to provide the required stress conditions. The fracture model is placed inside the core holder, and, under such conditions, it is subjected to a confining radial stress along its length. The core holder is modified to allow the imaging of the fracture model under stress. A high strength stainless steel tube is used inside the Hassler sleeve instead of the solid core outlet fittings. The stainless steel tube has a 1.5 in. outside diameter and 0.75 in. inside diameter. The main advantages of the tube are its

ability to hold the applied stress and to provide a conduit to access the fracture model under stress. Furthermore, a tempered glass disk (1.5 in. diameter and 0.25 in. thickness) was used to confine the fracture model to prevent the proppant to pop-out of the fracture under stress. The tempered glass has a high compressive strength and enables the imaging of the fracture model by its ability to transmit the light.

Figure 2.7 High-pressure cylindrical core holder with a Hassler rubber sleeve.

The stress is applied with a fixed-step of 1,000 up to 8,000 psia at the rate of 1000 psia/min. At each step, the propped fracture is imaged using a digital borescope that reaches to the model through the stainless steel tube. The borescope has a built-in LED light source and its magnification power is up to 400X. The images are acquired using a computer and analyzed using a software for fracture width measurement. At each stress, a waiting time is allowed for the fracture to reach stabilization before the image is acquired. The time needed for stabilization is between two and five minutes. **Figure 2.8**

shows a schematic of the propped fracture model, the tempered glass disk, and the stainless steel tube inside the core holder.

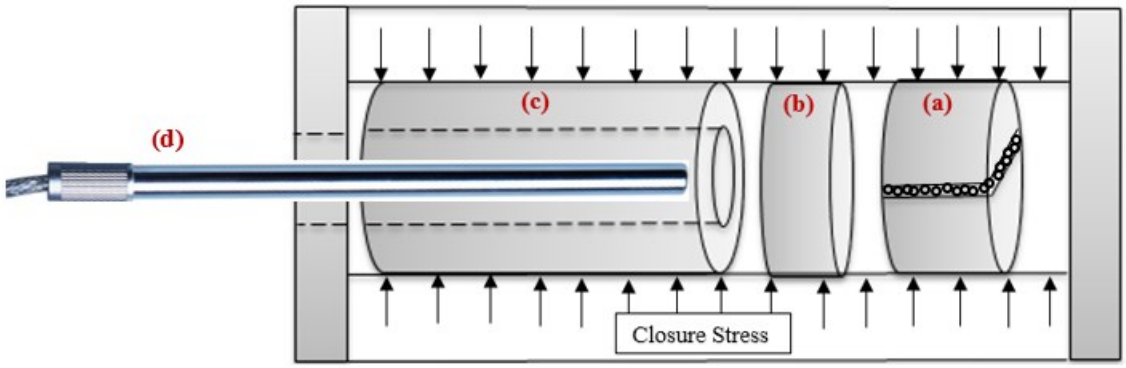

Figure 2.8 A schematic of (a) propped fracture model, (b) tempered glass disk, (c) stainless steel tube, and (d) digital borescope, all inside the core holder.

The software processes the acquired image of the fracture model to estimate the distance between the upper and lower boundaries of the proppant bed, which is considered as the fracture width at the specified stress. The image is converted to its negative copy, which includes the three basic colors: red, green and blue, and sharpened with a filter size and intensity of 10 and 50%, respectively. This procedure enables the viewing of the proppant edges and the upper and lower boundaries of the proppant bed. A horizontal line is then drawn at the boundaries and the perpendicular distance between the two lines is measured using a measurement tool in the software and considered as the propped fracture width. **Figure 2.9** illustrates the software processing stages of the acquired images for propped fracture width measurements under stress

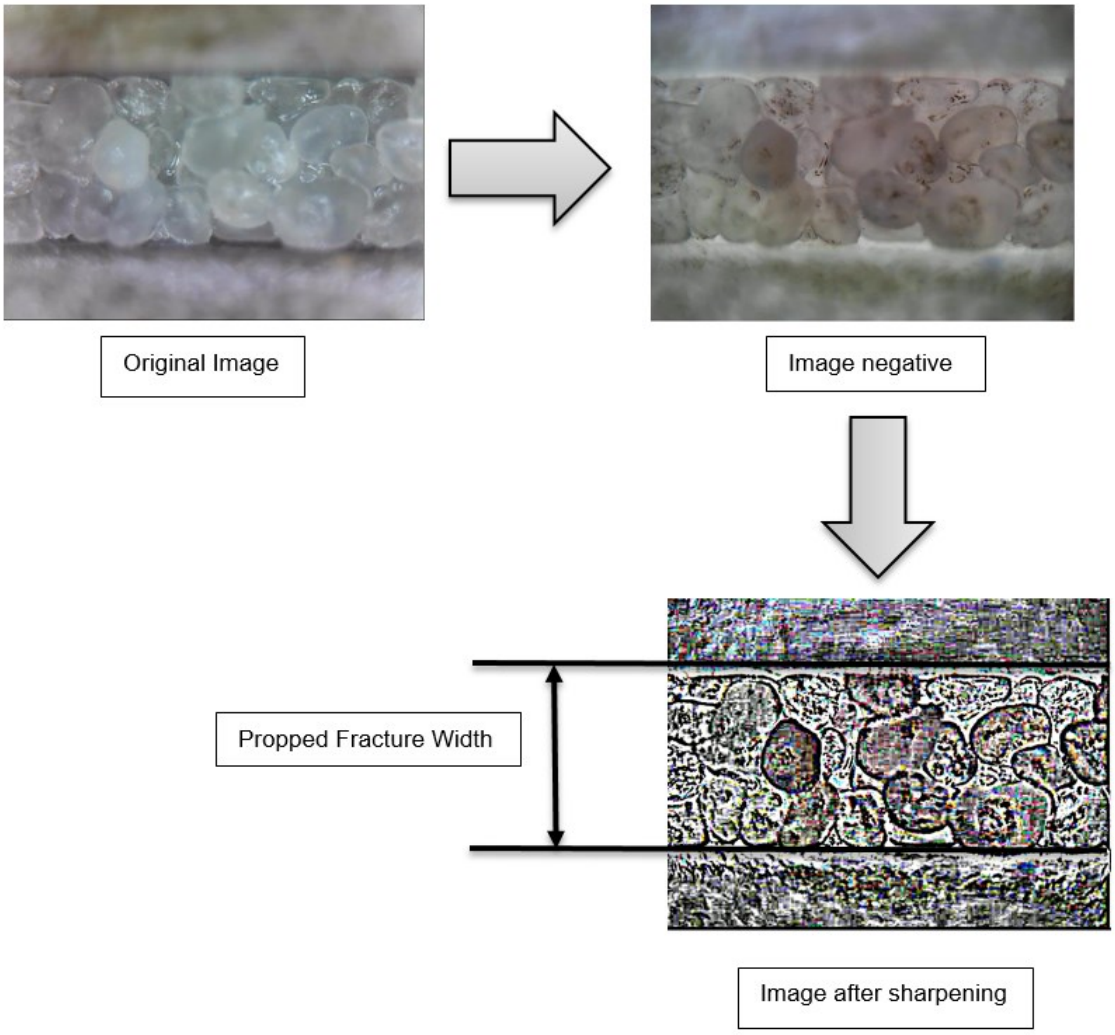

Figure 2.9 The software processing stages of the acquired images for propped fracture width measurements. Reprinted from SPE-191240-MS.

2.4. Calculation of the Proppant Porosity Under Stress

The measurements of the propped fracture width at each stress value were utilized to calculate the change in the proppant porosity under stress. By assuming that the proppant mass inside the fracture is constant for all stress values (the proppant mass lost due to embedment into the rock surface is neglected compared to the total proppant

mass inside the fracture), the change in the measured fracture width can thus be related to the reduction in the proppant porosity. The following equations summarize the porosity calculations at each stress step.

Proppant porosity (ϕ_p) by definition, is the ratio of the pore volume to the bulk volume of the proppant.

$$\phi p = \frac{V_P}{V_b} \ldots\ldots\ldots\ldots Equation\ (1)$$

Where, V_p is the proppant pore volume, and V_b is the proppant bulk volume

$$V_P = 1 - V_s \ldots\ldots\ldots\ldots Equation\ (2)$$

$$= 1 - \frac{M_P}{\rho_p}$$

Where, V_s is the solid volume of the proppant, M_P is the proppant mass, and ρ_p is the proppant density.

$$V_b = V_f = A_f * W_f \ldots\ldots\ldots\ldots Equation\ (3)$$

Where, V_f is the bulk volume of the propped fracture, A_f is the surface area of the propped fracture, and W_f is the measured fracture width.

2.5. Aging Cells

To investigate the proppant diagenesis process, the Eagle Ford formation samples were crushed using a vibratory disk mill (**Figure 2.10**) and sieved to a 50/100 mesh-size, using a sonic sifter separator (**Figure 2.11**). The proppants, including, ceramic, sand, and resin-coated sand, were sieved to a larger mesh-size of 20/40 to be easily separated after mixing with the formation. The proppant and formation were statically aged separately

and together in a stainless steel high-pressure/high-temperature (HP/HT) aging cell with a non-stick Teflon liner (OFITE style, shown in **Figure 2.12**). The cell volume is 500 mL and loaded with 10 gm proppant and/or 10 gm formation, and 300 ml deionized water. The cell was pressurized with nitrogen to 300 psia and placed in a static oven at 325°F for 3 weeks.

Figure 2.10 Vibratory disk mill.

Figure 2.11 Sonic sifter separator.

Figure 2.12 OFITE stainless steel HP/HT aging cell with a non-stick Teflon liner

2.6. Post-Aging Experimental Analysis

The proppant and formation were recovered after the aging, dried in an oven for 24 hours at 160°F, separated, and analyzed using a thermionic emission VEGA3 TESCAN scanning electron microscopy (SEM), with an energy dispersive X-ray spectroscopy (EDS), as shown in **Figure 2.13**. The supernatant samples were filtered and analyzed using Inductively Coupled Plasma Optical Emission Spectroscopy (ICP-OES) Optima 7000DV system, shown in **Figure 2.14**, and WinLab 32TM software to

determine the cations' concentrations. A spectrophotometer, SP600 Orbeco (**Figure 2.15**), was used to measure the sulfate concentration using the precipitation method.

Figure 2.13 VEGA3 TESCAN scanning electron microscopy with an energy dispersive X-ray spectroscopy.

Figure 2.14 Inductively Coupled Plasma Optical Emission Spectroscopy (ICP-OES) Optima 7000DV system.

Figure 2.15 Spectrophotometer SP600 Orbeco.

3. RESULTS AND DISCUSSION[*]

3.1. Measurements of Propped Fracture Width and Proppant Porosity

The fracture width and proppant porosity results are presented in **Tables 3.1 through 3.9**. As the closure stress increases, the fracture width and the proppant porosity decrease due to the compaction of the proppant bed resulting from the proppant rearrangement, the crushing of the proppant under stress, and the embedment of the proppant into the rock surface. The measured fracture width and porosity results from the combined effect of the three mechanisms.

[*] Reprinted with permission from "Experimental Evaluation of Sand Porosity in Eagle Ford Shale Fractures" by A. Elsarawy and H. Nasr-El-Din, 2018. SPE-191240-MS, Copyright 2018 by Society of Petroleum Engineers, and, "An Experimental Investigation of Proppant Diagenesis and Proppant-Formation-Fluid Interactions in Hydraulic Fracturing of Eagle Ford Shale" by A. Elsarawy and H. Nasr-El-Din, 2018. SPE-191225-MS, Copyright 2018 by Society of Petroleum Engineers.

Table 3.1 Fracture width and porosity of sand proppant at the concentration of 0.2 lb/ft^2. Reprinted from SPE-191240-MS.

Mesh-Size	**20/40**		**40/70**		**100**	
Closure Stress (psia)	**W_f (mm)**	**ϕ_p (%)**	**W_f (mm)**	**ϕ_p (%)**	**W_f (mm)**	**ϕ_p (%)**
0	0.6400	41.49	0.6400	41.49	0.6400	41.49
1000	0.6322	40.77	0.6192	39.53	0.5948	37.05
2000	0.6000	37.59	0.5799	35.43	0.5809	35.54
3000	0.5940	36.96	0.5590	33.02	0.5739	34.76
4000	0.5730	34.65	0.5433	31.08	0.5704	34.36
5000	0.5440	31.17	0.5399	30.65	0.5635	33.55
6000	0.5380	30.40	0.5333	29.79	0.5635	33.55
7000	0.5087	26.39	0.5299	29.34	0.5565	32.72
8000	0.4990	24.96	0.5290	29.22	0.5446	31.25

Table 3.2 Fracture width and porosity of sand proppant at the concentration of 0.4 lb/ft^2. Reprinted from SPE-191240-MS.

Mesh-Size	20/40		40/70		100	
Closure Stress (psia)	W_f (mm)	ϕ_p (%)	W_f (mm)	ϕ_p (%)	W_f (mm)	ϕ_p (%)
0	1.2900	41.95	1.2900	41.95	1.2900	41.95
1000	1.2518	40.18	1.2210	38.67	1.1849	36.79
2000	1.2210	38.67	1.2170	38.47	1.1725	36.13
3000	1.2090	38.06	1.1988	37.53	1.1602	35.46
4000	1.1750	36.27	1.1660	35.77	1.1540	35.11
5000	1.1600	35.44	1.1578	35.32	1.1417	34.41
6000	1.1200	33.14	1.1441	34.54	1.1293	33.69
7000	1.0990	31.86	1.1305	33.76	1.1232	33.33
8000	1.0653	29.70	1.1031	32.11	1.1170	32.96

Table 3.3 Fracture width and porosity of sand proppant at the concentration of 0.6 lb/ft^2. Reprinted from SPE-191240-MS.

Mesh-Size	**20/40**		**40/70**		**100**	
Closure Stress (psia)	**W_f (mm)**	**ϕ_p (%)**	**W_f (mm)**	**ϕ_p (%)**	**W_f (mm)**	**ϕ_p (%)**
0	1.9300	41.79	1.9300	41.79	1.9300	41.79
1000	1.7710	36.57	1.9048	41.03	1.9212	41.53
2000	1.7558	36.02	1.8858	40.43	1.8947	40.71
3000	1.7508	35.84	1.8540	39.41	1.8858	40.43
4000	1.7406	35.46	1.8477	39.21	1.8768	40.15
5000	1.7356	35.28	1.8413	38.99	1.8767	40.15
6000	1.7204	34.71	1.8223	38.36	1.8750	40.09
7000	1.7180	34.62	1.8096	37.93	1.8681	39.87
8000	1.7153	34.51	1.7905	37.26	1.8593	39.58

Table 3.4 Fracture width and porosity of resin-coated sand proppant at the concentration of 0.2 lb/ft^2.

Mesh-Size	20/40		40/70	
Closure Stress (psia)	W_f (mm)	ϕ_p (%)	W_f (mm)	ϕ_p (%)
0	0.6800	44.09	0.7100	44.09
1000	0.6627	42.63	0.6910	42.56
2000	0.6450	41.06	0.6636	40.19
3000	0.6166	38.34	0.6540	39.31
4000	0.5763	34.03	0.6400	37.98
5000	0.5705	33.36	0.6033	34.21
6000	0.5647	32.68	0.5986	33.69
7000	0.5359	29.06	0.5615	29.31
8000	0.5040	24.57	0.5522	28.12

Table 3.5 Fracture width and porosity of resin-coated sand proppant at the concentration of 0.4 lb/ft^2.

Mesh-Size	20/40		40/70	
Closure Stress (psia)	W_f (mm)	ϕ_p (%)	W_f (mm)	ϕ_p (%)
0	1.3500	43.68	1.4100	43.70
1000	1.3252	42.62	1.3400	40.76
2000	1.3000	41.51	1.2776	37.87
3000	1.2261	37.99	1.2542	36.71
4000	1.1889	36.05	1.2150	34.67
5000	1.1020	31.00	1.1841	32.96
6000	1.0899	30.24	1.1763	32.52
7000	1.0899	30.24	1.1685	32.07
8000	1.0775	29.43	1.1530	31.15

Table 3.6 Fracture width and porosity of resin-coated sand proppant at the concentration of 0.6 lb/ft^2.

Mesh-Size	20/40		40/70	
Closure Stress (psia)	**W_f (mm)**	**ϕ_p (%)**	**W_f (mm)**	**ϕ_p (%)**
0	2.0300	43.82	2.1200	43.84
1000	1.9393	41.19	2.0290	41.32
2000	1.9064	40.17	2.0000	40.47
3000	1.8982	39.92	1.9470	38.84
4000	1.8735	39.12	1.9171	37.89
5000	1.8078	36.91	1.9020	37.39
6000	1.7913	36.33	1.8870	36.90
7000	1.7747	35.73	1.8795	36.65
8000	1.7667	35.44	1.8644	36.14

Table 3.7 Fracture width and porosity of ceramic proppant at the concentration of 0.2 lb/ft^2.

Mesh-Size	20/40		40/70	
Closure Stress (psia)	W_f (mm)	ϕ_p (%)	W_f (mm)	ϕ_p (%)
0	0.7300	62.45	0.4820	43.29
1000	0.7086	62.45	0.4760	42.57
2000	0.7030	62.45	0.4710	41.96
3000	0.6553	62.45	0.4540	39.79
4000	0.6447	62.45	0.4326	36.81
5000	0.5861	62.45	0.4270	35.98
6000	0.5807	62.45	0.4220	35.23
7000	0.5594	62.45	0.4216	35.16
8000	0.5168	62.45	0.4162	34.32

Table 3.8 Fracture width and porosity of ceramic proppant at the concentration of 0.4 lb/ft^2.

Mesh-Size	**20/40**		**40/70**	
Closure Stress (psia)	**W_f (mm)**	**ϕ_p (%)**	**W_f (mm)**	**ϕ_p (%)**
0	0.9400	41.68	0.9600	43.05
1000	0.9240	40.67	0.9520	42.57
2000	0.9160	40.15	0.9430	42.03
3000	0.8841	37.99	0.9346	41.51
4000	0.8760	37.42	0.9270	41.03
5000	0.8682	36.86	0.9100	39.92
6000	0.8602	36.27	0.9015	39.36
7000	0.8520	35.66	0.8850	38.23
8000	0.8443	35.07	0.8680	37.02

Table 3.9 Fracture width and porosity of ceramic proppant at the concentration of 0.6 lb/ft^2.

Mesh-Size	20/40		40/70	
Closure Stress (psia)	W_f (mm)	ϕ_p (%)	W_f (mm)	ϕ_p (%)
0	1.4200	42.09	1.4458	43.28
1000	1.3917	40.91	1.4047	41.62
2000	1.3775	40.30	1.3910	41.05
3000	1.3350	38.40	1.3704	40.16
4000	1.3349	38.39	1.3704	40.16
5000	1.3207	37.74	1.3636	39.86
6000	1.3140	37.42	1.3636	39.86
7000	1.3060	37.04	1.3636	39.86
8000	1.2990	36.69	1.3636	39.86

The calculated values of the proppant porosity (ϕ_p) at different stress conditions, is not only useful for the proppant evaluation process, but it is also a main parameter used in the well production and reservoir simulation models. It is essential in the calculation of the bulk volume of the propped fracture for a given injected proppant mass. The fracture volume is used in the unified fracture design (UFD) provided by Economides et al. (2002) to optimize the fracture dimensions and maximize the well productivity. The design of the fracturing treatments also employs the proppant porosity to convert the hydraulic fracture width (which is calculated using the fracture geometry

models, such as the PKN and KGD models) into the propped fracture width. The match of the design fracture geometry with the optimum values from the production models is required to achieve the maximum possible benefits from the fracture treatment (Economides et al. 2002). Furthermore, the proppant porosity can be utilized to estimate the fracture permeability using the porosity/permeability models, e.g. the Kozeny-Carman equation (Fan et al. 2017, Barree et al. 2016, Shamsi et al. 2015).

3.2. Evaluation of Crushed Proppant

The recovered proppant after each test was analyzed to quantify the proppant crushing mechanism using a sieve shaker. The proppant that falls below the original proppant size is considered as the crushed proppant. The crushed proppant is weighted and calculated as a percentage of the total proppant mass. **Figure 3.1** shows the results of sand proppant crushing at 0.2, 0.4, and 0.6 lb/ft^2. The results showed that the crushed percentage of the 20/40-mesh sand can be as high as 28.03 wt% at 0.2 lb/ft^2.

The results also showed that, for the same concentration, the smaller-size proppant experiences less crushing under stress than the larger-size proppant. This is because, for the same mass, the number of proppant particles is higher in the case of the small-size proppant than in the case of the large-size proppant. Therefore, the applied stress is distributed on more proppant particles, and consequently, each proppant particle experiences less stress in the case of small-size proppant than in the case of the large-size proppant.

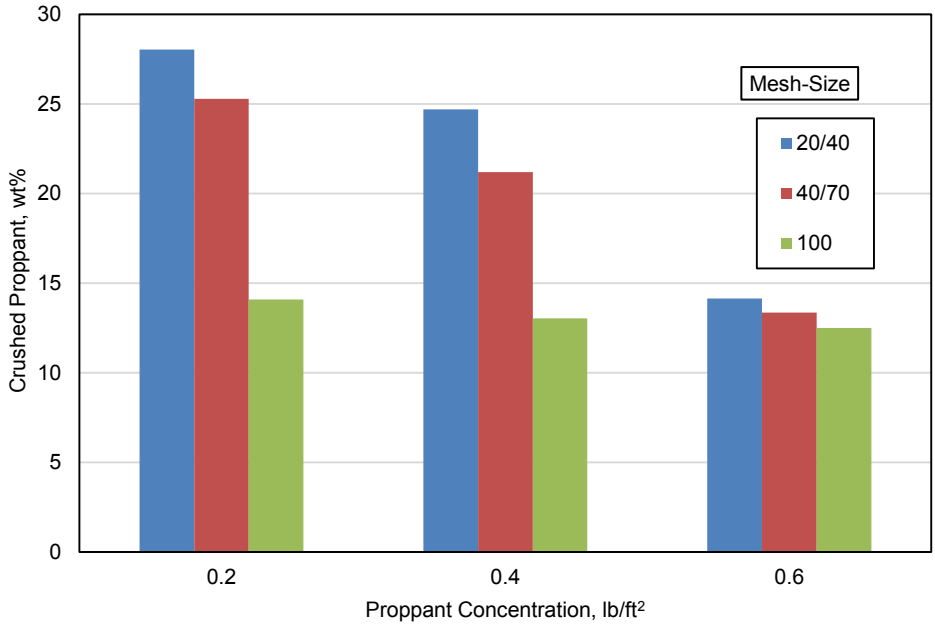

Figure 3.1 Percentage of crushed sand of different sizes and concentrations. Reprinted from SPE-191240-MS.

Figure 3.1 also indicated that for the same proppant size, as the concentration increases, the proppant crushing decreases. The proppant particles in contact with the rock surface are subjected to more stress than the interior particle due to the reduced number of contact points with the adjacent particles. As a result, the particles in contact with the rock surface experience more crushing than the interior particles (Palisch et al. 2010). Therefore, as the proppant concentration increases, the percentage of the particles in contact with the rock decreases, thus, the crushing test results in a lower percentage. The testing of the resin-coated sand under stress resulted in the bonding of the proppant particles in a large agglomerates, as shown in **Figure 3.2**, which prevented the falling of the crushed proppants in the post-test sieve analysis. The resin encapsulates any crushed

proppants and prevents its migration and plugging to the pore throats inside the fracture. In addition, it consolidates the uncrushed proppant particles to prevent the proppant flow-back process.

Figure 3.2 Large agglomerates of resin-coated sand proppant after testing under stress.

Due to the high-strength of ceramic proppant, no crushing has been observed after its testing. Therefore, the reduction of the fracture width and the proppant porosity, in the case of ceramic proppant, results only from the proppant compaction and embedment mechanisms.

Figures 3.3 and 3.4 show a comparison between the proppant porosity at 8,000 psia for sand and resin-coated sand proppants, respectively. The results showed that the proppant porosity is directly proportional to the proppant concentration and inversely proportional to the proppant size. Such relations is explained by the inverse relation between the proppant porosity and the proppant crushing mechanism which is controlled by the proppant size and concentration as shown in **Figure 3.1**.

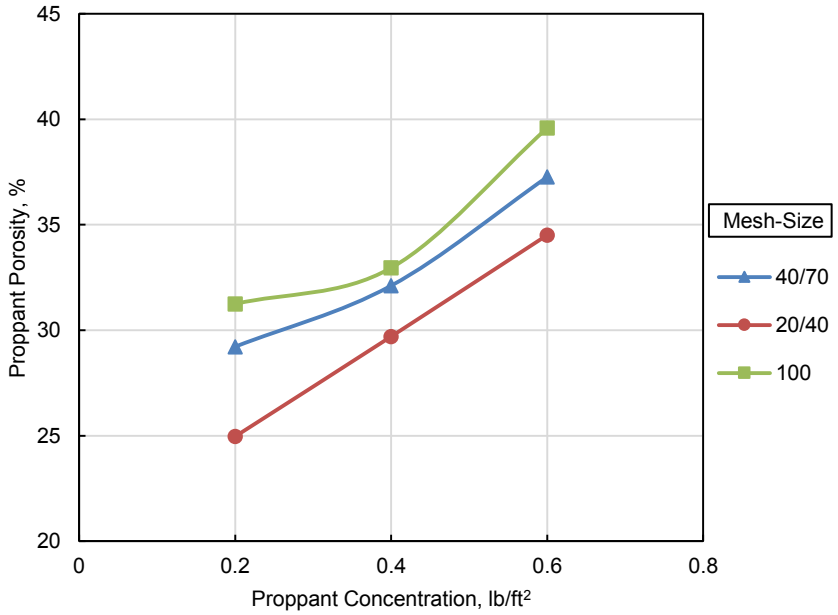

Figure 3.3 Sand porosity at different concentrations and mesh-sizes at 8,000 psia.

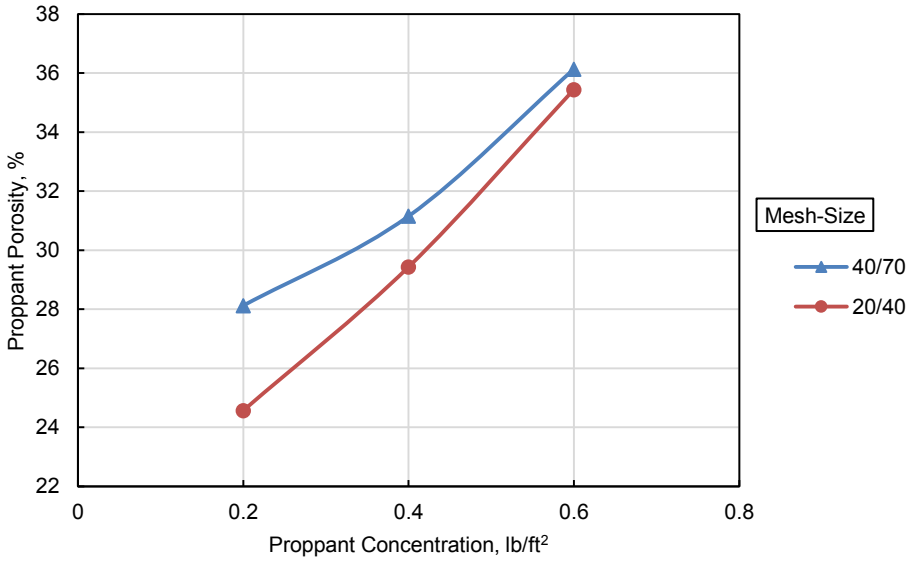

Figure 3.4 Porosity of Resin-coated sand at different concentrations and mesh-sizes at 8,000 psia.

In the preparation of the fracture model of 20/40 ceramic proppant at 0.2 lb/ft^2, a physical constraint existed that the fracture width should be equal or greater than the particle diameter, so that the proppant can enter the fracture. The initial fracture width was set to 0.73 mm (the mean proppant particle diameter) which is equivalent to an initial porosity of 62.76%. Due to the increased density of ceramic (>3.6 g/cc), the 20/40 ceramic proppant at 0.2 lb/ft^2 partially covered the available fracture area, and thus, it formed a partial monolayer of proppant with an enlarged porosity value. At such condition, the reduction of fracture width due to stress results only from proppant embedment into the rock surface and no compaction or crushing mechanisms involved. **Table 3.10** shows the embedment distance of 20/40 ceramic proppant in Eagle Ford shale at 0.2 lb/ft^2 under the effect of stress. The results show that the reduction percentage of the fracture width due to embedment can reach 29.2% at 8,000 psia, which could be of a significant effect to the fracture conductivity when coupled with the damage from fracture fluid residues and multiphase flow.

Table 3.10 Embedment of 20/40 ceramic proppant in Eagle Ford shale at 0.2 lb/ft^2.

Closure Stress (psia)	W_f (mm)	Embedment (mm)	Reduction of fracture width (%)
0	0.7300	0.0000	0
1000	0.7086	0.0214	2.9315068
2000	0.7030	0.0270	3.6986301
3000	0.6553	0.0747	10.232877
4000	0.6447	0.0853	11.684932
5000	0.5861	0.1439	19.712329
6000	0.5807	0.1493	20.452055
7000	0.5594	0.1706	23.369863
8000	0.5168	0.2132	29.205479

Although the 20/40 sand and the 20/40 ceramic have the same mesh size, the 20/40 sand at 0.2 lb/ft^2 was packed in a smaller fracture width of 0.64 mm compared to 0.73 mm in the case of ceramic. This is because the mean particle diameter of the 20/40 sand is less than the 20/40 ceramic (0.54 mm compared to 0.73 mm), and also the roundness and sphericity of particles are less in the case of sand, as shown in **Table 2.2**, which enables the particles to get packed in a smaller volume.

Figure 3.5 shows the proppant porosity of 20/40 and 40/70 ceramic proppants at 8,000 psia. At 0.2 lb/ft^2, the 20/40 proppant showed an elevated porosity as it formed a fracture with a partial monolayer of proppant. At 0.4 and 0.6 lb/ft^2, the results show that the porosity slightly increases as the proppant size decreases and proppant concentration

increases. Since the ceramic proppant experiences no crushing due to its increased strength, the only mechanism controls the porosity in that case is the proppant compaction due to stress. The compaction of particles under stress is controlled by the stability of frictional and cohesive forces operating at the contact points between particles (Kadau et al. 2010). As the frictional and cohesive forces increases, the resistance force of particles to movement increases, and as a result, the compaction of particles decreases. Such forces is higher in small size particles because the external surface area of particles exposed to the load is higher than in the case of large particles. Therefore, the compaction of larger size proppant is higher than smaller size proppant. The slight increase in the proppant porosity at 0.6 lb/ft^2 can be explained by the increased number of proppant particles which reduces the load on each proppant particle and reduces its possibility to compact under stress.

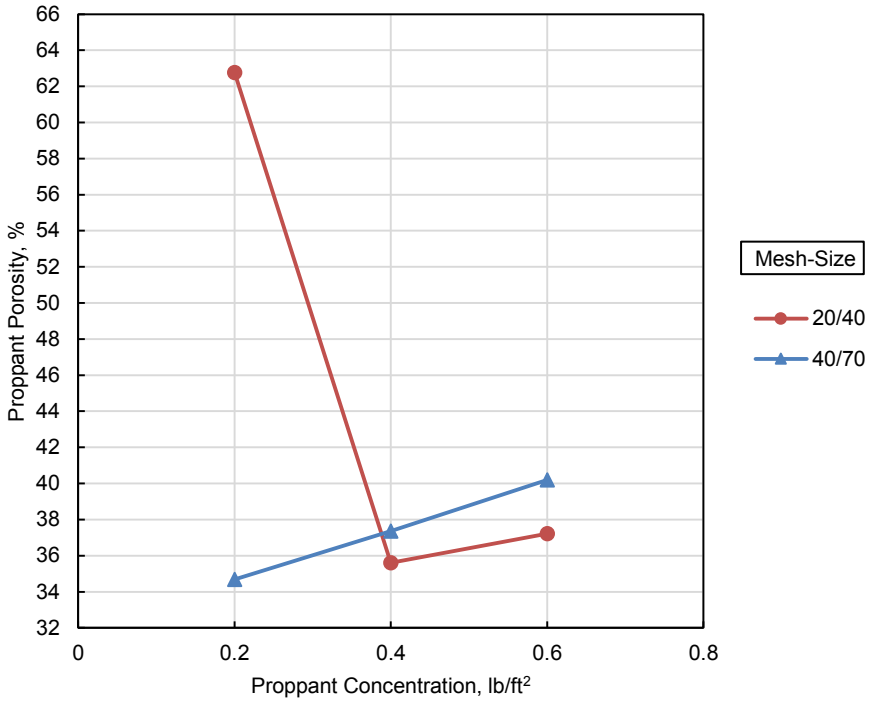

Figure 3.5 Porosity of ceramic proppant at different concentrations and mesh-sizes at 8,000 psia.

Figures 3.6 and 3.7 show the reduction percentage of proppant porosity and fracture width, respectively, at 8,000 psia of 20/40 and 40/70 proppants. The maximum reduction of proppant porosity and fracture width were found be 44.16 and 25.88%, respectively, corresponding to 20/40 resin-coated sand at 0.2 lb/ft^2. The resin-coated sand experienced the most damage due to its reduced density (2.61 g/cc) which reduces its strength and resistance to crushing and compaction. The proppant is coated with 0-5 wt% of phenol formaldehyde resin which reduced its density than the regular sand density (2.65 g/cc). On the contrary, the 40/70 ceramic proppant which has the highest density (3.63 g/cc), and consequently the highest strength, showed the minimum

reduction in proppant porosity and fracture width of the value of 7.88 and 5.68%, respectively.

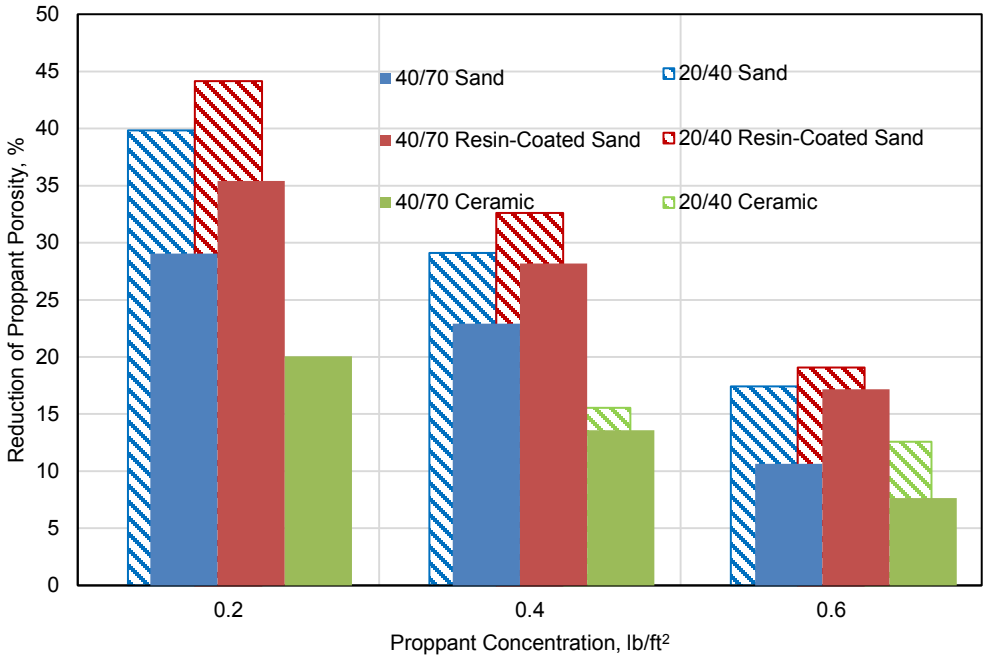

Figure 3.6 Reduction percentage of proppant porosity at 8,000 psia for different types, concentrations, and mesh-sizes.

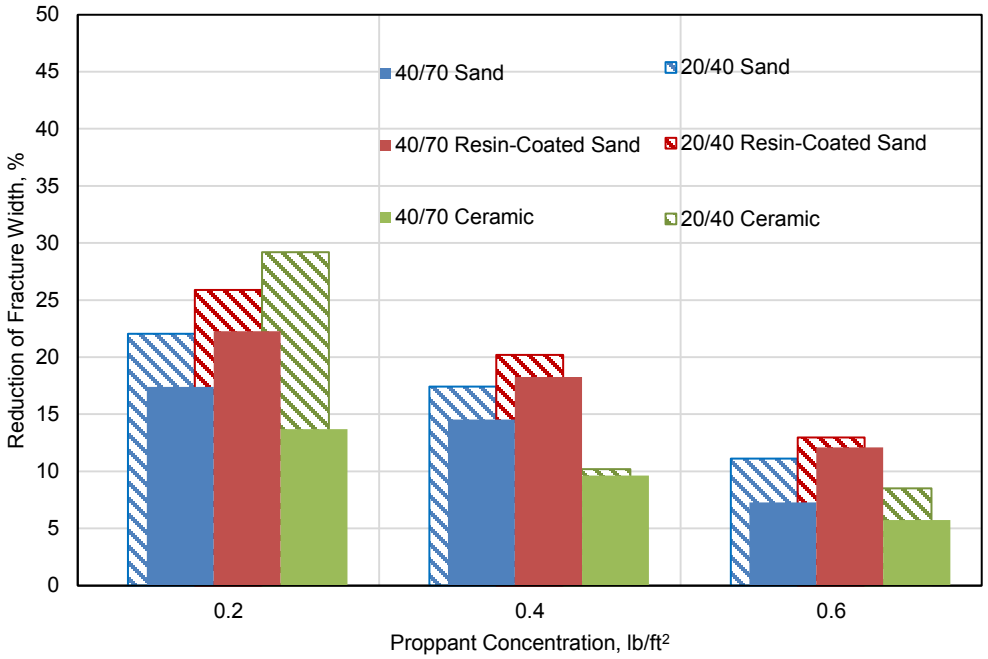

Figure 3.7 Reduction percentage of fracture width at 8,000 psia for different types, concentrations, and mesh-sizes.

The following sections present the results from the proppant diagenesis study of ceramic, sand, and resin-coated sand proppants.

3.3. Diagenesis of Ceramic Proppant

3.3.1. SEM/EDS Analysis

The visual observation of the ceramic proppant and formation mixture after aging showed the agglomeration of both materials in the form of large clumps. **Figure 3.8** shows the observed formation and proppant clumps. The SEM examination indicated the presence of clustered broken thin-cuboid-like crystals on and around most of the proppant and formation particles as shown in **Figures 3.9 through 3.12**. The EDS

analysis was utilized to determine the composition of the observed crystals. The results as shown in **Table 3.11** identify the crystals as $CaSO_4$.

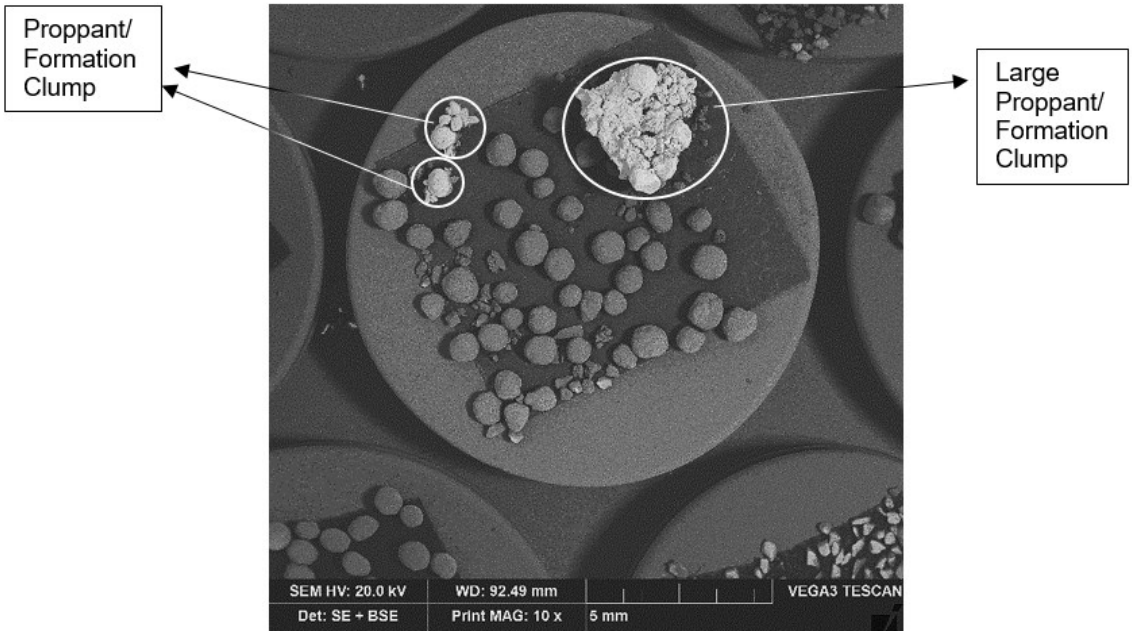

Figure 3.8 Clumps of the proppant and formation chips formed after aging the ceramic proppant/formation mixture. Reprinted from SPE-191225-MS.

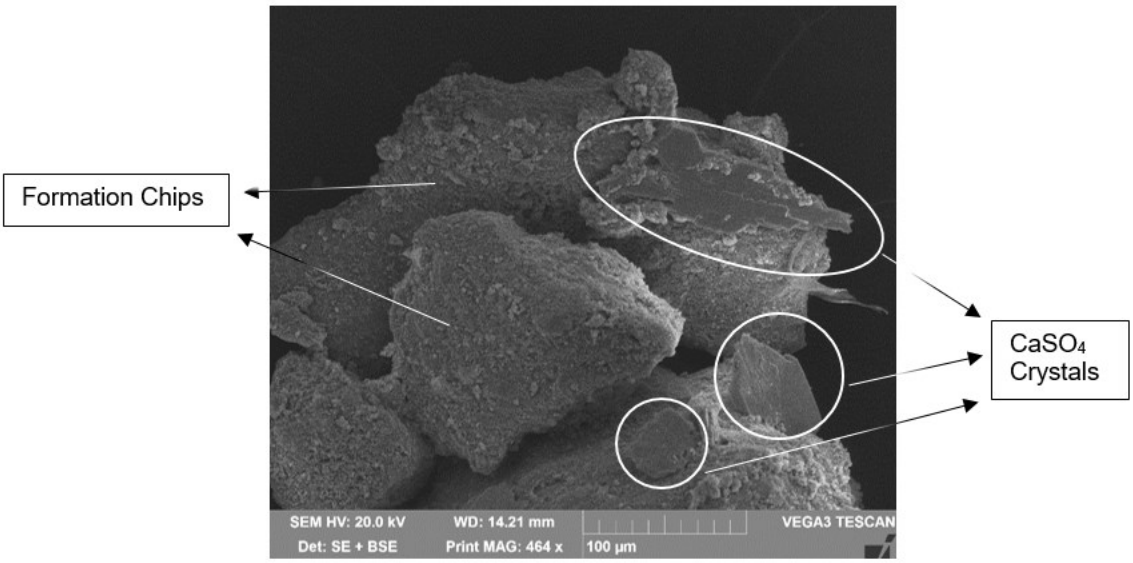

Figure 3.9 $CaSO_4$ crystals formed on the formation surface after aging the ceramic proppant/formation mixture. Reprinted from SPE-191225-MS.

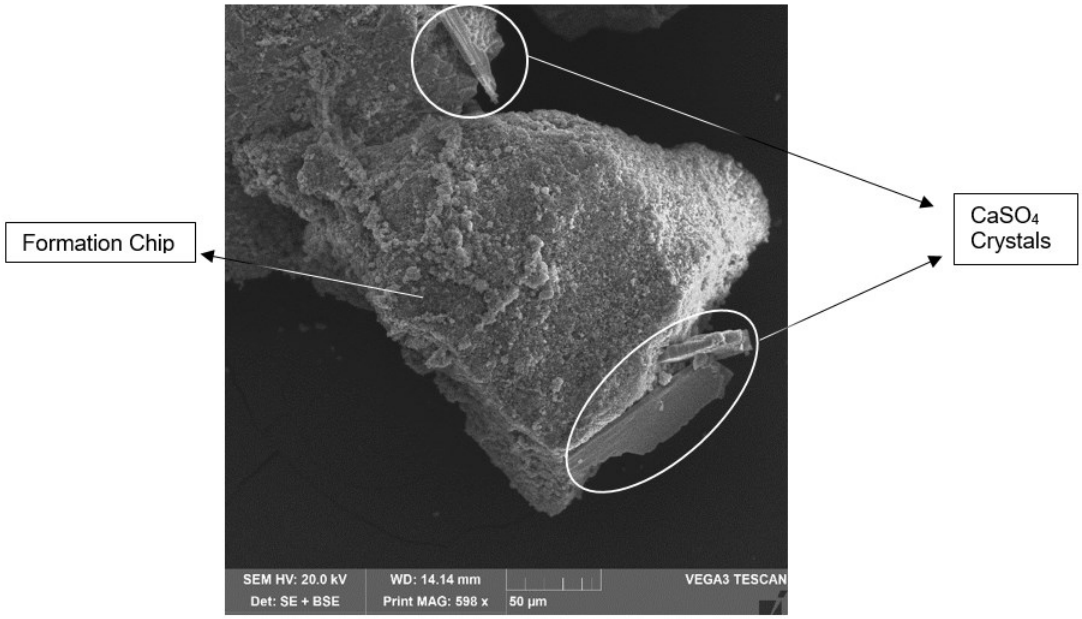

Figure 3.10 $CaSO_4$ crystals formed around the formation chips after aging the ceramic proppant/formation mixture. Reprinted from SPE-191225-MS.

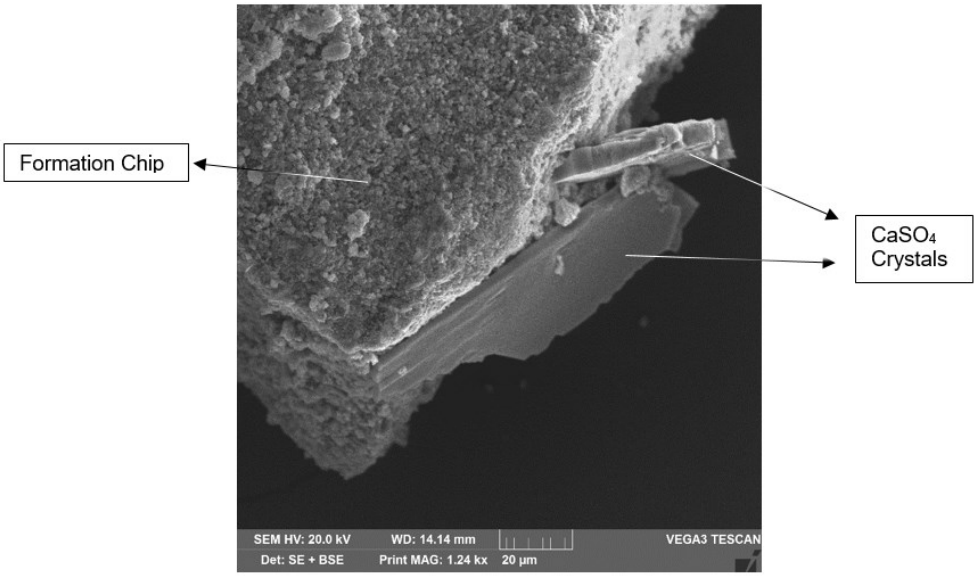

Figure 3.11 $CaSO_4$ crystals formed around the formation chips after aging the ceramic proppant/formation mixture at 1.24 kx magnification. Reprinted from SPE-191225-MS.

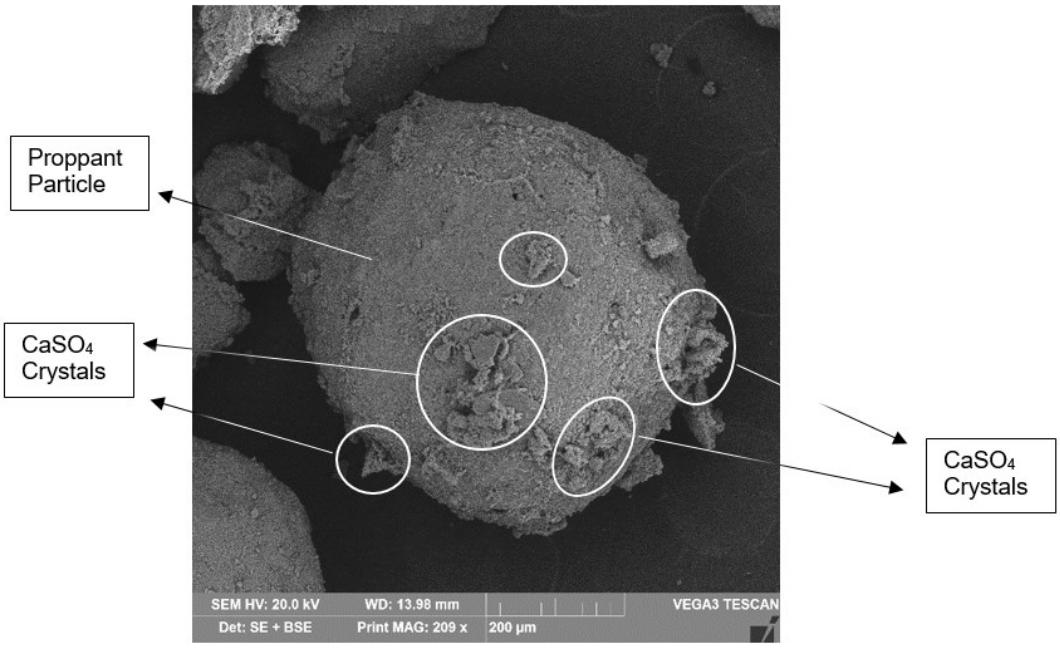

Figure 3.12 $CaSO_4$ crystals formed on and around the proppant particles after aging the ceramic proppant/formation mixture. Reprinted from SPE-191225-MS.

Table 3.11 The EDS analysis of the observed $CaSO_4$ crystals, after excluding the oxygen element. Reprinted from SPE-191225-MS.

Element	Concentration, wt%
Ca	59.04
S	40.96

Some $CaSO_4$ crystals were found embedded-in or covered-with a second precipitated material on the proppant and formation surfaces, as shown in **Figures 3.13 through 3.20** at different magnifications. It consists of tiny fines (less than 1 Mm) that were found in both loose and bonded forms. It was also found extensively on some proppant and formation surfaces and in the area of attachment between the proppant and the formation, as shown in **Figures 3.21 through 3.28**. The EDS results, as shown in **Table 3.12**, indicates its richness in calcium and aluminum with less silicon content. Based on the previous studies (Weaver et al. 2005; LaFallotte and Carman 2010; Raysoni et al. 2013), which have been done at similar aging conditions, the precipitate was interpreted as a calcium zeolite mineral. The proppant is characterized by the abundance of the aluminum and iron elements, while the formation is characterized by its richness in calcium and silicon elements. The different Al/Si ratios, as shown in **Table 3.12**, is an indicator of the development of a new material.

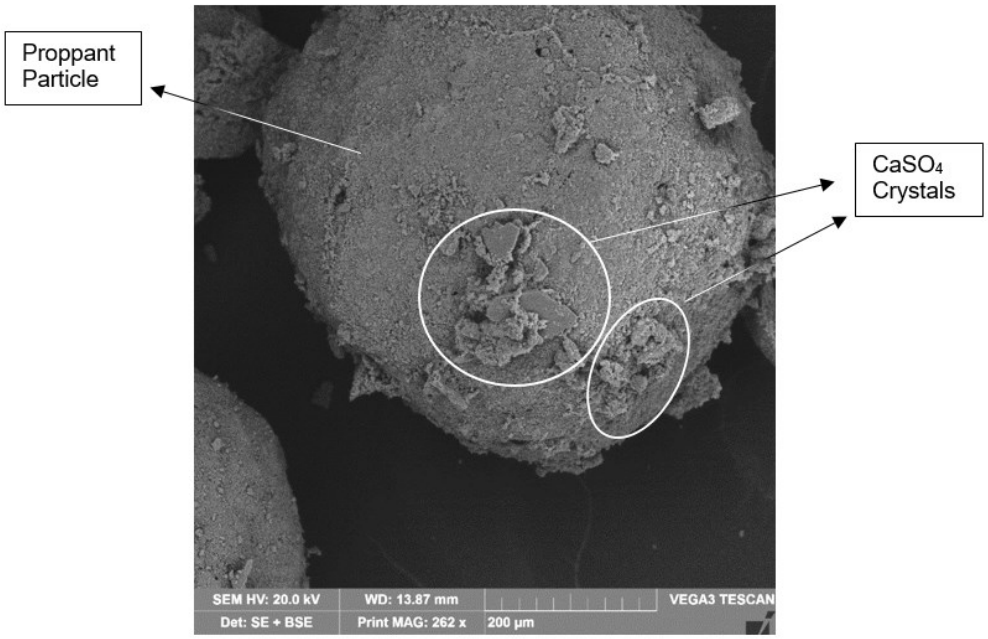

Figure 3.13 $CaSO_4$ crystals clumped with calcium zeolite on the surface of the ceramic proppant. Reprinted from SPE-191225-MS.

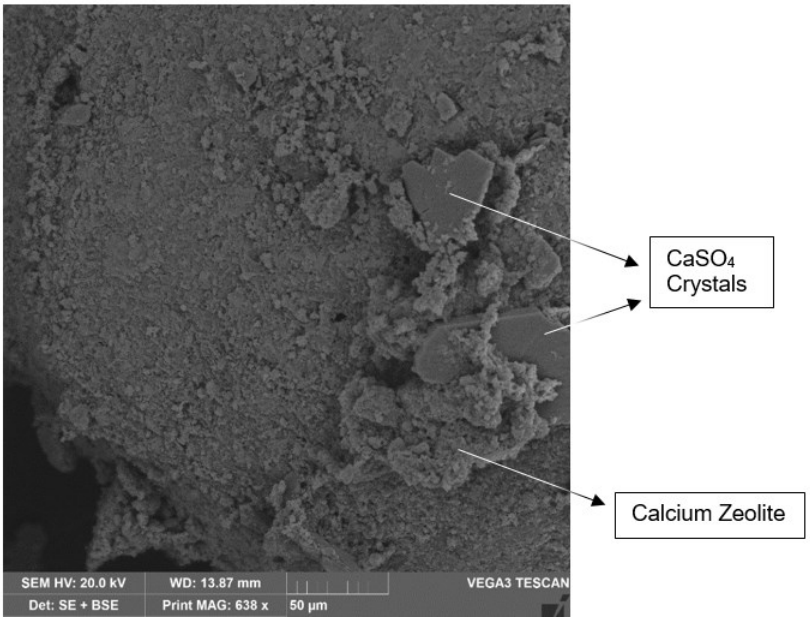

Figure 3.14 $CaSO_4$ crystals clumped with calcium zeolite on the surface of the ceramic proppant at 638 kx magnification. Reprinted from SPE-191225-MS.

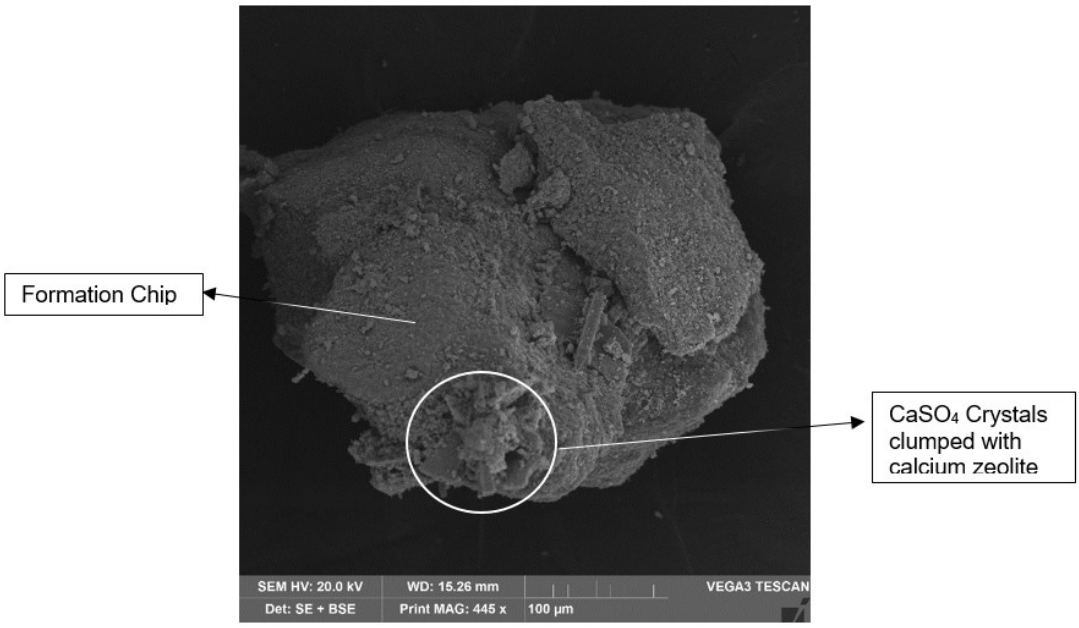

Figure 3.15 $CaSO_4$ crystals clumped with calcium zeolite on the surface of formation chips. Reprinted from SPE-191225-MS.

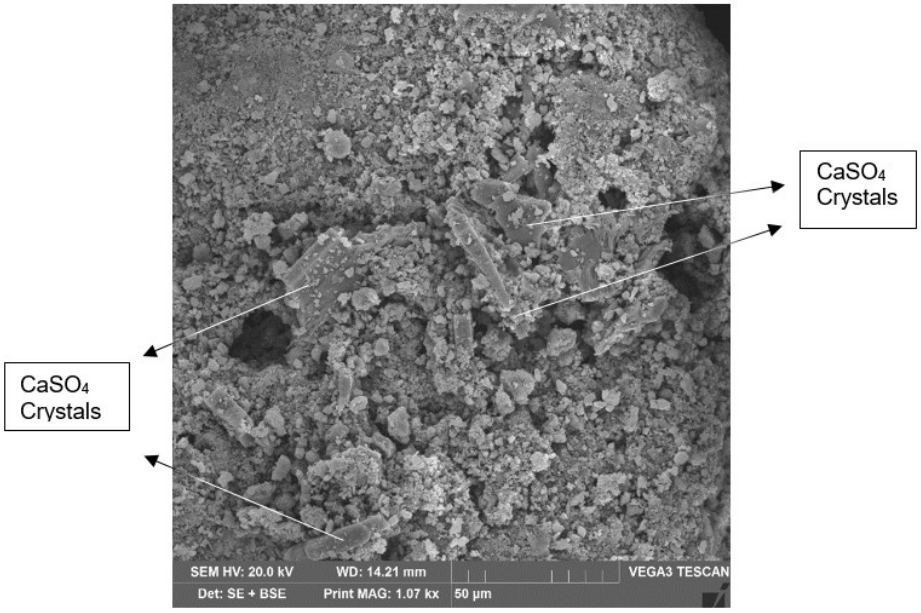

Figure 3.16 $CaSO_4$ crystals covered with calcium zeolite on the surface of the formation. Reprinted from SPE-191225-MS.

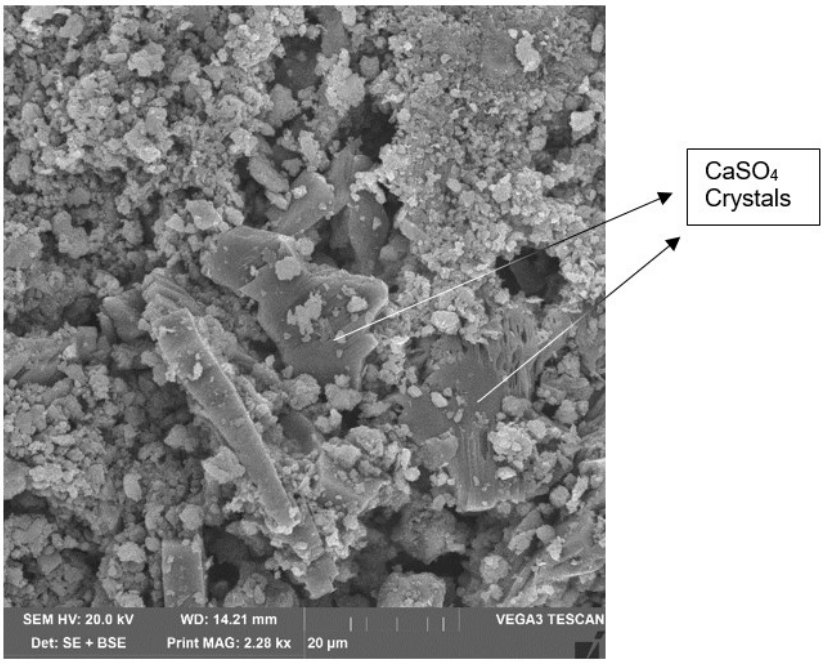

Figure 3.17 $CaSO_4$ crystals covered with calcium zeolite on the surface of the formation at 2.28 kx magnification. Reprinted from SPE-191225-MS.

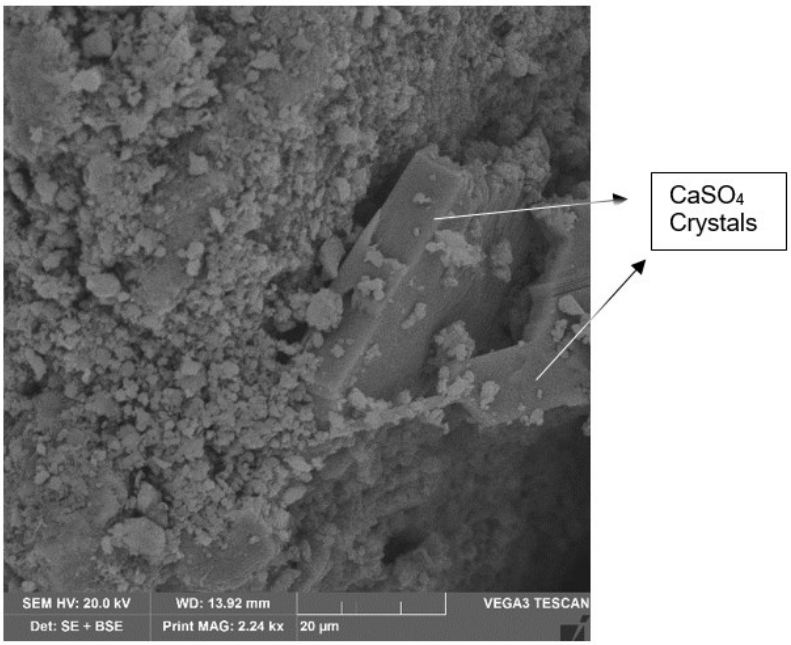

Figure 3.18 $CaSO_4$ crystals covered with calcium zeolite on the surface of the ceramic proppant. Reprinted from SPE-191225-MS.

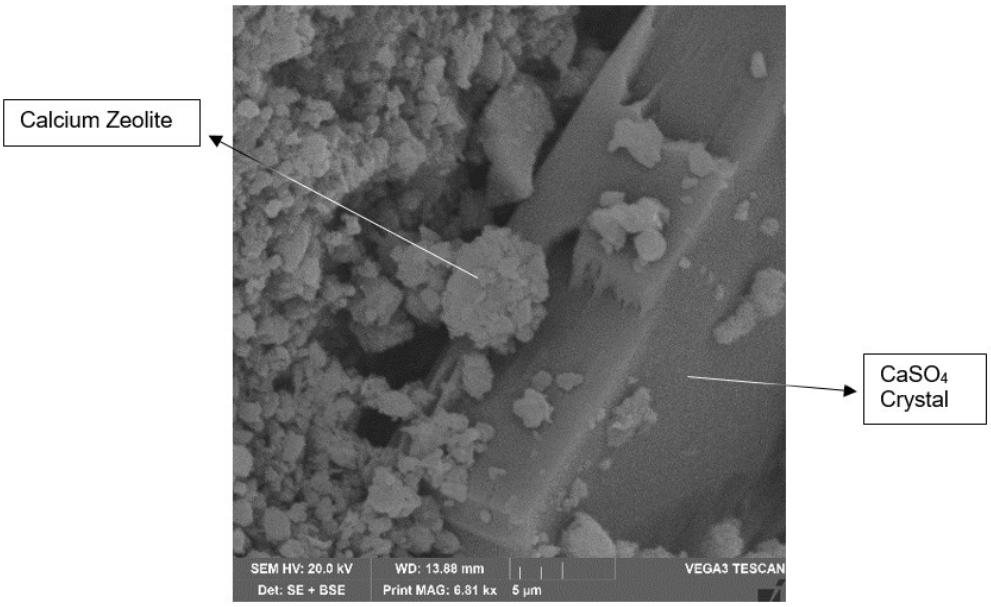

Figure 3.19 $CaSO_4$ crystal covered with calcium zeolite on the surface of the ceramic proppant at 6.81 kx magnification. Reprinted from SPE-191225-MS.

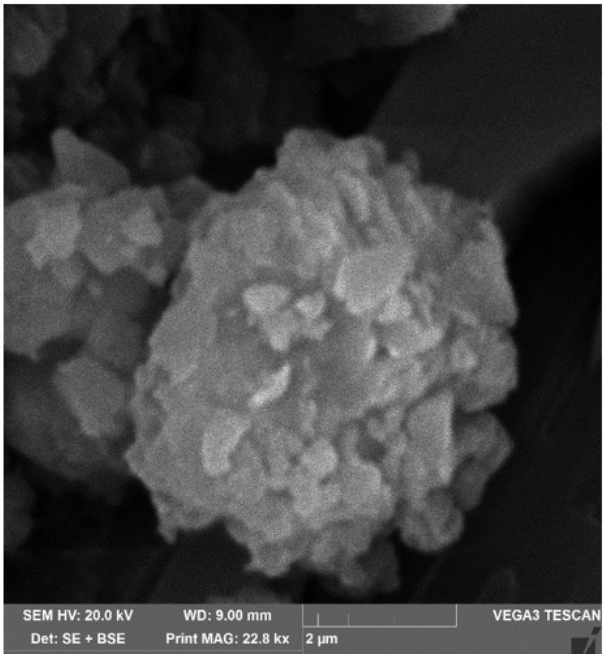

Figure 3.20 Calcium zeolite at 22.8 kx magnification. Reprinted from SPE-191225-MS.

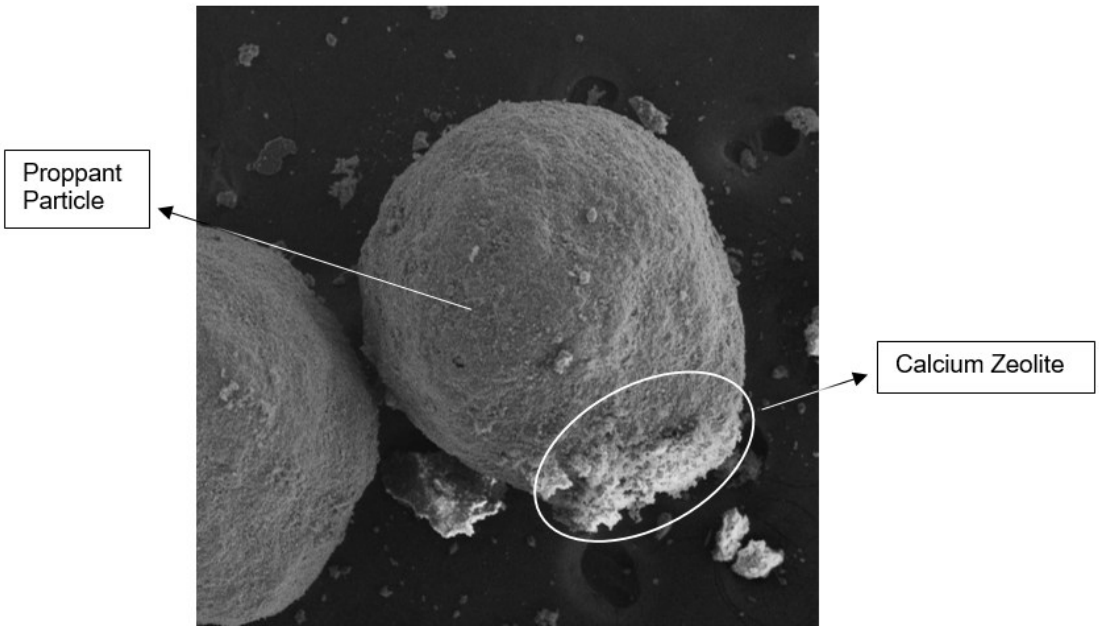

Figure 3.21 Calcium zeolite precipitate on the surface of the ceramic proppant. Reprinted from SPE-191225-MS.

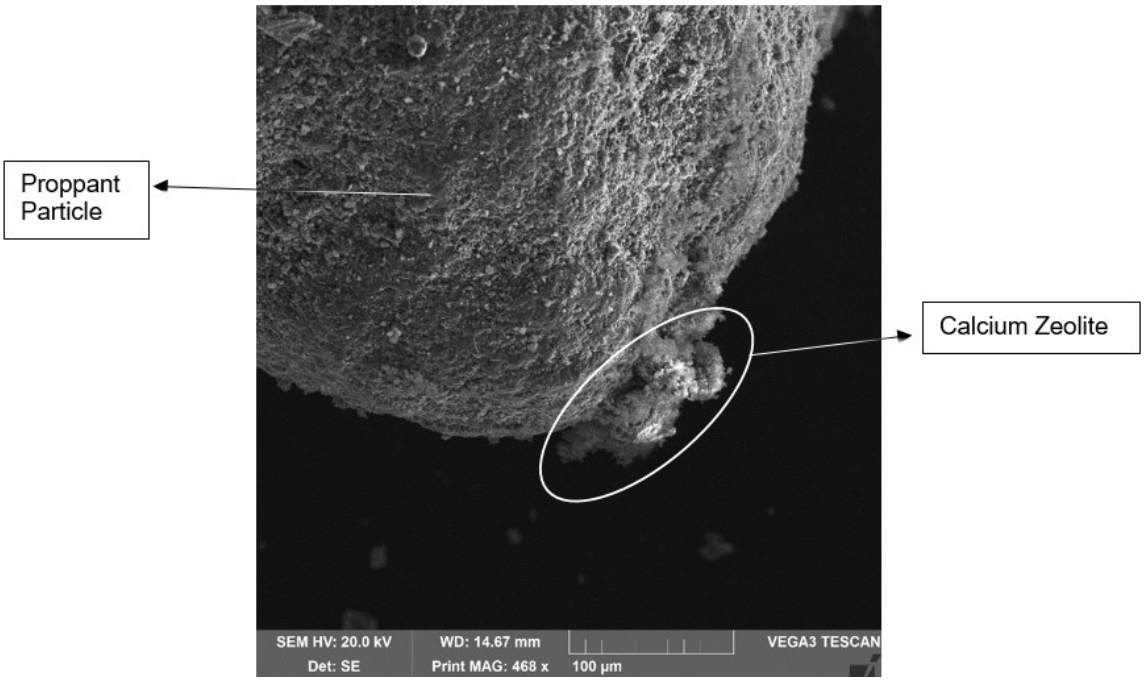

Figure 3.22 Calcium zeolite precipitate on the surface of the ceramic proppant. Reprinted from SPE-191225-MS.

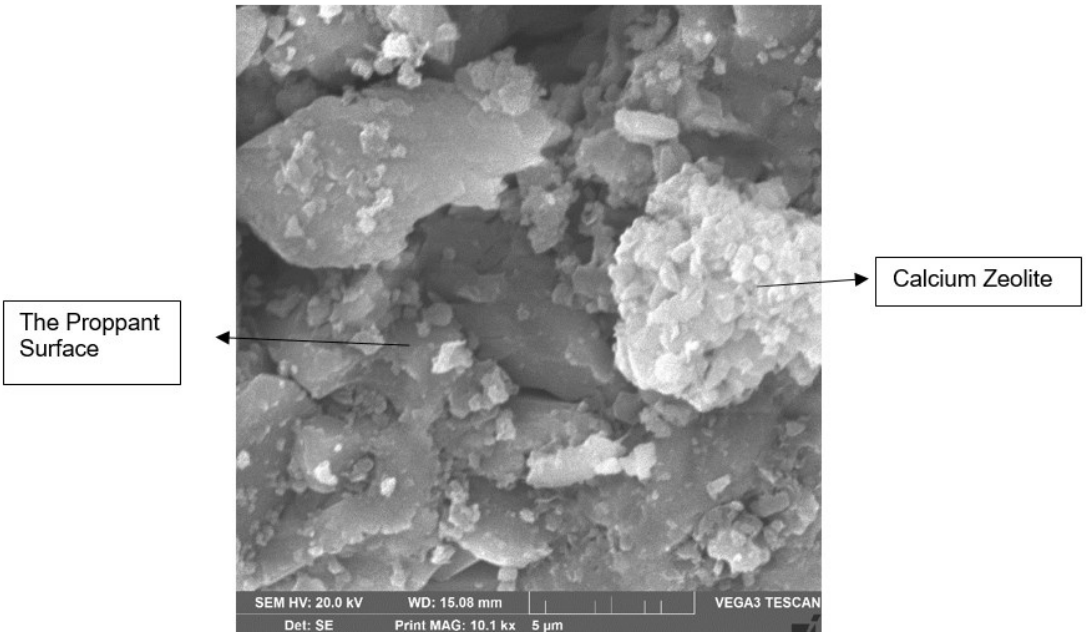

Figure 3.23 Calcium zeolite precipitate on the surface of the ceramic proppant at 10.1 kx magnification. Reprinted from SPE-191225-MS.

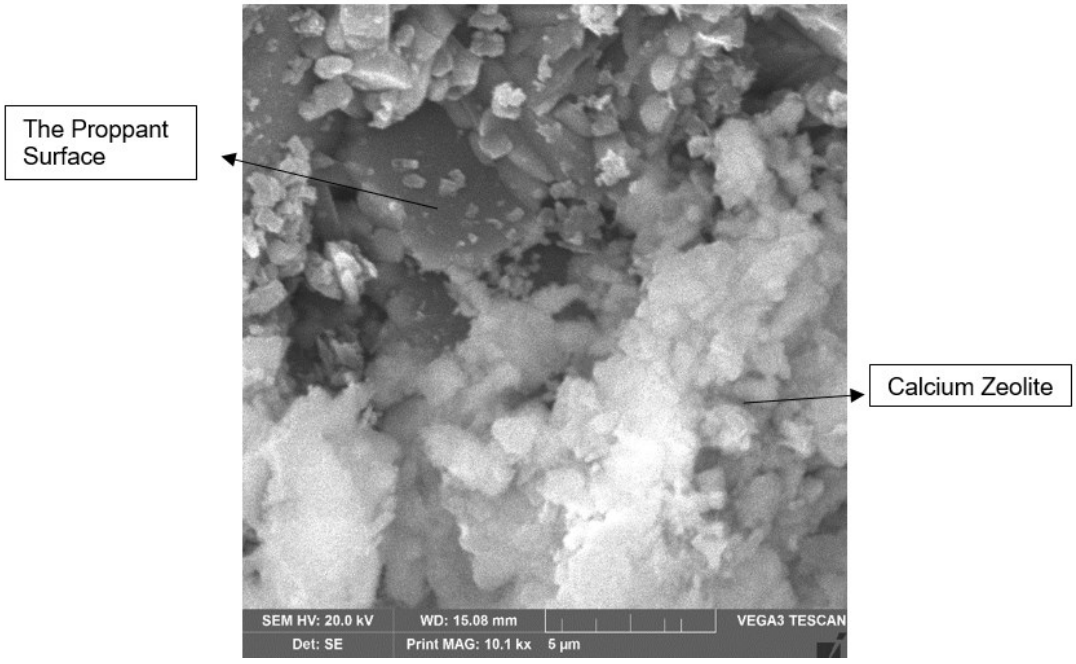

Figure 3.24 Calcium zeolite precipitate on the surface of the ceramic proppant at 15.08 kx magnification. Reprinted from SPE-191225-MS.

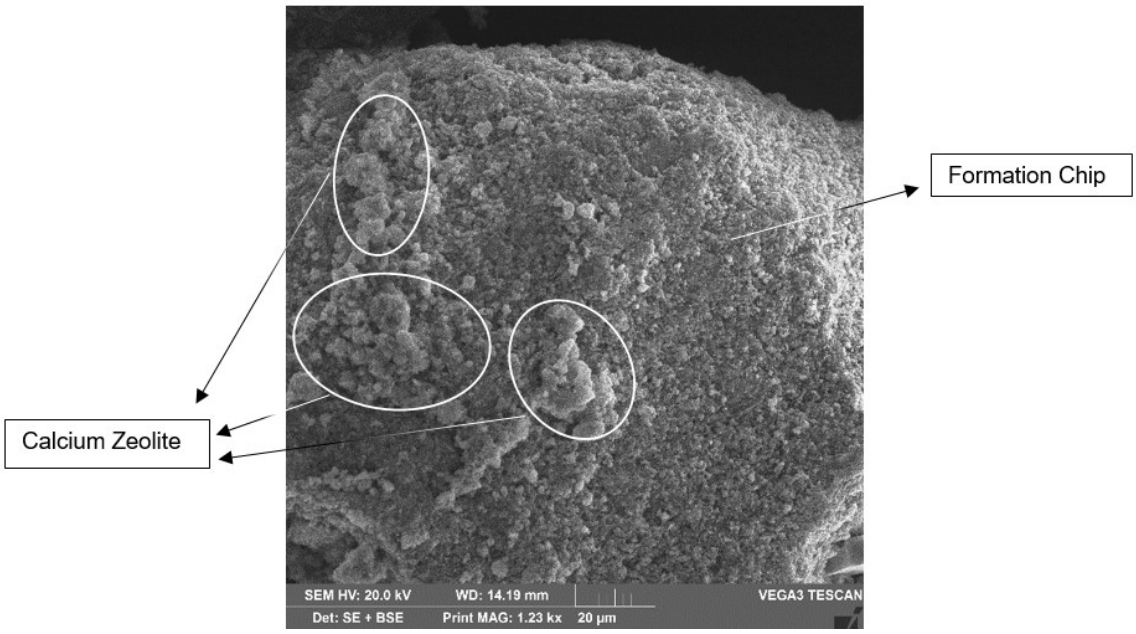

Figure 3.25 Calcium zeolite precipitate on the surface of the formation. Reprinted from SPE-191225-MS.

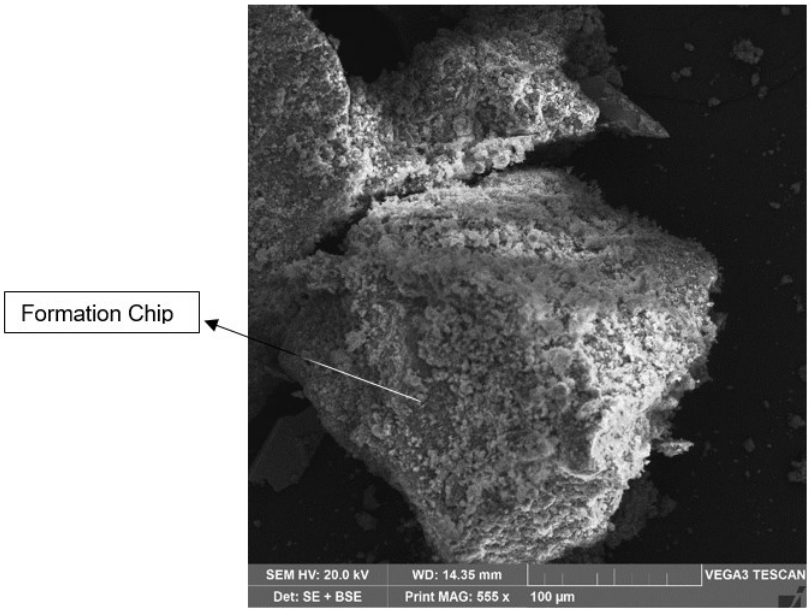

Figure 3.26 Calcium zeolite precipitate covering the surface of a formation chip. Reprinted from SPE-191225-MS.

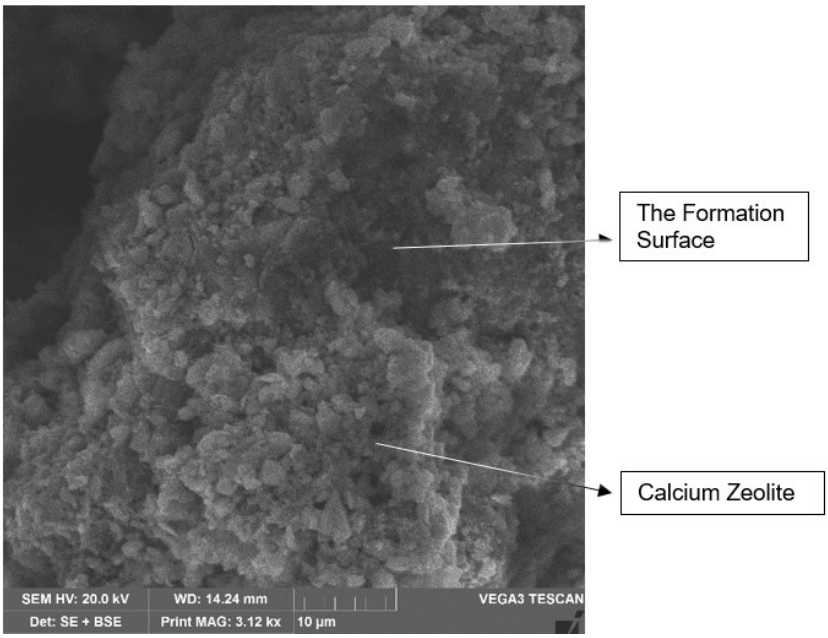

Figure 3.27 Calcium zeolite precipitate on the surface of the formation at 3.12 kx magnification. Reprinted from SPE-191225-MS.

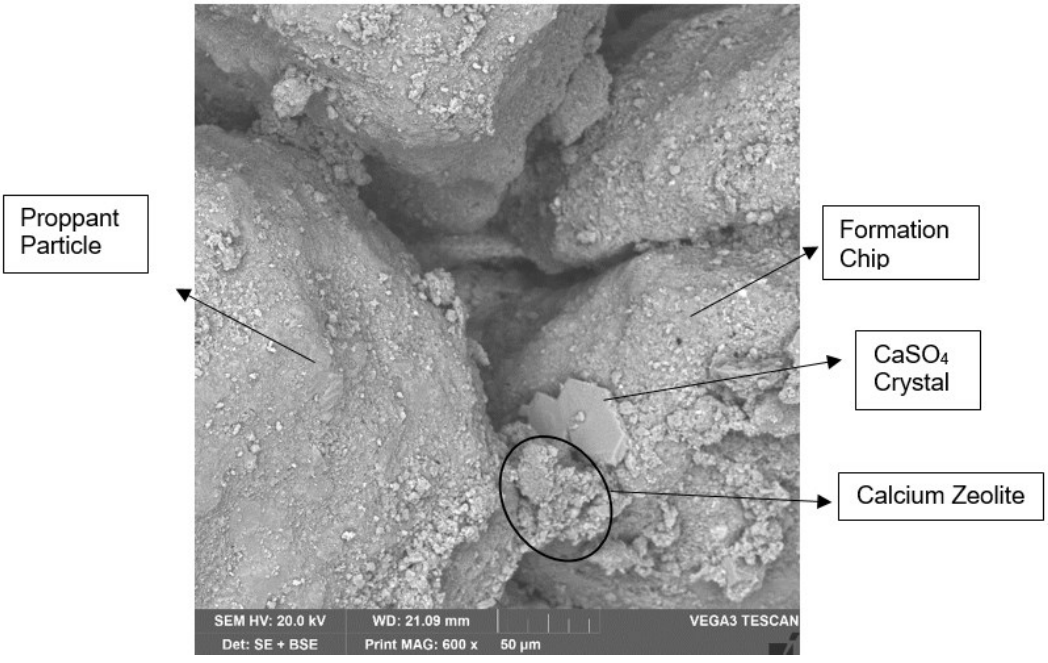

Figure 3.28 Calcium zeolite precipitate on the area between clumped ceramic proppant and formation. Reprinted from SPE-191225-MS.

Table 3.12 The EDS analysis of the formation, the ceramic proppant, and the calcium zeolite precipitate. Reprinted from SPE-191225-MS.

Element, wt%	Ceramic Proppant	Formation	Calcium Zeolite
Ca	Not detected	52.22	75.53
Al	56.89	5.28	16.31
Si	3.39	42.5	8.16
Fe	36.31	Not detected	Not detected
Ti	3.39	Not detected	Not detected
Al/Si ratio	16.78	0.12	1.99

Further investigation using the SEM/EDS analysis indicated the development of a different overgrowth material that were found explicitly on the proppant surface. It was found in the form of tiny fines that are spreading all over the proppant surface (**Figures 3.29 and 3.30**). The EDS analysis shows its chemical composition in **Table 3.13**. It consists of iron, calcium, aluminum, and silicon, in concentrations of 33.05, 29.38, 25.99, and 11.58 wt%, respectively. The overgrowth was interpreted as iron-calcium zeolite. The new overgrowth is differentiated from the proppant by the presence of calcium.

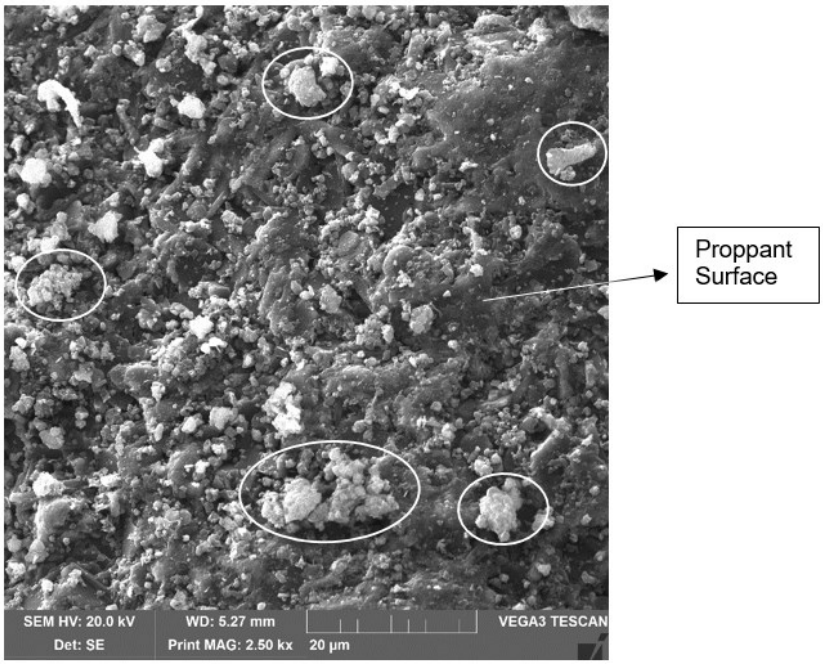

Figure 3.29 Iron-calcium zeolite on the surface of the ceramic proppant. Reprinted from SPE-191225-MS.

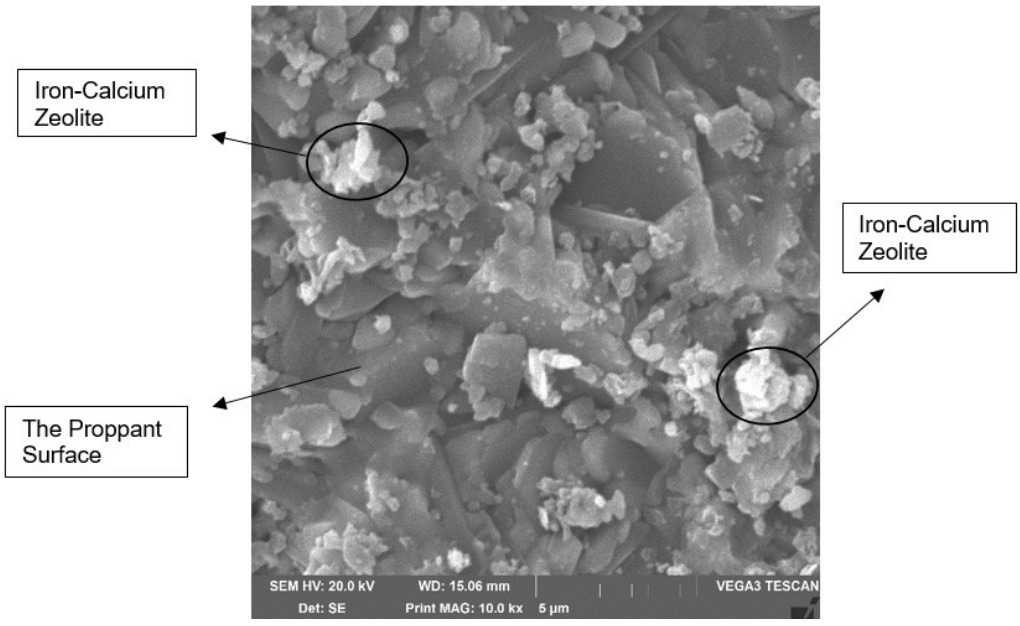

Figure 3.30 Iron-calcium zeolite on the surface of the ceramic proppant at 10.0 kx magnification. Reprinted from SPE-191225-MS.

Table 3.13 The EDS analysis of the observed iron-calcium zeolite overgrowth. Reprinted from SPE-191225-MS.

Element	Concentration, wt%
Fe	33.05
Ca	29.38
Al	25.99
Si	11.58

In order to identify the sources of the observed overgrowth minerals, the ceramic proppant and formation were separately aged under the same conditions. The SEM analysis of the proppant after aging alone indicated the precipitation of a thin layer of a net-like structure on its surface. **Figures 3.31 and 3.32** show the SEM images of the proppant surface before aging, while **Figures 3.33 through 3.35** show the SEM images after aging at different magnifications. The EDS analysis, **Table 3.14**, shows the increase in the silicon content of the proppant surface, which indicates the dissolution of silicon and its subsequent precipitation on the proppant surface. A thorough SEM/EDS investigation showed no observations of any crystalized minerals or any other developed overgrowth material. The aging of the formation alone reproduced the previously observed $CaSO_4$ crystals and the calcium zeolite precipitate. **Figures 3.36 through 3.39** show the observed precipitate materials on the formation surface after aging.

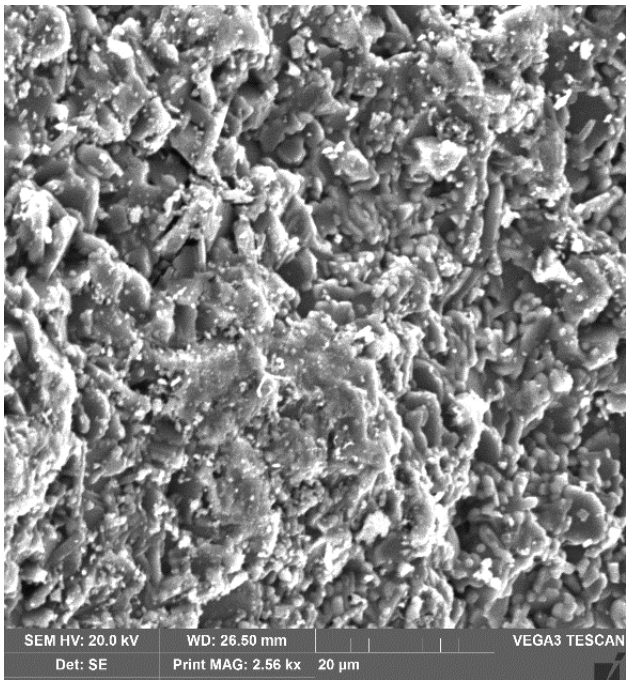

Figure 3.31 The surface of the ceramic proppant before aging at 2.56 kx magnification. Reprinted from SPE-191225-MS.

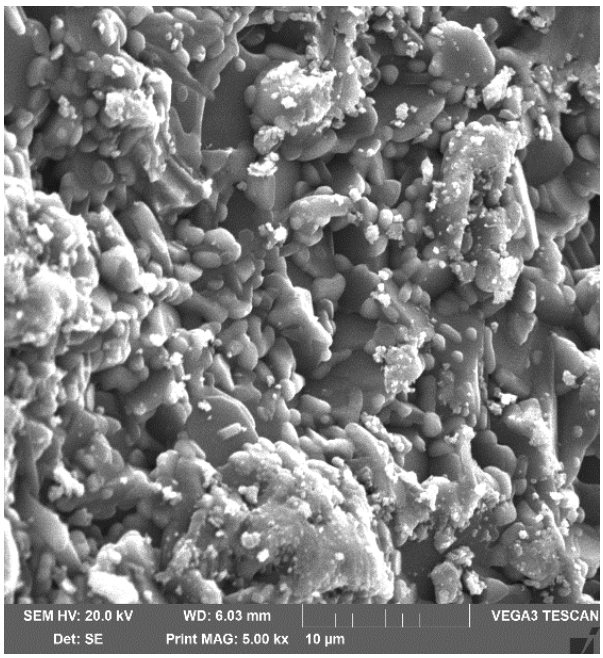

Figure 3.32 The surface of the ceramic proppant before aging at 5.0 kx magnification. Reprinted from SPE-191225-MS.

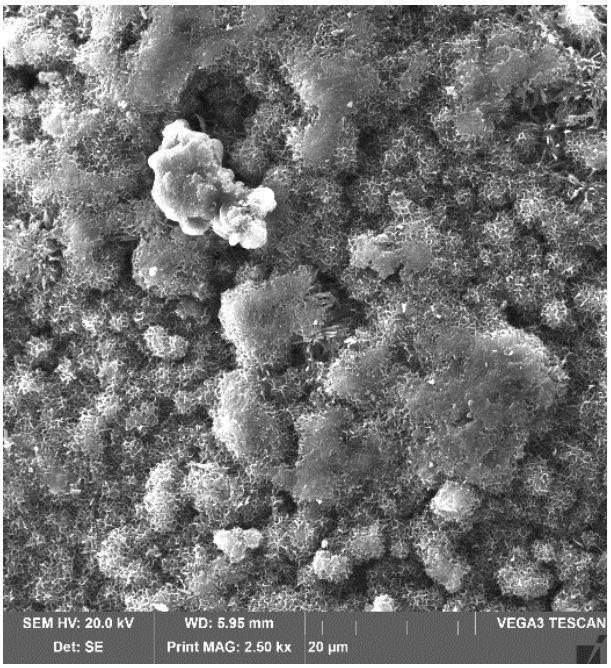

Figure 3.33 The surface of the ceramic proppant after its aging alone at 2.5 kx magnification. Reprinted from SPE-191225-MS.

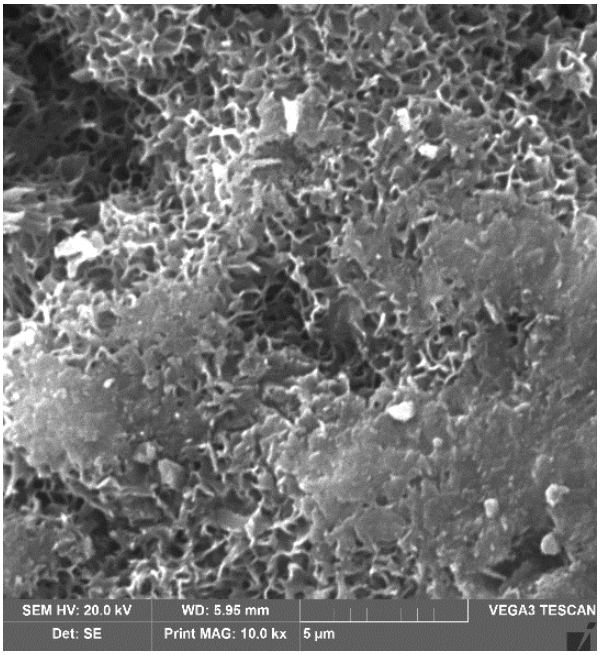

Figure 3.34 The surface of the ceramic proppant after its aging alone at 10.0 kx magnification. Reprinted from SPE-191225-MS.

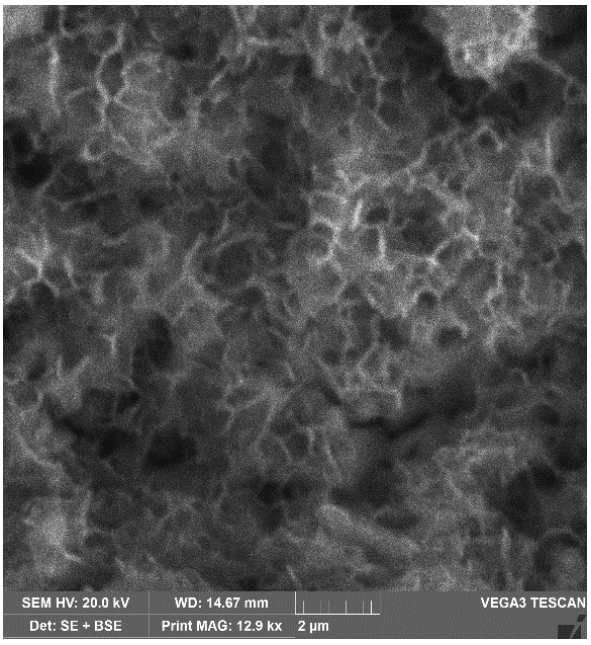

Figure 3.35 The surface of the ceramic proppant after its aging alone at 12.9 kx magnification. Reprinted from SPE-191225-MS.

Table 3.14 The EDS analysis of the ceramic proppant surface before and after its aging alone. Reprinted with permission from SPE-191225-MS.

Element	Concentration Before Aging, wt%	Concentration After Aging, wt%
Al	56.89	61.20
Fe	36.31	23.17
Si	3.39	15.62
Ti	3.39	Not detected

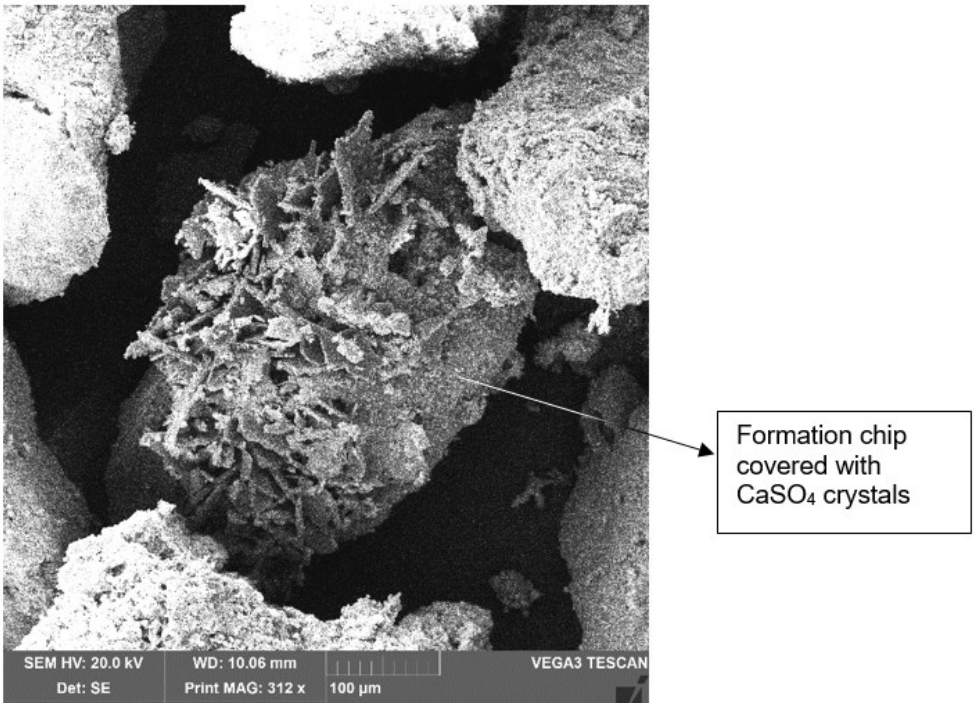

Figure 3.36 $CaSO_4$ crystals covering the surface of the formation after its aging alone. Reprinted from SPE-191225-MS.

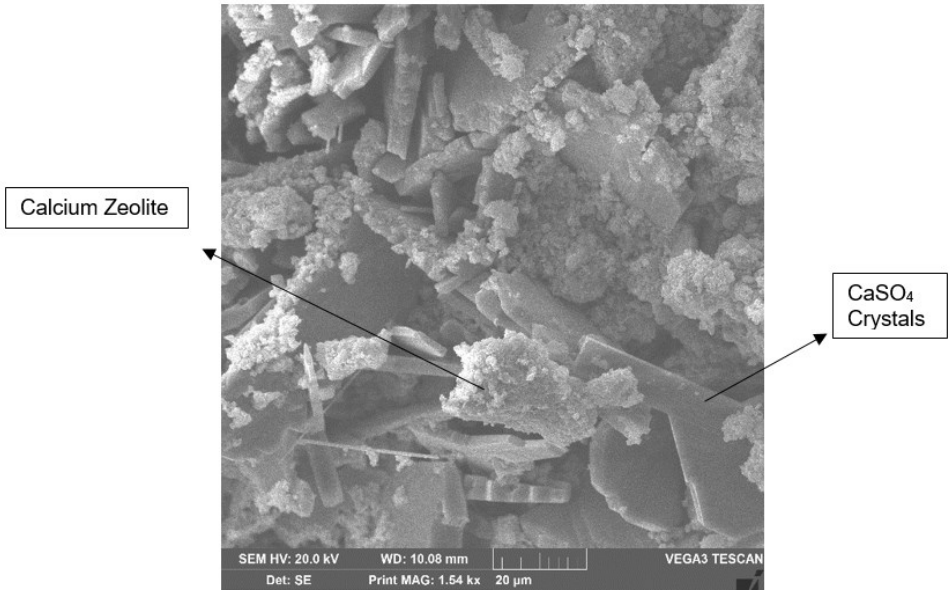

Figure 3.37 $CaSO_4$ crystals and calcium zeolite on the surface of the formation after its aging alone at 1.54 kx magnification. Reprinted from SPE-191225-MS.

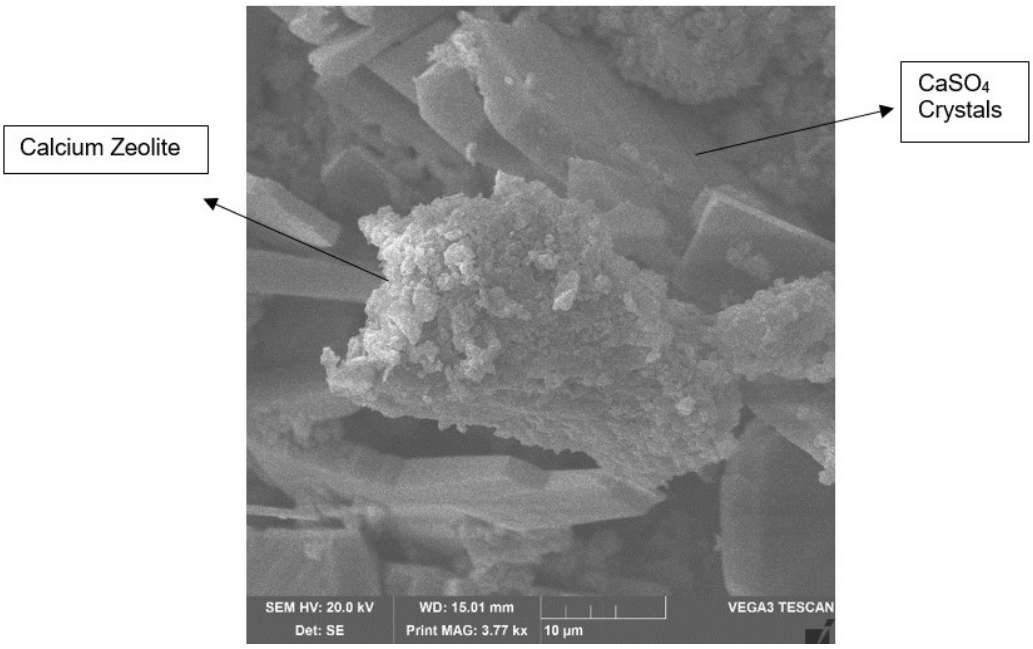

Figure 3.38 $CaSO_4$ crystals and calcium zeolite on the surface of the formation after its aging alone at 3.77 kx magnification. Reprinted from SPE-191225-MS.

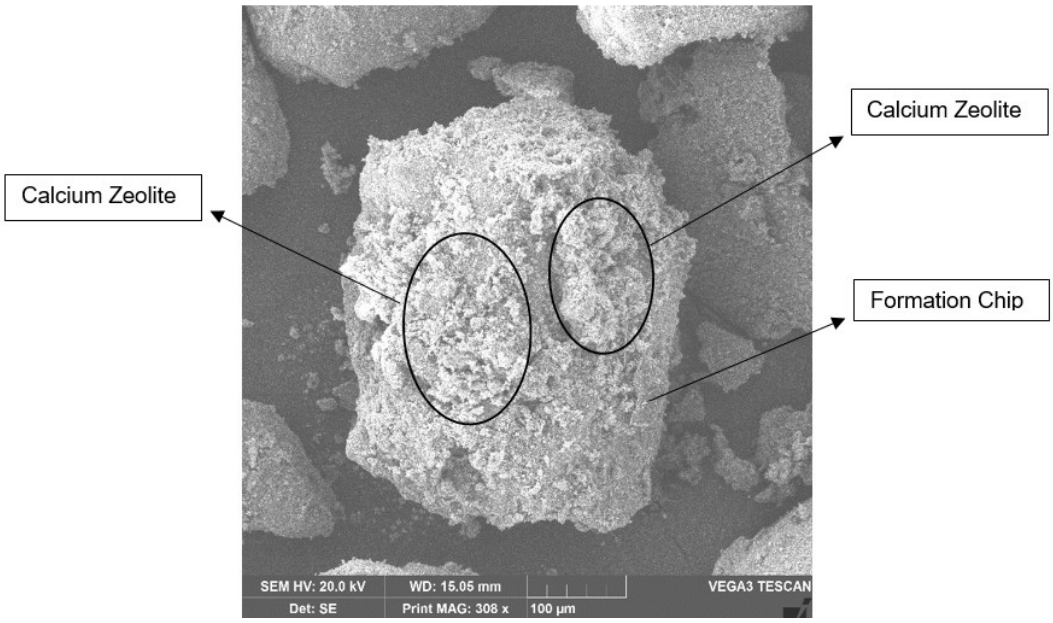

Figure 3.39 Calcium zeolite covering the surface of the formation after its aging alone. Reprinted from SPE-191225-MS.

3.3.2. Fluid Analysis

The supernatant solutions after aging the ceramic proppant and the formation, separately and together, were collected, filtered, and analyzed for the cations and sulfate content. The solutions (1), (2), and (3) refer to the supernatant solutions from aging the ceramic proppant/formation mixture, the ceramic proppant alone, and the formation alone, respectively. The analysis results are summarized in **Figure 3.40**. The results of supernatant solution of the aging of the ceramic proppant/formation mixture (solution 1) show high silicon, calcium, and sulfate concentrations. No significant aluminum, sodium, potassium, magnesium or iron concentrations are found in any of the supernatant samples (concentration < 15 ppm).

The supernatant solution 2 shows a high silicon content indicating the partial dissolution of the ceramic proppant after aging. The calcium and silicon are found to be the main cations leached into the solution from aging the formation, as shown in **Figure 3.40** (solution 3). The dissolution of the calcite and quartz minerals in the formation are the main sources of the calcium and silicon ions. The results of the sulfate measurements indicate the oxidation of pyrite in the Eagle Ford shale which causes the leaching of the sulfate ions into the solution. The following equation explains the oxidation of pyrite and its reaction products.

$$4\ FeS_2 + 4\ H_2O \quad \Longrightarrow \quad 4\ Fe^{2+} + 7\ S^{2-} + SO_4{}^{2-} + 8\ H^+$$

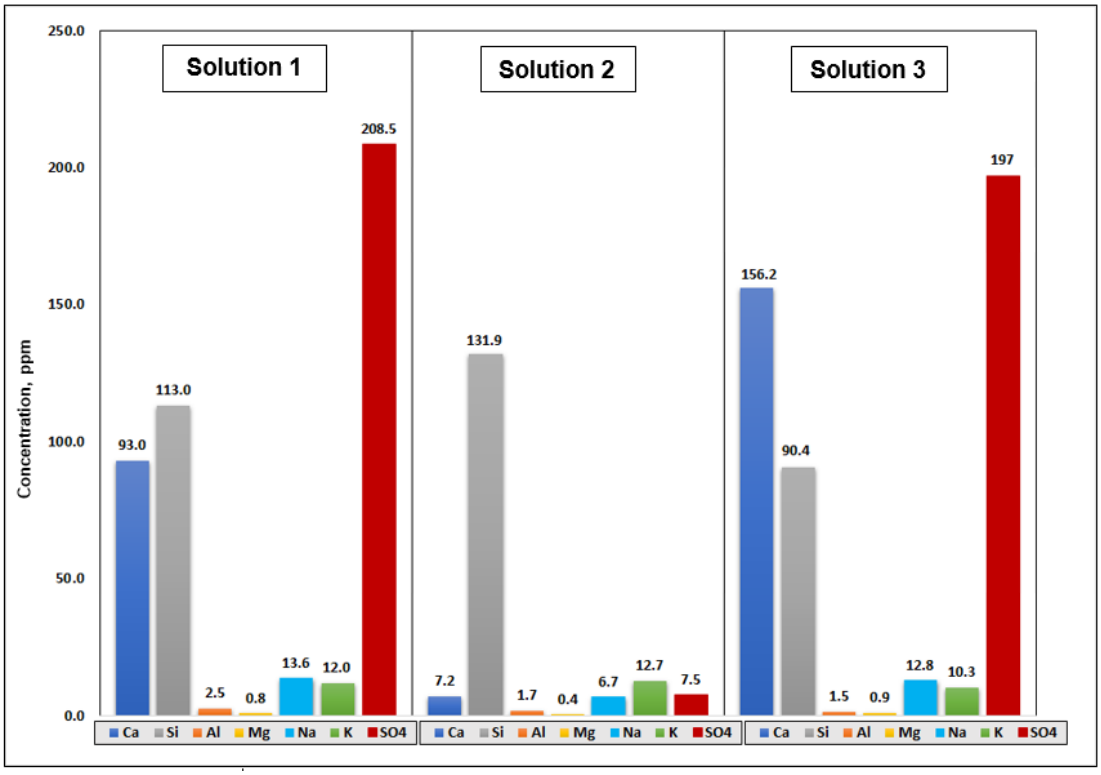

Figure 3.40 The analysis of the supernatant solutions after aging the ceramic proppant/formation mixture (solution 1), the ceramic proppant alone (solution 2), and the formation alone (solution 3). Reprinted from SPE-191225-MS.

The fluid analysis indicates that the ceramic proppant and Eagle Ford shale mixture, at elevated temperature, yields calcium and sulfate ions into the medium solution sourced from the formation, and yields silicon ions, sourced from both the ceramic proppant and the formation. Upon cooling, an ionic bond between the calcium and sulfate ions is formed and leads to the crystallization of $CaSO_4$. The formation of $CaSO_4$ has been previously observed by Lafollette and Carman (2013). Although no significant aluminum ion concentration was found in solution from the fluid analysis, a minor concentration of the aluminum ion could leach from the surfaces of both the formation and the proppant. The dissolution of the mullite and corundum minerals are

the sources of aluminum ion from the ceramic proppant. The dissolution of the clay and feldspar minerals are the sources of aluminum ion from the formation. The reaction between the calcium and silicon ions with the leached aluminum ions led to the precipitation of a calcium zeolite mineral on the surfaces of both the proppant and the formation.

Aven et al. (2013) observed a similar zeolite mineral when a calcium-rich water has been flowed through an intermediate strength proppant. The attachment of calcium and silicon ions to the ceramic proppant surface could combine with the iron from the proppant and led to the overgrowth on the proppant surface, iron-calcium zeolite. The interpretation of the results indicates that the formation of zeolite minerals could be sourced from the formation exclusively or from the interaction between the formation and the ceramic proppant. Different zeolite minerals could be formed on the proppant and formation surfaces as a result of their interaction with the medium solution.

3.4. Diagenesis of Sand and Resin-Coated Sand Proppants

3.4.1. SEM/EDS Analysis

The aging of sand and resin-coated sand proppants in the presence of the Eagle Ford shale precipitated $CaSO_4$ crystals. Such precipitate is observed after aging all cells containing the Eagle Ford shale formation regardless the proppant type. In addition, calcium zeolite precipitate was also observed after aging both types of proppants in the presence of the formation chips. However, its chemical composition is different from the previously identified calcium zeolite mineral after aging the ceramic proppant mixture with the formation. It contains higher silicon and lower calcium and aluminum

concentrations. **Figures 3.41 and 3.42** show the $CaSO_4$ and calcium zeolite precipitates observed on the sand proppant and the formation surfaces.

Figure 3.43 shows both precipitates at the magnification power of 5 kx. **Table 3.15** shows the EDS results that used to identify the observed precipitates. The observed zeolite precipitate was differentiated from the Eagle Ford shale formation using the different Ca and Si concentrations.

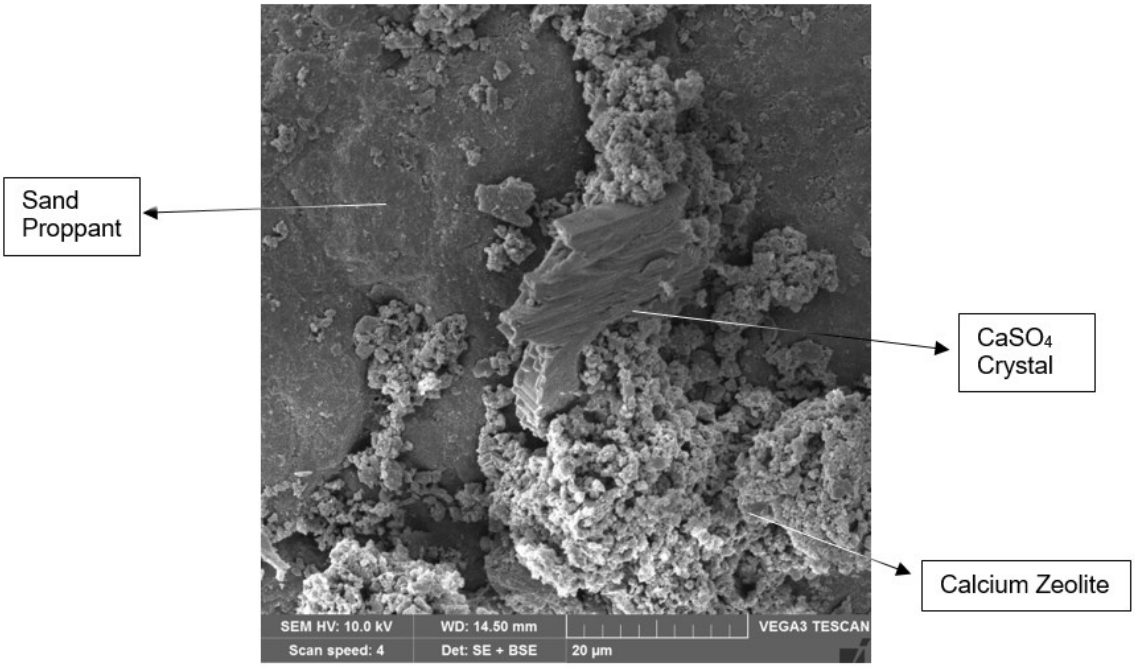

Figure 3.41 $CaSO_4$ and calcium zeolite precipitates on the surface of the sand proppant.

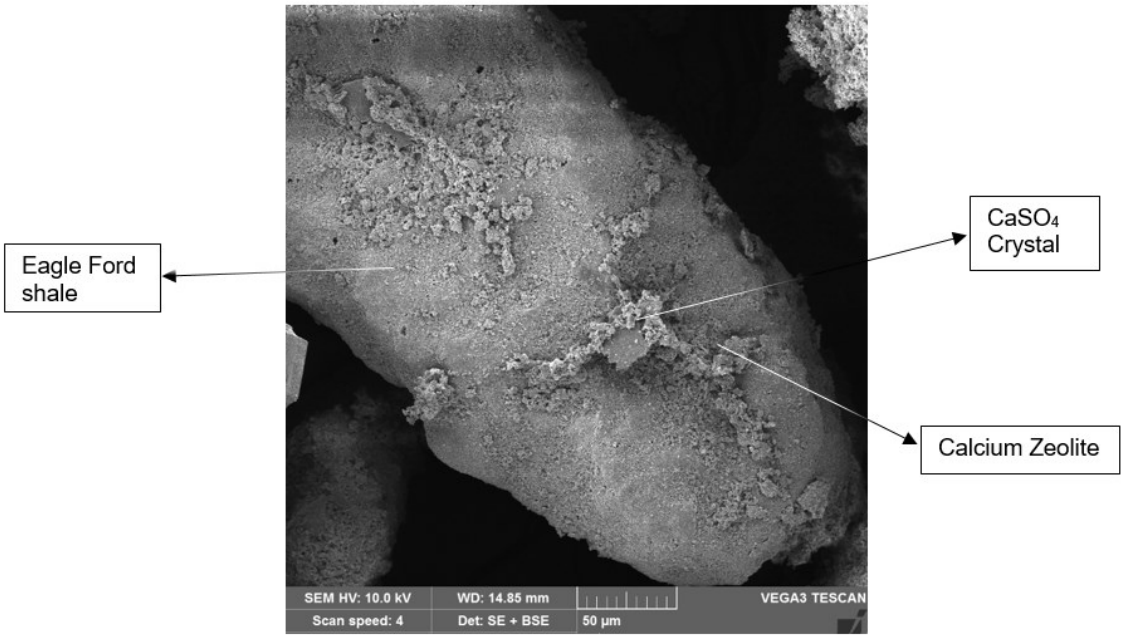

Figure 3.42 $CaSO_4$ crystal clumped with calcium zeolite on the surface of the formation chip.

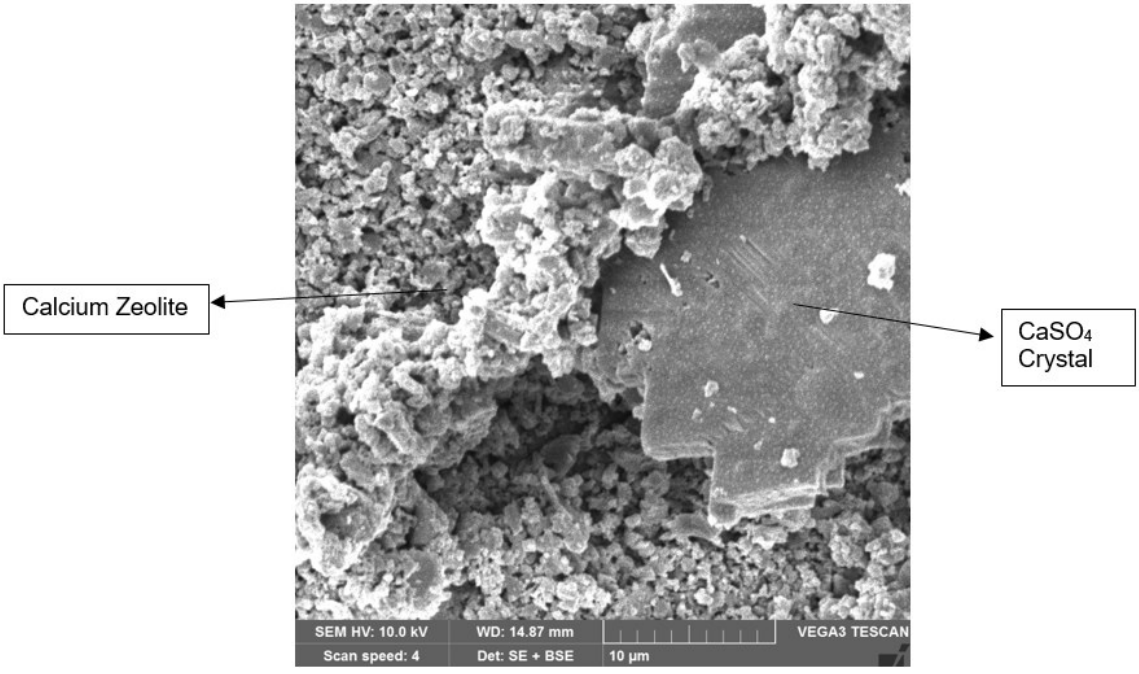

Figure 3.43 $CaSO_4$ crystal surrounded with calcium zeolite at 5 kx magnification.

Table 3.15 The EDS analysis of the sand proppant, the Eagle Ford formation, and the $CaSO_4$ and calcium zeolite precipitates observed after aging sand proppant mixture with the formation.

Element, wt%	Sand Proppant	$CaSO_4$	Calcium Zeolite	Eagle Ford formation
Ca	Not detected	56	26.2	52.22
Al	Not detected	Not detected	7.54	5.28
Si	43.2	Not detected	66.26	42.5
S	Not detected	44	Not detected	Not detected

Figures 3.44 through 3.46 show the $CaSO_4$ and calcium zeolite precipitates observed on top of the resin-coated sand proppant and the formation after aging. The observed precipitates has the same elemental composition as the previously observed in the case of sand proppant (**Table 3.15**).

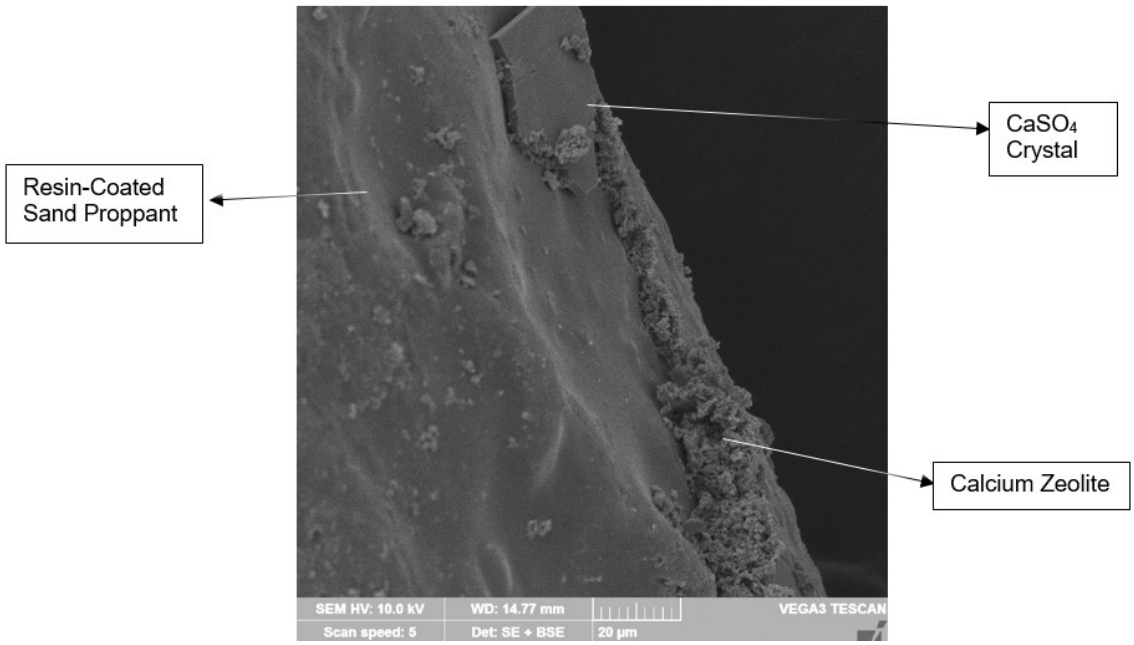

Figure 3.44 $CaSO_4$ and calcium zeolite on the surface of the resin-coated sand proppant.

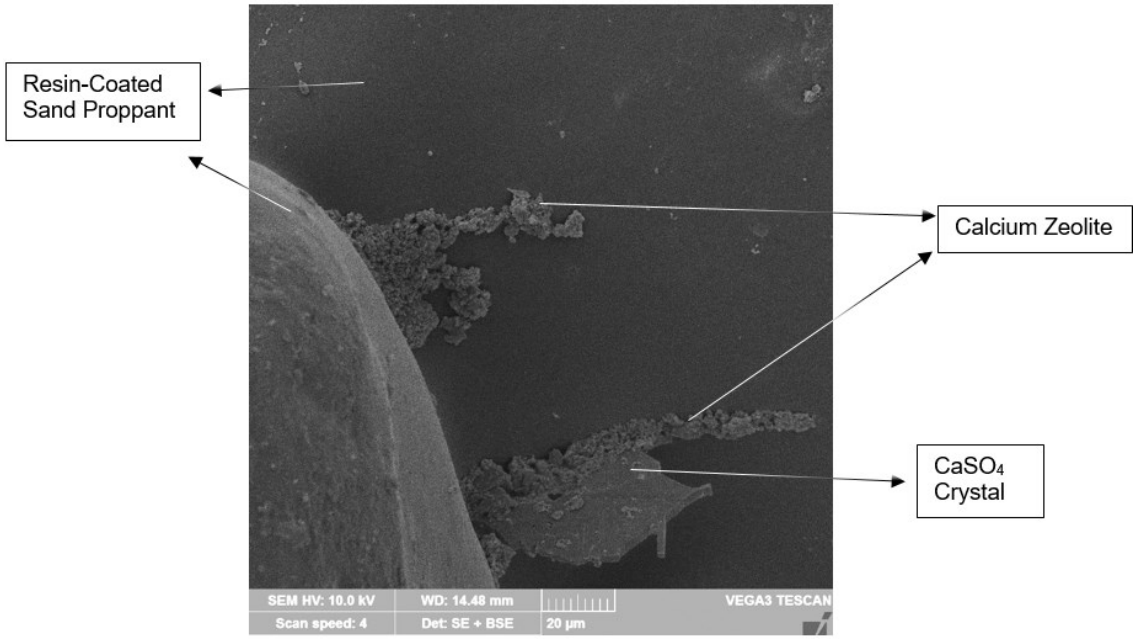

Figure 3.45 $CaSO_4$ and calcium zeolite in-between two resin-coated sand proppant particles.

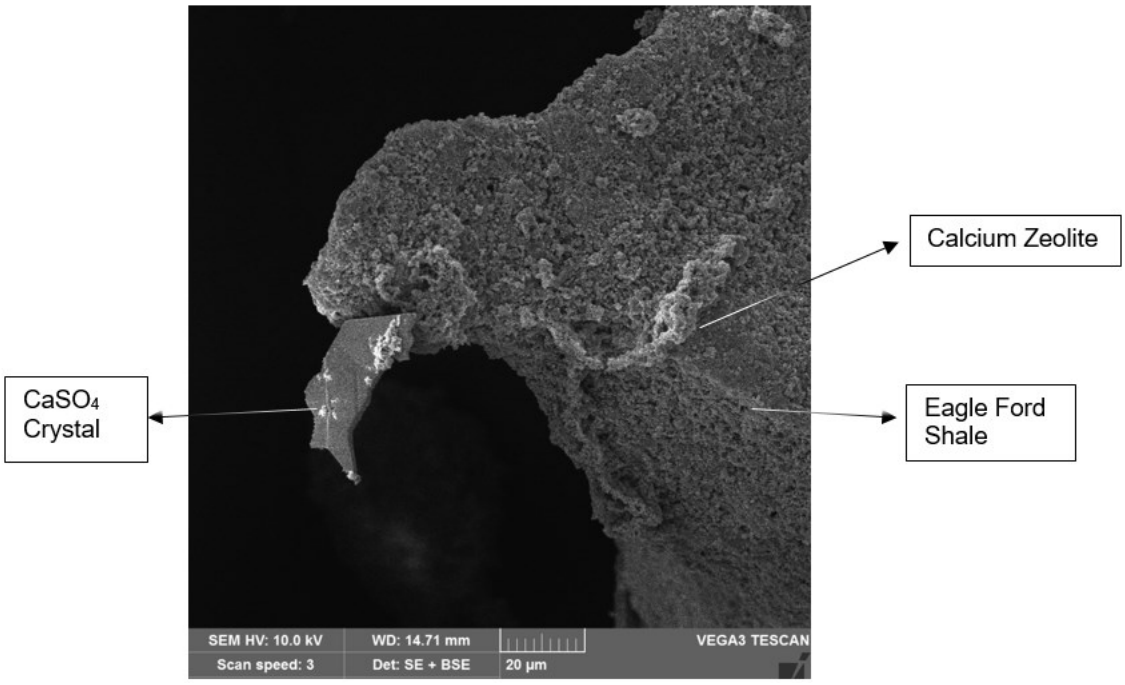

Figure 3.46 $CaSO_4$ and calcium zeolite on the surface of the Eagle Ford formation.

After the separate aging of sand and resin-coated sand proppants, no precipitates have been observed. However, the surface of the sand proppant indicated its partial dissolution, as shown from its surface disintegration in **Figures 3.47 and 3.48**. Moreover, the resin-coated sand showed the partial and complete peeling of the coating, as shown in **Figures 3.49 and 3.50**.

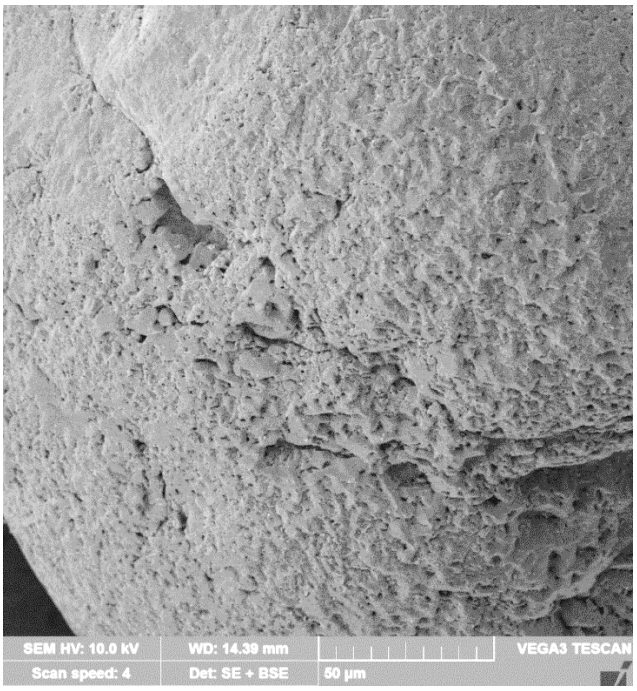

Figure 3.47 The surface of sand proppant after aging.

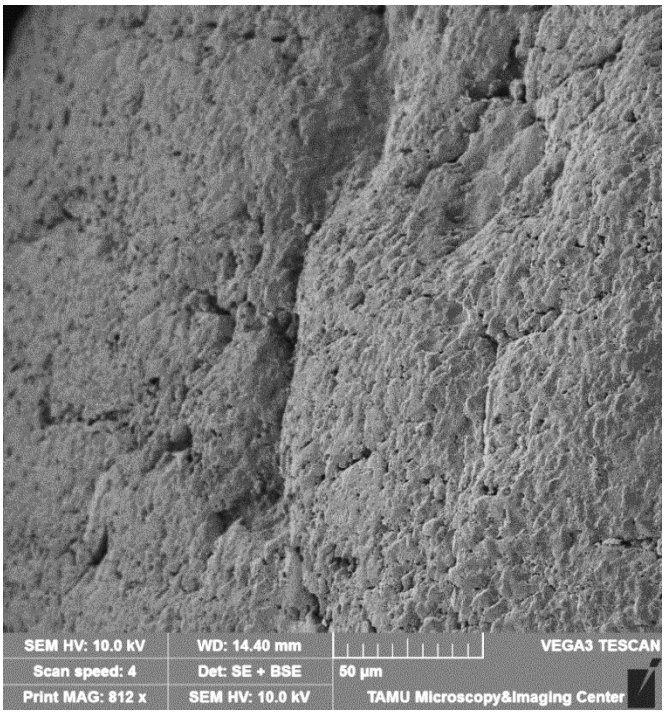

Figure 3.48 The surface of sand proppant after aging, at different location.

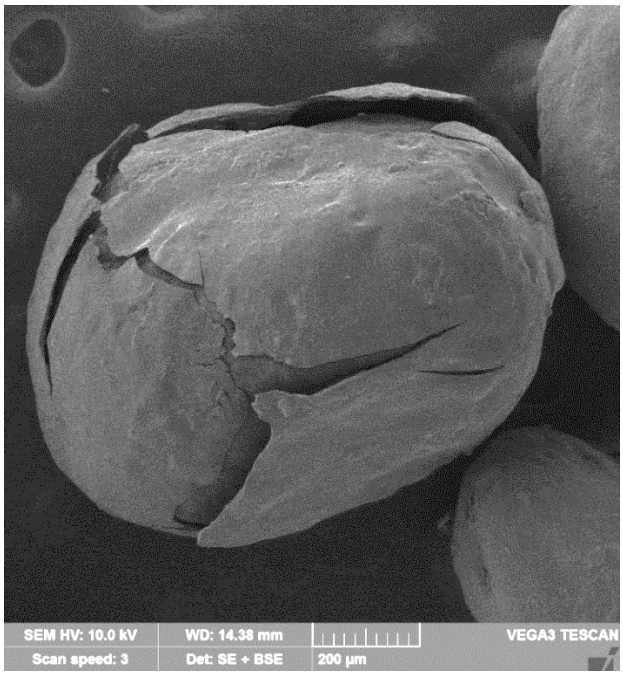

Figure 3.49 The surface of resin-coated sand proppant after aging.

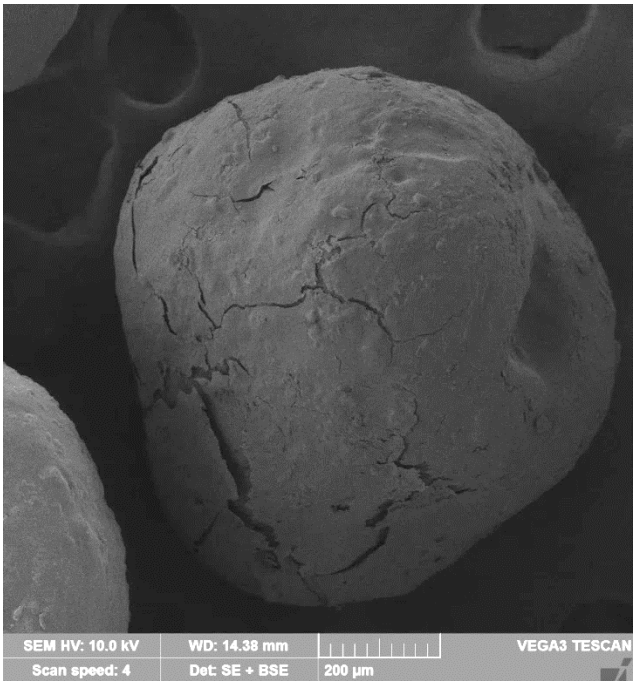

Figure 3.50 The surface of resin-coated sand proppant after aging, of another particle.

3.4.2. Fluid Analysis

The analysis of the supernatant fluids after the aging of the sand and resin-coated sand proppants showed similar results, in the two cases: aging alone and in the presence of the Eagle Ford shale formation. Only the silicon ion was observed after the separate aging of both proppants due to the dissolution of the quartz mineral. The silicon concentrations after the separate aging were found to be 37.4 and 42 ppm, for the sand and resin-coated sand proppants, respectively. Although the resin-coated sand is covered with a hydrophobic phenol formaldehyde layer, it did not prevent the dissolution of the proppant due to the breaking and peeling of its coating, as shown in **Figures 3.49 and 3.50**.

After the aging of both proppants in the presence of the formation, the silicon, calcium, and sulfate were the main ions observed in the fluid, as shown in **Figure 3.51**. The solutions (4) and (5) refer to the supernatant solutions from aging the sand proppant and resin-coated sand proppant, respectively, in the presence of the Eagle Ford shale formation. The silicon ion sourced from both the proppant and the formation, while the calcium and sulfate ions were sourced explicitly from the formation as previously observed in the case of the ceramic proppant.

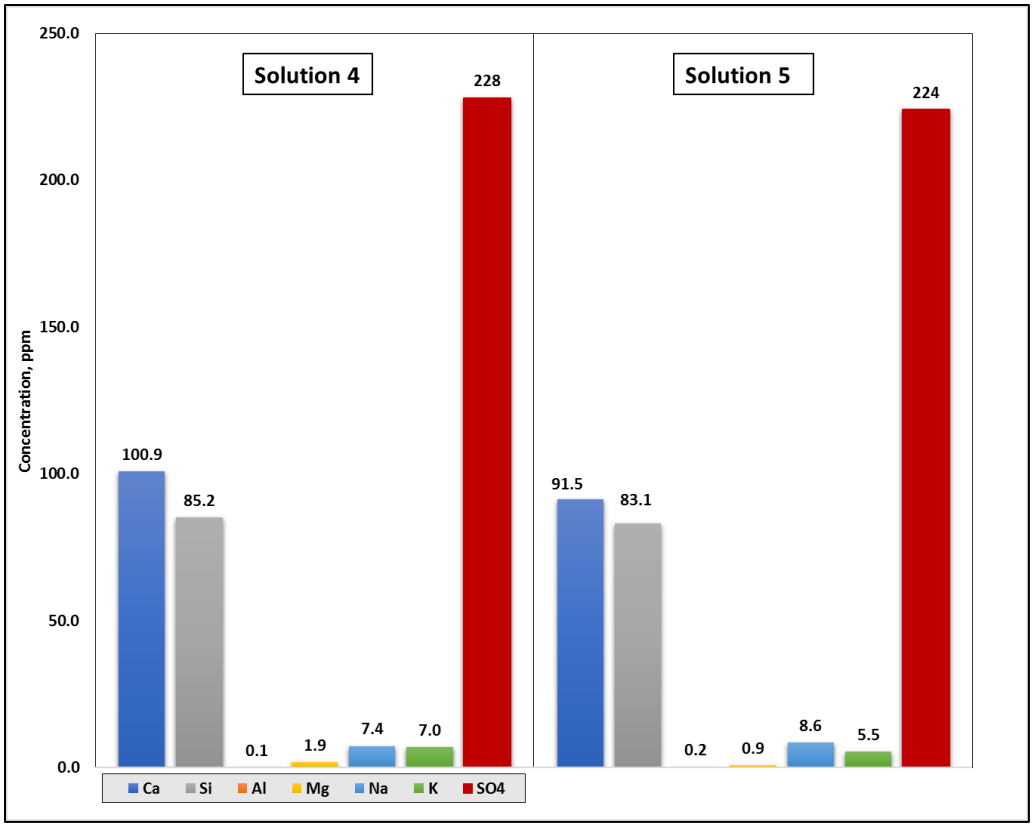

Figure 3.51 The analysis of the supernatant solutions after aging the sand (solution 4) and resin-coated sand (solution 5) proppants, in the presence of the Eagle Ford shale formation.

The previous results show that the sand and resin-coated sand proppants do not contribute to any precipitation or development of an overgrowth material; the Eagle Ford shale formation was the one source of the observed precipitates. The proppant dissolution, however, was the only observed sort of proppant diagenesis, which was indicated from the change of the surface morphology and the supernatant fluid analysis results. Such results are in agreement with the results of LaFallotte and Carman (2011) and Dunckel et al. (2012).

4. CONCLUSIONS AND RECOMMENDATIONS

A review study was done to evaluate the importance of fracture conductivity to the hydrocarbon production from shale reservoirs. The ceramic, sand, and resin-coated sand proppants were evaluated for the use in hydraulic fracturing of Eagle Ford shale through 1) measuring the fracture width and the proppant porosity at downhole conditions, and 2) the investigation of the proppant diagenesis process associated with each proppant type. On the basis of the obtained results, the following conclusions were drawn:

1. Although the shale reservoirs have an ultra-low matrix permeability, the improvement in fracture conductivity showed a significant increase in the well hydrocarbon production that can reach up to 150% of cumulative production in 3 years.
2. The propped fracture width and proppant porosity under stress depend on the proppant type, size, and concentration. **Tables 3.1 through 3.9** present the values of the fracture width and proppant porosity at different closure stresses.
3. Crushing of sand proppant decreases as the proppant size decreases and as the proppant concentration increases.
4. The proppant porosity under stress is directly proportional to the proppant strength and concentration and inversely proportional to the proppant size.

5. At 0.2 lb/ft^2, 20/40-mesh ceramic proppant formed a fracture with a partial monolayer of proppant and embedment due to stress reduced the fracture width by 29.2% at 8000 psia.
6. The 20/40-mesh resin-coated sand at 0.2 lb/ft^2 showed the highest reduction in fracture width and proppant porosity of 25.88 and 44.16%, respectively, while the 40/70-mesh ceramic proppant at 0.6 ft/ft^2 showed the minimum reduction of 5.68 and 7.88%, respectively, at 8000 psia closure stress.
7. The ceramic proppant contributed to the formation of calcium zeolite precipitation and led to the overgrowth of iron-calcium zeolite mineral due to the proppant diagenesis process in the presence of the Eagle Ford shale formation.
8. No overgrowth minerals due to diagenesis were observed from the use of sand and resin-coated sand proppants, however, their presence changed the chemistry of the precipitated zeolite from the interaction of the Eagle Ford shale formation with the fluid (increased the silicon and decreased the calcium and aluminum concentrations).
9. The chemical interaction between the Eagle Ford shale and water precipitated $CaSO_4$ and calcium zeolite.
10. All proppants, ceramic, sand, and resin-coated sand, undergo dissolution and yield silicon ion into the solution (132, 85, and 83 ppm, respectively).

11. Although the resin-coated sand is coated with a hydrophobic material, its diagenesis led to the partial and complete peeling of its coating and its further dissolution.

The study provides information of the propped fracture width and proppant porosity under stress that can be used in well production models, reservoir simulation models, and fracture design calculations. The results can also be used in the proppant selection process to improve the fracture conductivity and maximize the well productivity of Eagle Ford shale formations.

Furthermore, the results of the proppant/formation/fluid interactions showed that the use of a scale inhibitor in the fracture fluid could be necessary to prevent scale formation due to rock/fluid interactions, especially for fractured wells with long shut-in period. Furthermore, the study suggests that a care should be taken before the selection of ceramic proppant for fracturing Eagle Ford shale formations. Even though the ceramic proppant experiences less crushing than sand and resin-coated sand, its diagenesis process can induce a new material overgrowth on its surface and reduces the fracture conductivity. Therefore, the effect of proppant diagenesis and proppant crushing on fracture conductivity need to be evaluated, and combined for the optimization of the proppant selection process.

The following list presents our recommendations for possible future work:

1. Performing fracture conductivity tests for each proppant type and concentration at the same downhole conditions used in our studies to evaluate

the combined effect of the proppant-related damaging mechanisms on the fracture conductivity.

2. In the case of the absence of the fracture conductivity cell, we recommend the performing of the proppant sieve analysis at each stress step to determine the proppant size distribution after crushing. The particle size distribution along with the measured proppant porosity can then be used to calculate the proppant pack permeability using porosity/permeability relations, such as, Kozeny-Carmen equation. The evaluation of the two parameters will provide a better approach for the proppant selection process.
3. Testing the effect of shale mineralogy on the proppant embedment/compaction and the proppant diagenesis processes by using different shale samples, such as, Barnett, Haynesville, Marcellus, and Mancos shale. This will help to generalize our results to more unconventional shale oil and gas fields.
4. Experimentally investigate the effect of proppant diagenesis on the proppant crushing and compaction inside the fracture by performing the proppant evaluation experiment on the proppant that has been recovered from the diagenesis experiment. Doing the two experiments consecutively will help investigate the combined effect of the proppant diagenesis and the proppant crushing, embedment, and compaction mechanisms on the proppant porosity and fracture width.

5. Performing a cost analysis for the required scale inhibitor to prevent precipitation from the interactions between the formation and the fracture fluid to determine the degree of its necessity. Furthermore, the compatibility of the scale inhibitor with the fracture fluid additives should be tested before its application in the hydraulic fracturing operations.
6. Finally, we recommend the consideration of the cost of each proppant type in the proppant selection and completion optimization processes. Based on our discussion with different representatives from operator companies, the in-basin prices (prices when the proppant is shipped from the same basin) of ceramic, sand, and resin-coated sand are $170 to 220, 60 to 85, and 120 to 160 USD/ton of proppant, respectively. The comparison between these price differences and the gained hydrocarbon production from the use of each type should be considered for the economic success of the completion operation of unconventional shale formations.

REFERENCES

Alramahi, B. and Sundberg, M. I. 2012. Proppant Embedment and Conductivity of Hydraulic Fractures in Shales. Presented at the 46th U.S. Rock Mechanics/Geomechanics Symposium, Chicago, Illinois, 24-27 June. ARMA-2012-291.

American Petroleum Institute, API RP 61. 1989. Recommended Practices for Evaluating Short Term Proppant Pack Conductivity. First Edition.

American Petroleum Institute, API RP 19D. 2008. Measuring the Long-term Conductivity of Proppants. First Edition.

API Recommended Practice 19C. 2006. Measurement of Properties of Proppants Used in Hydraulic Fracturing and Gravel-packing Operations. API Standards Dept. 1st Edition.

API Recommended Practice 19D. 2008. Measuring the Long-term Conductivity of Proppants. API Standards Dept. 1st Edition.

Aven, N. K., Weaver, J., Loghry, R. et al. 2013. Long-Term Dynamic Flow Testing of Proppants and Effect of Coatings. Presented at the SPE European Formation Damage Conference & Exhibition, Noordwijk, The Netherlands, 5-7 June. SPE-165118-MS. https://doi.org/10.2118/165118-MS.

Barree, R. D., Miskimins, J. L., Conway, M. W. et al. 2016. Generic Correlations for Proppant Pack Conductivity. Presented at the SPE Hydraulic Fracturing Technology Conference, The Woodlands, Texas, 9-11 February. SPE-179135-MS. http://dx.doi.org/10.2118/179135-MS.

Barree, R. D., Cox, S. A., Barree, V. L. et al. 2003. Realistic Assessment of Proppant Pack Conductivity for Material Selection. Presented at the SPE Annual Technical Conference and Exhibition, Denver, Colorado, 5-8 October. SPE-84306-MS. https://doi.org/10.2118/84306-MS.

Bazan, L. W., Larkin, S. D., Lattibeaudiere, M. G. et al. 2010. Improving Production of the Eagle Ford Shale with Fracture Modeling, Increased Conductivity and Optimized Stage and Cluster Spacing Along the Horizontal Wellbore. Presented at the SPE Tight Gas Completions Conference, San Antonio, Texas, 2-3 November. SPE-138425-MS. https://doi.org/10.2118/138425-MS.

Bazan, L. W., Lattibeaudiere, M. G., and Palisch, T. T. 2012. Hydraulic Fracture Design and Well Production Results in the Eagle Ford Shale: One Operator's Perspective. Presented at the SPE Americas Unconventional Resources Conference, Pittsburgh, Pennsylvania, 5-7 June. SPE-155779-MS. https://doi.org/10.2118/155779-MS.

Becq, D. F., Claude, R., and Sarda, J. P. 1984. High-Strength Proppants Behavior Under Extreme Conditions. Presented at the SPE Formation Damage Control Symposium, Bakersfield, California, 13-14 February. SPE-12487-MS. https://doi.org/10.2118/12487-MS.

Bhattacharya, S. and Nikolaou, M. 2016. Comprehensive Optimization Methodology for Stimulation Design of Low-Permeability Unconventional Gas Reservoirs. *SPE J.* **21** (03): 947-964. SPE-147622-PA. https://doi.org/10.2118/147622-PA.

Chapman, M. and Palisch, T. 2014. Fracture conductivity – Design considerations and benefits in unconventional reservoirs. *Journal of Petroleum Science and Engineering* **124**: 407-415. https://doi.org/10.1016/j.petrol.2014.09.015.

Chen, D., Ye, Z., Pan, Z. et al. 2016. A Permeability Model for Hydraulic Fracture Filled with Proppant Packs Under Combined Effect of Compaction and Embedment. *Journal of Petroleum Science and Engineering* **149**: 428-435.

Cook, D., Downing, K., Bayer, S. et al. 2014. Unconventional Asset Development Work Flow in the Eagle Ford Shale. Presented at the SPE Unconventional Resources Conference, The Woodlands, Texas, 1-3 April. SPE-168973-MS. https://doi.org/10.2118/168973-MS.

Cooke, C. E. 1975. Effect of Fracturing Fluids on Fracture Conductivity. *JPT* **27** (10): 1273-1282. SPE-5114-PA. https://doi.org/10.2118/5114-PA.

Duenckel, R., Moore, N., O'Connell, L. et al. 2016. The Science of Proppant Conductivity Testing- Lessons Learned and Best Practices. Presented at the SPE Hydraulic Fracturing Technology Conference, The Woodlands, Texas, 9-11 February. SPE-179125-MS. https://doi.org/10.2118/179125-MS.

Duenckel, R., Conway, M. W., Eldred, B. et al. 2011. Proppant Diagenesis - Integrated Analyses Provide New Insights Into Origin, Occurrence, And Implications For Proppant Performance. Presented at the SPE Hydraulic Fracturing Technology Conference, The Woodlands, Texas, 24-26 January. SPE-139875-MS. https://doi.org/10.2118/139875-MS.

Duenckel, R., Conway, M. W., Eldred, B. et al. 2012. Proppant Diagenesis--Integrated Analyses Provide New Insights Into Origin, Occurrence, and Implications for Proppant Performance. *SPE Journal* **27** (02): 131-144. SPE-139875-PA. https://doi.org/10.2118/139875-PA.

Economides, M. J., Martin, A. N., and Valkó, P. 2002. Unified Fracture Design. *Orsa Press*, Houston.

Economides, M. J., Hill, A. D., Ehlig-Economides, C. et al. 2012. Petroleum Production Systems. Prentice Hall, Upper Saddle River, NJ.

Elsarawy, A. M., Nasr-El-Din, H. A., and Cawiezel, K. E. 2016. Laboratory Study on Using Produced Water in High pH Borate Gels Used in Hydraulic Fracturing. Presented at the SPE Improved Oil Recovery Conference, Tulsa, Oklahoma, 11-13 April. SPE-179553-MS. https://doi.org/10.2118/179553-MS.

Elsarawy, A. M. and Nasr-El-Din, H. A. 2018. Propped Fracture Conductivity in Shale Reservoirs: A Review of its Importance and Roles in Fracturing Fluid Engineering. Presented at the SPE Kingdom of Saudi Arabia Annual Technical Symposium and Exhibition, Dhahran, Saudi Arabia, 23-26 April. SPE-192451-MS. https://doi.org/10.2118/192451-MS.

Elsarawy, A. M. and Nasr-El-Din, H. A. 2018. Experimental Evaluation of Sand Porosity in Eagle Ford Shale Fractures. Presented at the SPE Trinidad and Tobago Energy Resources Conference, Port of Spain, Trinidad and Tobago, 25-26 June. SPE-191240-MS. https://doi.org/10.2118/191240-MS.

Elsarawy, A.M. and Nasr-El-Din, H.A. 2018. An Experimental Investigation of Proppant Diagenesis and Proppant-Formation-Fluid interactions in Hydraulic Fracturing of Eagle Ford Shale. Presented at the SPE Trinidad and Tobago Energy Resources Conference, Port of Spain, Trinidad and Tobago, 25-26 June. SPE-191225-MS. https://doi.org/10.2118/191225-MS.

Fan, M., Han, Y., McClure, J. et al. 2017. Hydraulic Fracture Conductivity as a Function of Proppant Concentration under Various Effective Stresses: from Partial Monolayer to Multilayer Proppants. Presented at the Unconventional Reseources Technology Conference, Austin, Texas, 24-26 July. URTEC-2693347-MS. https://doi.org/10.15530/URTEC-2017-2693347.

Forchheimer, P. 1901. Wasserbewegung durch Boden. 45th Edition, Zeitschrift des Vereins Deutscher Ingenieure, Düsseldorf.

Gidley, J. L., Holditch, S. A. et al. 1989. Recent Advances in Hydraulic Fracturing. *SPE Monograph Series Vol. 12*, Society of Petroleum Engineers.

Jangda, Z. Z. and Al-Nuaim, S. 2014. Application of Unified Fracture Design to Higher Permeability Reservoirs. Presented at the Abu Dhabi International Petroleum Exhibition and Conference, Abu Dhabi, 10-13 November. SPE-172047-MS. http://dx.doi.org/10.2118/172047-MS.

Holditch, S. A. 2006. Tight Gas Sands. *JPT* **58** (06): 86-93. SPE-103356-JPT. https://doi.org/10.2118/103356-JPT.

Hua, M., Yongjun, L., Baoshan, G. et al. 2016. A cellulose Fracturing Fluid with Instant Solution and No Residue. Presented at the SPE Asia Pacific Oil & Gas

Conference and Exhibition, Perth, Australia, 25-27 October. SPE-182374-MS. https://doi.org/10.2118/182374-MS.

Ibrahim, A. F., Nasr-El-Din, H. A., Rabie, A. et al. 2016. A Non-Damaging Friction Reducing Agent for Slick-Water Fracturing. Presented at the SPE Western Regional Meeting, Anchorage, Alaska, 23-26 May. SPE-180436-MS. https://doi.org/10.2118/180436-MS.

Kadau, D., Bartels, G., Brendel, L. et al. 2010. Pore Stabilization in Cohesive Granular Systems. *Phase Transitions* 76:4-5, 315-331. DOI: 10.1080/01411590210000051460.

LaFollette, R. F. and Carman, P. S. 2010. Proppant Diagenesis: Results So Far. Presented at the SPE Unconventional Gas Conference, Pittsburgh, Pennsylvania, 23-25 February. SPE-131782-MS. https://doi.org/10.2118/131782-MS.

LaFollette, R. F. and Carman, P. S. 2011. Long Term Stability of Proppants Exposed To Harsh Shale Reservoir Conditions. Presented at the SPE Hydraulic Fracturing Technology Conference, The Woodlands, Texas, 24-26 January. SPE-140110-MS. https://doi.org/10.2118/140110-MS.

Lafollette, R. F. and Carman, P. S. 2013. Comparison of the Impact of Fracturing Fluid Compositional pH on Fracture Wall Properties in Different Shale Formation Samples. Presented at the SPE Annual Technical Conference and Exhibition, New Orleans, Louisiana, 30 September-2 October. SPE-166471-MS. https://doi.org/10.2118/166471-MS.

Lee, D. S., Elsworth, D., Yasuhara, H. et al. 2009. An Evaluation of the Effect of Fracture Diagenesis on Fracture Treatments: Modeled Response. Presented at the 43rd US Rock Mechanics Symposium and 4th US-Canada Rock Mechanics Symposium, Asheville, North Carolina, 28 June-1 July.

Lee, D. S., Elsworth, D., Yasuhara, H. et al. 2010. Experiment and Modeling to Evaluate the Effects of Proppant-Pack Diagenesis on Fracture Treatments. *Journal of Petroleum Science and Engineering* **74**: 67-76.

Marongiu-Porcu, M., Economides, M. J., and Holditch, S. A. 2008. Economic and Physical Optimization of Hydraulic Fracturing. Presented at the SPE International Symposium and Exhibition on Formation Damage Control, Lafayette, Louisiana, 13-15 February. SPE-111793-MS. http://dx.doi.org/10.2118/111793-MS.

Mayerhofer, M. J., Lolon, E. P., Youngblood, J. E. et al. 2006. Integration of Microseismic-Fracture-Mapping Results With Numerical Fracture Network Production Modeling in the Barnett Shale. Presented at the SPE Annual Technical Conference and Exhibition, San Antonio, Texas, 24-27 September. SPE-102103-MS. https://doi.org/10.2118/102103-MS.

McDaniel, B. W. 1986. Conductivity Testing of Proppants at High Temperature and Stress. Presented at the SPE California Regional Meeting, Oakland, California, 2-4 April. SPE-15067-MS. https://doi.org/10.2118/15067-MS.

McGuire, W. J. and Sikora, V. J. 1960. The Effect of Vertical Fractures on Well Productivity. *JPT* **12** (10): 72-74.

Mendoza, E. E., Aular, J., and Sousa, L. J. 2011. Optimizing Horizontal-Well Hydraulic-Fracture Spacing in the Eagle Ford Formation, Texas. Presented at the North American Unconventional Gas Conference and Exhibition, The Woodlands, Texas, 14-16 June. SPE-143681-MS. https://doi.org/10.2118/143681-MS.

Nasr-El-Din, H. A. and Samuel, M. 2007. Lessons Learned From Using Viscoelastic Surfactants in Well Stimulation. *SPE Prod & Oper* **22** (01): 112-120. SPE-90383-PA. https://doi.org/10.2118/90383-PA.

Nguyen, P. D., Weaver, J. D., and Rickman, R. D. 2008. Prevention of Geochemical Scaling in Hydraulically Created Fractures: Laboratory and Field Studies. Presented at the SPE Eastern Regional/AAPG Eastern Section Joint Meeting, Pittsburgh, Pennsylvania, 11-15 October. SPE-118175-MS. https://doi.org/10.2118/118175-MS.

Olson, K. E., Haidar, S., Milton-Tayler, D. et al. 2004. Multiphase Non-Darcy Pressure Drop in Hydraulic Fracturing. Presented at the SPE Annual Technical Conference and Exhibition, Houston, Texas, 26-29 September. SPE-90406-MS. https://doi.org/10.2118/90406-MS.

Ozden, S., Li, L., Al-Muntasheri, G. et al. 2017. Nanomaterials-Enhanced High-Temperature Viscoelastic Surfactant VES Well Treatment Fluids. Presented at the SPE International Conference on Oilfield Chemistry, Montgomery, Texas, 3-5 April. SPE-184551-MS. https://doi.org/10.2118/184551-MS.

Palisch, T. T., Duenckel, R., Chapman, M. et al. 2010. How To Use and Misuse Proppant Crush Tests: Exposing The Top 10 Myths. *SPE Prod & Oper* **25** (03): 345-354. SPE-119242-PA. https://doi.org/10.2118/119242-PA.

Palisch, T. T., Chapman, M. A., and Godwin, J. W. 2012. Hydraulic Fracture Design Optimization in Unconventional Reservoirs - A Case History. Presented at the SPE Annual Technical Conference and Exhibition, San Antonio, Texas, 8-10 October. SPE-160206-MS. https://doi.org/10.2118/160206-MS.

Palisch, T. T., Duenckel, R. J., Bazan, L. W. et al. 2007. Determining Realistic Fracture Conductivity and Understanding its Impact on Well Performance - Theory and Field Examples. Presented at the SPE Hydraulic Fracturing Technology Conference, College Station, Texas, 29-31 January. SPE-106301-MS. https://doi.org/10.2118/106301-MS.

Penny, G. S. 1987. An Evaluation of the Effects of Environmental Conditions and Fracturing Fluids Upon the Long-Term Conductivity of Proppants. Presented at the SPE Annual Technical Conference and Exhibition, Dallas, Texas, 27-30 September. SPE-16900-MS. https://doi.org/10.2118/16900-MS.

Penny, G. S., Crafton, J. W., Champagne, L. M. et al. 2012. Proppant and Fluid Selection to Optimize Performance of Horizontal Shale Fracs. Presented at the SPE Hydraulic Fracturing Technology Conference, The Woodlands, Texas, 6-8 February. SPE-152119-MS. https://doi.org/10.2118/152119-MS.

Penny, G. S. and Jin, L. 1995. The Development of Laboratory Correlations Showing the Impact of Multiphase Flow, Fluid, and Proppant Selection upon Gas Well Productivity. Presented at the SPE Annual Technical Conference and Exhibition, Dallas, Texas, 22-25 October. SPE-30494-MS. https://doi.org/10.2118/30494-MS.

Pope, C. D., Palisch, T., and Saldungaray, P. 2012. Improving Completion and Stimulation Effectiveness in Unconventional Reservoirs- Field Results in The Eagle Ford Shale of North America. Presented at the SPE/EAGE European Unconventional Resources Conference and Exhibition, Vienna, Austria, 20-22 March. SPE-152839-MS. https://doi.org/10.2118/152839-MS.

Ramurthy, M., Barree, R. D., Kundert, D. P. et al. 2011. Surface Area vs Conductivity Type Fracture Treatments in Shale Reservoirs. Presented at the SPE Hydraulic Fracturing Technology Conference, The Woodlands, Texas, 24-26 January. SPE-140169-MS. https://doi.org/10.2118/140169-MS.

Ran, B. and Kelkar, M. 2015. Fracture Stages Optimization in Bakken Shale Formation. Presented at the Unconventional Resources Technology Conference, San Antonio, Texas, 20-22 July. SPE-2154796-MS. https://doi.org/10.2118/2154796-MS.

Rankin, R. R., Thibodeau, M., Vincent, M. C. et al. 2010. Improved Production and Profitability Achieved With Superior Completions in Horizontal Wells: A Bakken/Three Forks Case History. Presented at the SPE Annual Technical Conference and Exhibition, Florence, Italy, 19-22 September. SPE-134595-MS. https://doi.org/10.2118/134595-MS.

Raysoni, N. and Weaver, J. 2012. Improved Understanding of Proppant-Formation Interactions for Sustaining Fracture Conductivity. Presented at the SPE Saudi Arabia Section Technical Symposium and Exhibition, Al-Khobar, Saudi Arabia, 8-11 April. SPE-160885-MS. https://doi.org/10.2118/160885-MS.

Raysoni, N. and Weaver, J. 2013. Long-Term Hydrothermal Proppant Performance. *SPE Prod & Oper* **28** (04): 414-426.SPE-150669-PA. https://doi.org/10.2118/150669-PA.

Saldungaray, P. M. and Palisch, T. T. 2012. Hydraulic Fracture Optimization in Unconventional Reservoirs. Presented at the SPE Middle East Unconventional Gas Conference and Exhibition, Abu Dhabi, UAE, 23-25 January. SPE-151128-MS. https://doi.org/10.2118/151128-MS.

Shelly, R., Guliyev, N., and Nejad, A. 2012. A Novel Method to Optimize Horizontal Bakken Completions in a Factory Mode Development Program. Presented at the SPE Annual Technical Conference and Exhibitions, San Antonio, Texas, 8-10 October. SPE-159696-MS. https://doi.org/10.2118/159696-MS.

Smith, M. B. and Montgomery, C. 2015. *Hydraulic Fracturing*. CRC Press, Taylor and Francis Group, Boca Raton, FL.

Song, B., Economides, M. J., and Ehlig-Economides, C. 2011. Design of multiple transverse fracture horizontal Wells in shale gas reservoirs. Presented at the SPE Hydraulic Fracturing Technology Conference, The Woodlands, Texas, 24-26 January. SPE-140555-MS. https://doi.org/10.2118/140555-MS.

Stephens, W. T., Schubarth, S. K., Dickson, K. R. et al. 2007. Behavior of Proppants Under Cyclic Stress. Presented at the SPE Hydraulic Fracturing Technology Conference, College Station, Texas, 29-31 January. SPE-106365-MS. https://doi.org/10.2118/106365-MS.

Shamsi, M. M., Nia, S. F., and Jessen, K. 2015. Conductivity of Proppant-Packs under Variable Stress Conditions: An Integrated 3D Discrete Element and Lattice Boltzman Method Approach. Presented at the SPE West Regional Meeting, Garden Grove, California, 27-30 April. SPE-174046-MS. http://dx.doi.org/10.2118/174046-MS.

Sun, J. and Schechter, D. 2015. Investigating the Effect of Improved Fracture Conductivity on Production Performance of Hydraulically Fractured Wells: Field-Case Studies and Numerical Simulations. *Journal of Canadian Petroleum Technology* **54** (06): 442-449.

U.S. EIA Energy Information Administration. 2018. U.S. Crude Oil and Natural Gas Proved Reserves, Year-end 2016. U.S. Department of Energy, Washington, DC 20585.

Vincent, M. C. 2009. Examining Our Assumptions – Have oversimplifications Jeopardized Our Ability To Design Optimal Fracture Treatments? Presented at the SPE Hydraulic Fracturing Technology Conference, The Woodlands, Texas, 19-21 January. SPE-119143-MS. https://doi.org/10.2118/119143-MS.

Vincent, M. C. 2010. Refracs: Why Do They Work, and Why Do They Fail in 100 Published Field Studies? Presented at the SPE Annual Technical Conference and Exhibition, 19-22 September, Florence, Italy, 19-22 September. SPE-134330-MS. https://doi.org/10.2118/134330-MS.

Vincent, M. C. 2011. Optimizing Transverse Fractures in Liquid Rich Formations. Presented at the SPE Annual Technical Conference and Exhibition, Denver,

Colorado, 30 October-2 November. SPE-146376-MS. https://doi.org/10.2118/146376-MS.

Wen, Q., Zhang, S., Wang, L. et al. 2007. The effect of proppant embedment upon the long-term conductivity of fractures. *Journal of Petroleum Science and Engineering* **55** (3–4): 221-227. http://dx.doi.org/10.1016/j.petrol.2006.08.010.

Weaver, J. D., Nguyen, P. D., Parker, M. A. et al. 2005. Sustaining Fracture Conductivity. Presented at the SPE European Formation Damage Conference, Sheveningen, The Netherlands, 25-27 May. SPE-94666-MS. https://doi.org/10.2118/94666-MS.

Weaver, J. D., Van Batenburg, D. W., and Nguyen, P. D. 2006. Sustaining Conductivity. Presented at the SPE International Symposium and Exhibition on Formation Damage Control, Lafayette, Louisiana, 15-17 February. SPE-98236-MS. https://doi.org/10.2118/98236-MS.

Weaver, J. D., Parker, M., Van Batenburg, D. W. et al. 2007. Fracture-Related Diagenesis May Impact Conductivity. *SPE Journal* **12** (03): 272-281. SPE-98236-PA. https://doi.org/10.2118/98236-PA.

Weaver, J. D., Rickman, R. D, and Luo, H. 2008. Fracture Conductivity Loss Due to Geochemical Interactions Between Man-Made Proppants and Formations. Presented at the SPE Eastern Regional/ AAPG Eastern Section Joint Meeting, Pittsburgh, Pennsylvania, 11-15 October. SPE-118174-MS. https://doi.org/10.2118/118174-MS.

Weaver, J. D., Rickman, R. D, Luo, H. et al. 2009. A Study of Proppant Formation Reactions. Presented at the SPE International Symposium on Oilfield Chemistry, The Woodlands, Texas, 20-22 April. SPE-121465-MS. https://doi.org/10.2118/121465-MS.

Weaver, J. D. and Rickman, R. D. 2010. Productivity Impact from Geochemical Degradation of Hydraulic Fractures. Presented at the SPE Deep Gas Conference and Exhibition, Manama, Bahrain, 24-26 January. SPE-130641-MS. https://doi.org/10.2118/130641-MS.

World Oil Data. 2015. Proppant Tables. *Gulf Publishing Company*, Houston, Texas. http://www.worldoil.com/media/3025/proppant-tables-2015.pdf

Yasuhara, H., Elsworth, D., and Polak, A. 2003. A Mechanistic Model for Compaction of Granular Aggregates Moderated by Pressure Solution. *Journal of Geophysical Research* **108** (B11): 2530.

Zhang, Y., Marongiu-Porcu, M., Ehlig-Economides, C. A. et al. 2010. Comprehensive Model for Flow Behavior of High-Performance-Fracture Completions. *SPE Prod & Oper* **25** (04): 484-497. SPE-124431-PA. https://doi.org/10.2118/124431-PA.